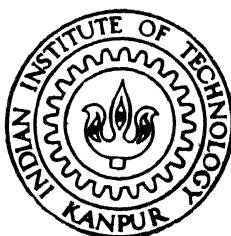


# THEORETICAL STUDIES ON POROUS SILICON

by  
GEORGE C. JOHN



DEPARTMENT OF PHYSICS

INDIAN INSTITUTE OF TECHNOLOGY KANPUR

DECEMBER, 1996

PHY  
1996  
D  
JOH.  
THE  
TH  
PHY/1996/D  
J613

# **Theoretical Studies on Porous Silicon**

*A Thesis Submitted  
in Partial Fulfillment of the Requirements  
for the Degree of  
Doctor of Philosophy*

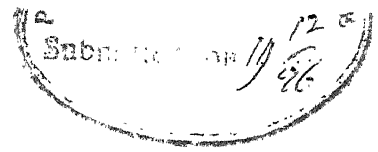
*by*  
**George C. John**

*to the*  
**Department of Physics  
Indian Institute of Technology, Kanpur**  
*December, 1996.*

-5 AUG 1997  
CENTRAL LIBRARY  
I. I. T., KANPUR

---

Vol. A 123640



## CERTIFICATE

It is certified that the work contained in the thesis entitled **Theoretical Studies on Porous Silicon** by **George C. John**, has been carried out under my supervision and that this work has not been submitted elsewhere for a degree.

*Vijay Singh*  
Dr. Vijay A. Singh  
Professor,  
Department of Physics,  
Indian Institute of Technology, Kanpur.

December, 1996



# Synopsis

Porous silicon was accidentally discovered in 1956 during the anodic etching of crystalline silicon in aqueous HF solution. It is a brittle, spongy material consisting of an intricate network of nanometer-size pores and silicon crystallites. The formation of a variety of pore morphologies in preference to uniform etching of silicon has evoked a great deal of interest in the scientific community. In 1990, high porosity (60-80%) samples of porous silicon were fabricated, which exhibited a surprisingly strong red luminescence on illumination with light of wavelength  $\lambda = 514.5nm$  [1]. Ever since this discovery, porous silicon has been the focus of attention of several workers in the field of semiconductor physics [2,3].

Crystalline silicon is an indirect gap material with a band gap of 1.1 eV, and consequently, the momentum conservation rule inhibits radiative transitions between the conduction band minimum and the valence band maximum. In porous silicon, the observed photoluminescence is in the range 1.3 - 2.2 eV, and has an external absolute quantum efficiency of 1-10%. This unexpected behavior has been explained in terms of the quantum confinement model [1] which posits an enhanced energy gap because of the increased kinetic energy due to carrier confinement in nanometer sized crystallites. However, this simple explanation is hard put to explain several vagaries observed in the photoluminescence behavior. **Chapter 1** constitutes a brief introduction to the porous silicon problem, where we review the porous silicon formation process and major theories proposed to explain the photoluminescence behavior.

Porous silicon formed under different anodization conditions exhibits a variety of rich and complex structures similar to those observed in diverse growth phenomena such as electrochemical deposition, viscous fingering and bacterial colony formation.

The presence of such varied behavior has led to the view that some interesting physical processes must be at work, besides the electrochemistry of silicon dissolution.

**Chapter 2** describes a drift diffusion model [4] which is successful in generating the various morphological classes reported in experimental growth literature. These are (i) fractal dendritic growth as seen in diffusion limited aggregation (DLA), (ii) homogeneous dense branching morphologies with a stable circular growth front. (iii) stringy morphologies, and (iv) inhomogeneous dendritic morphologies. We propose that the four classes result from the competition

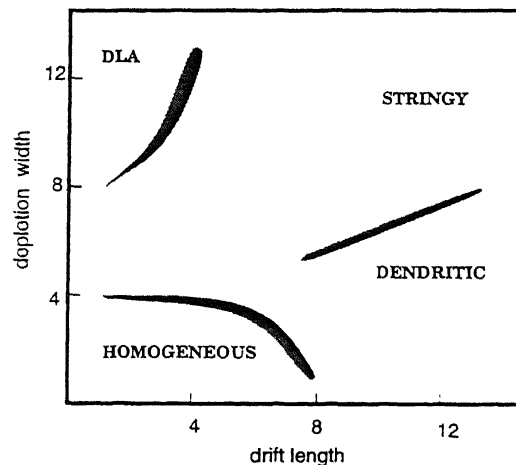


Fig.1: Phase diagram of various morphologies obtained by tuning two parameters (i) depletion width (ii) drift length (in lattice units)

between two antithetical scales - a diffusion length which tends to keep particles away from the growing cluster, and a drift length which drives particles towards surface inhomogeneities. A phase diagram depicting the transitions between morphological classes with varying scales is shown in Fig. 1.

In **Chapter 3** we extend the drift diffusion scheme to silicon anodization in HF, by means of a diffusion induced nucleation model [5]. A competition between the semiconductor depletion layer and electric field enhancement due to surface irregularities induce random removal of silicon atoms (i.e., an inverse nucleation process). This scheme successfully reproduces experimentally observed phenomena such as (i) high porosity structures similar to samples exhibiting visible photoluminescence, (ii) a constant rate of growth, (iii) the dependence of the rate of growth on the anodization potential, and (iv) electropolishing of silicon in the high potential limit. Further, the effect of quantum confinement on porosity can also be demonstrated within this model.

The photoluminescence (PL) spectrum of porous silicon is asymmetric on the energy scale, with a large full width at half maximum (FWHM) of  $\sim 300$  meV. **Chapter 4** presents a model for the spectral line shape [6]. Porous silicon is considered to be a collection of disordered silicon crystallites having a Gaussian distribution of sizes in the range 2 - 4 nm. Based on effective mass theory,

analytical expressions for the photoluminescence spectrum of such a distribution is obtained. This can explain both the asymmetry in the PL spectrum and the large FWHM (see Fig. 2). Based on the peak position of the calculated spectrum the exciton binding energy of the electron hole pair is estimated. This is found to be in better agreement with our understanding than those estimated by earlier electronic structure calculations. The low energy tail shown by some photoluminescence spectra is also explained using the Lifshitz argument.

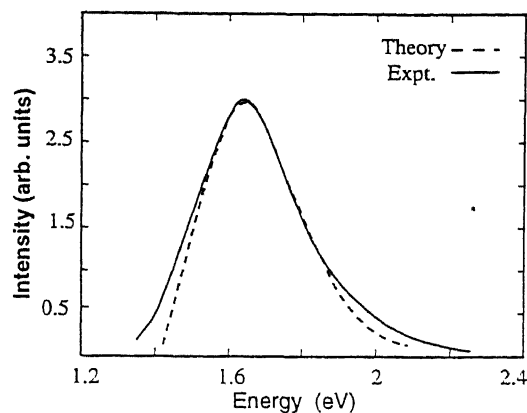


Fig.2. The porous silicon photoluminescence spectrum. The solid line is an experimental spectrum. The broken line represents a theoretical fit based on Ref. 6

The simple quantum confinement model was hard put to explain several experimental observations related to the temperature and pressure dependence of luminescence from porous silicon such as:

1. The PL intensity shows a maximum with temperature, the peak being in the range 50K - 150K
2. The luminescence decay time falls by an order of magnitude or more as the temperature is increased from  $\sim 10$ K to room temperature.
3. The PL intensity falls steeply with pressure.
4. The luminescence decay time decreases systematically with emission energy in the range 1.4 - 2.5 eV
5. The PL peak position exhibits an anomalous behavior (both blue and red shifts) with temperature.
6. The PL peak position exhibits an initial blue shift and a subsequent red shift with pressure, when the pressure transmitting medium is alcohol.

**Chapter 5** describes a unified model to explain all the above observations within an entirely analytical framework [7]. Based on conductivity studies, we propose that carrier hopping in silicon nanocrystallites follows a Berthelot type temperature

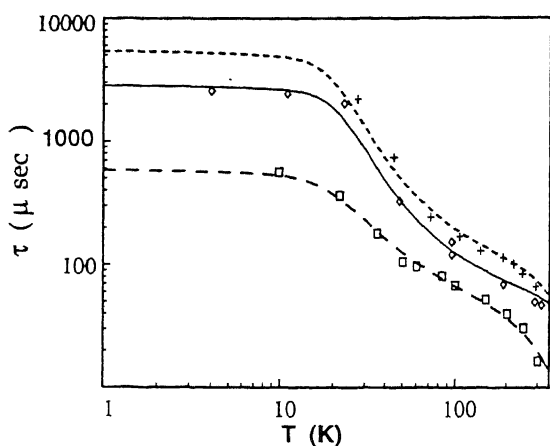


Fig.3. The temperature dependence of the luminescence decay time in porous silicon. The model of Ref.7 yields excellent fits to the data reported by different groups.

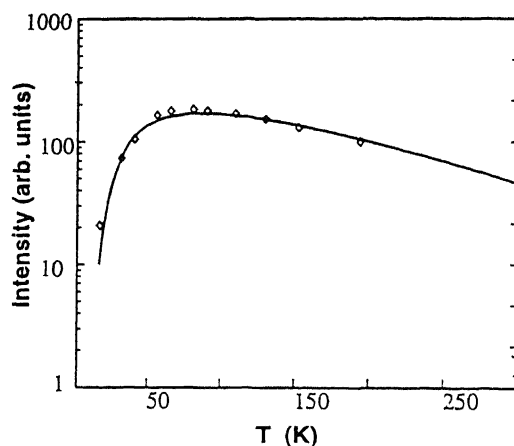


Fig.4. The temperature dependence of intensity in porous silicon luminescence. The solid line is a theoretical fit based on Ref. 7 to the data reported in Ref. 3.

dependence, i.e. it increases exponentially with temperature. The competition between the carrier hopping and an Arrhenius type radiative recombination is shown to explain the temperature and pressure dependence of the luminescence lifetime and intensity (see Figs. 3 and 4). We then extend this model within the quantum confinement scheme and successfully explain the luminescence lifetime dependence on emission energy and the observed temperature and pressure dependencies of the PL peak position.

Porous silicon has a large surface area. Several workers have contended that the luminescence originates from the molecular complexes found on the porous silicon surface [2]. Alternately, the disordered surface may give rise to several trap states which can play an intermediate role in the photoluminescence process. In this context, it is necessary to characterize the porous silicon surface. A common tool used for this purpose is infrared vibrational spectroscopy. The vibrational modes of the Si-H bond are known to be correlated to the electronegativity of the surrounding environment. We define a renormalized electronegativity based entirely on theoretical atomic scales. This new scale is successfully correlated to the vibrational frequencies of a given Si-H or Si-Cl bond in a particular environment [8]. This model is outlined in **Chapter 6** and used to systematize the assignment of vibrational frequencies observed in porous silicon.

In conclusion, we have presented a unified model to explain the vast body of experimental data in porous silicon. A simulation model for the formation of diverse

pore morphologies in porous silicon has also been developed. We show that the luminescence properties are modified by the disordered nature of the system as well as carrier hopping on or between crystallites. The optical characteristics are thus seen to correlate with the mesoscopic nature of porous silicon. **Chapter 7** presents a brief discussion of our results and suggests guidelines for future work.

## References

1. L.T.Canham, Appl. Phys. Lett. **57**, 1046 (1990).
2. G. C. John and V. A. Singh, Phys. Reports **263**, 93 (1995).
3. Y.Kanemitsu, Phys. Reports **263**, 1 (1995).
4. G. C. John and V. A. Singh, Phys. Rev. E **53**, 3920 (1996).
5. G.C.John and V.A.Singh, Phys. Rev. B **52**, 11125 (1995).
6. G. C. John and V. A. Singh, Phys. Rev. B **50**, 5329 (1994).
7. G. C. John and V. A. Singh, Phys. Rev. B **54**, 4416 (1996).
8. H.C.Verma, G. C. John, and V. A. Singh, Phys. Rev. B **53**, 9831 (1996).

*To my wife,  
who bore the brunt  
of this thesis.*

## Acknowledgments

The Ph.D. program in contemporary university education is the closest approximation we have to the ancient Indian *Gurukulam* tradition. In this spirit, what I have to acknowledge my *Guru* - Prof. Vijay Singh - for, at the end of these three and a half eventful years, go much beyond this thesis. What I have learned from him is not merely physics, but a whole new way of thinking, and his immense tolerance to mistakes, as I kept making a whole lot of them. Let me thank Dr.Singh in the knowledge that working with him has made me a better human being.

I must thank Dr.Sonali Banerjee for motivating work on porous silicon. This developing field which proved to be of a highly interdisciplinary nature enabled me to get acquainted with the philosophy of science, inclusive of its prejudices. Invaluable support was also provided at home by Drs. Sandeep Agarwal, S.Kumar, Y.N.Mohapatra, S.C.Agarwal and R.Prasad. I also wish to acknowledge the help and co-operation extended to me by Dr.B.M.Arora and Dr.K.L.Narasimhan during my brief, but extremely fruitful stay at the Tata Institute of Fundamental Research, Bombay.

I would like to thank Alok, Anirudh and Gaurav for help with the manuscript.

Now, it is the turn to acknowledge my friends without whom life at IIT Kanpur would not have been so meaningful. Apu and Sajith were constant companions who provided color and flavor to an otherwise dreary existence. I must thank Dr.Singh's family for their friendship, and David, Joseph, Sundar and their families for invaluable moral and spiritual support.

My family has played a key role in my career so far. I must thank my late father for having taught me to think critically about physical phenomena, my mother for being a pillar of support and encouragement, and my little sister for her confidence in me. My wife, Hazel, was always "by my side" despite being miles away, and without her, this thesis would not have been possible.

Lastly, let me express the joy and gratitude in my heart for a promise well kept - "*In all your ways acknowledge Him, and He shall direct your paths.*" (Proverbs 3:6).

George C. John

# Contents

<b>1</b>	<b>Introduction</b>	<b>1</b>
1.1	Porous Silicon . . . . .	2
1.2	Formation of Porous Silicon . . . . .	3
1.3	Luminescence from Silicon . . . . .	6
1.3.1	The Quantum Confinement Model . . . . .	7
1.3.2	Chemical Luminescence Models . . . . .	9
1.3.3	Recombination via Intermediate States - The Hybrid Model . . . . .	10
1.4	Microscopic theories . . . . .	11
1.5	More on Luminescence from Silicon - Some Surprises. . . . .	18
<b>2</b>	<b>Porous Silicon Formation: A Generalized Model for Aggregation and Etching</b>	<b>22</b>
2.1	Introduction . . . . .	22
2.2	Existing Models of Aggregation and Etching . . . . .	23
2.3	The Drift-Diffusion Model . . . . .	26
2.4	Results . . . . .	28
2.5	Discussion . . . . .	31
<b>3</b>	<b>Porous Silicon Formation: The Diffusion Induced Nucleation Model</b>	<b>34</b>
3.1	Introduction . . . . .	34
3.2	Phenomenological Theories . . . . .	36
3.3	Computer Simulations of Porous Silicon Formation . . . . .	42
3.4	The Diffusion Induced Nucleation Model . . . . .	47
3.5	Morphologies in Diffusion Induced Nucleation . . . . .	49
3.6	Discussion . . . . .	52



<b>4</b>	<b>Shape of the Luminescence Spectrum in Porous Silicon</b>	<b>59</b>
4.1	Introduction . . . . .	59
4.2	Theoretical Framework . . . . .	61
4.2.1	The Low Energy Tail in PL . . . . .	65
4.3	Results . . . . .	66
4.4	Discussion . . . . .	69
<b>5</b>	<b>Model for the Photoluminescence Behavior of Porous Silicon</b>	<b>75</b>
5.1	Introduction . . . . .	75
5.2	The Model . . . . .	78
5.2.1	The Photoluminescence Intensity . . . . .	78
5.2.2	Dynamics of Carrier Hopping . . . . .	80
5.3	Photoluminescence Intensity . . . . .	82
5.3.1	Temperature Dependence . . . . .	82
5.3.2	The Luminescence Decay Time . . . . .	84
5.3.3	Pressure Dependence . . . . .	87
5.4	Model Dependent Results . . . . .	89
5.4.1	Dependence of the Lifetime on Luminescence Energy . . . . .	90
5.4.2	Temperature Dependence of the PL Peak . . . . .	92
5.4.3	Pressure Dependence of the PL Peak . . . . .	94
5.5	Discussion . . . . .	96
<b>6</b>	<b>Vibrational Spectra of Defects in Porous Silicon: An Orbital Radii Based Approach</b>	<b>100</b>
6.1	Introduction . . . . .	100
6.2	The Renormalized Electronegativity (REEL) Model . . . . .	103
6.2.1	Electronegativity and Orbital Radius . . . . .	103
6.2.2	Vibrational Spectra . . . . .	106
6.3	Discussion . . . . .	108
6.4	Conclusion . . . . .	114
<b>7</b>	<b>Conclusion</b>	<b>117</b>

# List of Figures

1.1	Trench formation during silicon anodization in $\text{HF}$ acid. . . . .	2
1.2	A typical photoluminescence spectrum. . . . .	6
1.3	The effect of confinement on the band structure of silicon. . . . .	8
1.4	The levels of disorder in porous silicon . . . . .	12
2.1	The drift-diffusion model . . . . .	27
2.2	Morphologies in the drift-diffusion model . . . . .	29
2.3	Transition from dense branching to stringy morphologies . . . . .	30
2.4	Transition from DBM to DLA in the drift-diffusion model . . . . .	31
2.5	Phase plot of patterns obtained using the drift-diffusion model . . . . .	32
3.1	Typical I-V characteristic (schematic) for anodization of p-type silicon in $\text{HF}$ . . . . .	37
3.2	Schematic representation of the semiconductor - electrolyte system according to the Beale model . . . . .	38
3.3	The "pinch off" effect due to the overlap of depletion layers. . . . .	39
3.4	Drift-diffusion growth on a linear substrate . . . . .	46
3.5	The diffusion induced nucleation model . . . . .	47
3.6	Typical morphologies obtained in the diffusion induced nucleation simulations . . . . .	50
3.7	Growth rate of porous silicon . . . . .	53
3.8	Variation of the porous silicon growth rate with the depletion layer width . . . . .	54
3.9	Porosity vs. depth plot for a typical simulation . . . . .	55
4.1	Salient Features of the PL spectra . . . . .	60
4.2	Theoretical PL spectra . . . . .	63

4.3	Comparison of theoretical and experimental PL spectra (from Cullis and Canham, 1991) . . . . .	67
4.4	Comparison of theoretical and experimental PL spectra (from Vial <i>et al.</i> , 1992) . . . . .	69
4.5	Comparison of theoretical and experimental PL spectra (from Zhang <i>et al.</i> , 1993) . . . . .	70
5.1	Possible model of tunneling through a vibrating barrier of width $S$ and height $V_0$ . . . . .	80
5.2	The variation of the luminescence intensity with temperature . . . . .	83
5.3	The temperature dependence of the luminescence decay time . . . . .	85
5.4	The variation of luminescence intensity with pressure . . . . .	88
5.5	The variation of the luminescence decay time with confinement energy . . . . .	91
6.1	Sanderson electronegativity vs. the Zunger radius . . . . .	104
6.2	Linear relationship between the Sanderson electronegativity and the REEL quantum scale. . . . .	105
6.3	Linear relationship between the Si-H band stretching frequency and the REEL quantum scale . . . . .	107
6.4	The vibrational spectra of Si-H and Si-O bonds in porous silicon reported by various groups . . . . .	109
6.5	Linear relationship between the Si-Cl bond stretching frequency and the REEL quantum scale . . . . .	115
7.1	Transition from the molecular regime to the bulk solid . . . . .	118
7.2	Role of surface states in luminescence. . . . .	121

# Chapter 1

## Introduction

Silicon is - arguably - the most widely studied element in history. The technological applications of this material have revolutionized modern civilization and it has emerged as the workhorse of the semiconductor industry. The latter half of this century may rightly be termed the “silicon age” - so ubiquitous is the influence of this element in our day-to-day existence. On the other hand, silicon has also helped in furthering our understanding of traditional solid state physics. It has been intensely studied by the band structure theorists, being used as a test case for every new scheme, and any variation in methodology whether major or minor.

Nearly fifty years into silicon research, this thesis which purports to carry out further theoretical studies on silicon has been motivated by the possibility of extending the dominance of this material to an arena hitherto dominated by III-V semiconductors - namely, optoelectronics. Crystalline silicon has an indirect band gap of 1.17 eV, and the momentum conservation rule inhibits radiative transitions between the valence band maximum and the conduction band minimum. In 1990, photoluminescence in the range 1.3 – 2.2 eV with an external absolute quantum efficiency of 1 – 10% was observed from a novel material called Porous Silicon [1]. Since then, several review articles [2–5], conferences [6–9], and well over a thousand publications have been devoted to this interesting optical behavior. Theoretical studies of the formation of porous silicon and its surprising optical behavior constitute the subject matter of this thesis.

## 1.1 Porous Silicon

Porous silicon (PS), as the name suggests, consists of a brittle silicon skeleton permeated by an intricately woven network of nanometer sized pores. During anodization of silicon in hydrofluoric acid (HF), material removal does not always occur in the form of a uniform etch, but through the formation of microscopic trenches on the surface (see Fig. 1.1). Eventually these trenches develop branches and get interconnected, leading to the formation of a pore network. The resultant silicon structure is seen to consist of irregular columns and spheres with diameters in the range 1-10 nm.

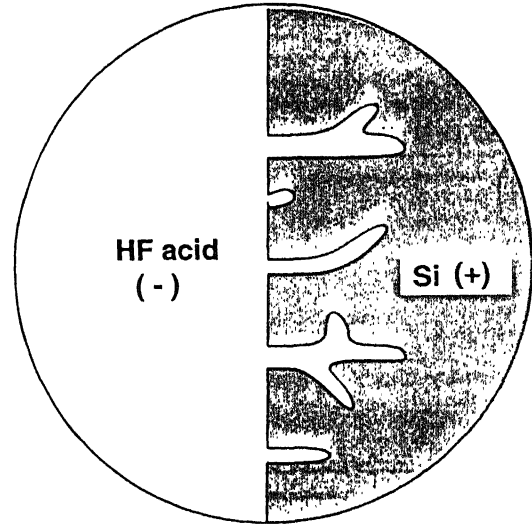


Figure 1.1: Trench formation during silicon anodization in HF acid.

The central problem in porous silicon research today is discovering the origin of light emission from silicon. In order to maximize the luminescence yield and tune the emission parameters such as frequency and decay time, a better understanding of the carrier dynamics associated with the light emission process is needed. The diverse pore morphologies found in PS have puzzled the semiconductor community for the last four decades, and continue to elude a concrete theory. The eventual goal of all research is to fabricate PS under controlled conditions leading to desired characteristics needed to make an optoelectronic device, which could ultimately be integrated into a “chip.” Hence, this novel material opens up a new vista of truly interdisciplinary research involving semiconductor physics, non-equilibrium growth processes, electrochemistry etc.

The present thesis aims to explore - at a theoretical level - the formation mechanism as well as the photoluminescence behavior of porous silicon. The remaining sections of this chapter present a brief overview of existing theoretical models of PS photoluminescence. Microscopic attempts to validate these models are reviewed in

Sec. 1.4. The issues that can be resolved within these models are spelt out, and the problems that remain unresolved are discussed.

Chapters 2 and 3 provide a short review of the formation problem, and develop a computational model that successfully simulates several characteristics of the porous silicon formation process. Chapters 4 and 5 study the optical properties of PS, and present models for the PL line shape, intensity and decay dynamics. Chapter 6 proposes a phenomenological scheme for the assignment of vibrational modes observed in PS using infrared spectroscopy, which has gained ground as a powerful tool for the characterization of the PS surface. Chapter 7 summarizes our results and provides guidelines for future research.

## 1.2 Formation of Porous Silicon

Ever since the discovery of porous silicon in 1956 at the Bell laboratories by Uhler [10], the causative mechanism associated with its formation process has been of some interest to the researchers. Unlike theories of electronic structure and photoluminescence, theoretical studies on porous silicon formation span nearly four decades. In spite of this, formation is perhaps the least understood of the several enigmas posed by this material. Various models have been proposed to explain the formation of the observed pore patterns. These range from purely electrochemical theories to stochastic simulations representative of physical phenomena. The discovery of visible photoluminescence in 1990 has also served to enhance the interest in PS formation studies, as the synthesis of PS under controlled conditions is an essential pre-requisite for a better control over its optical properties.

Porous silicon is normally synthesized in an electrolytic reaction where the silicon substrate constitutes the anode and an acid resistant metal such as platinum is used as the cathode. The electrolyte consists of  $\simeq 49\%$  HF, diluted in de-ionized water or ethanol at ratios ranging from 1:1 to 1:5. Currents in the range  $10 - 30 \text{ mA/cm}^2$  are passed through the electrolyte over a period of 5 - 60 minutes. A porous layer is formed on the surface of the silicon substrate, its thickness increasing uniformly with time. PS layers of thickness upto  $500 \mu\text{m}$  have been fabricated by this method. Note that in the absence of any current, the acid would have eaten away the silicon uniformly at a rate of a few nm/hr. This process, distinct from the anodization

procedure, is termed "passive etching."

Transmission electron microscopy (TEM) studies of porous silicon have been reported by several workers [11,12]. They reveal that porous silicon consists of isolated crystallites and/or chains of crystallites linked by narrow silicon walls. The crystallites are found to be in the size range 1-10 nm. This implies clusters of about  $10^2 - 10^4$  atoms which retain the diamond like lattice structure of bulk silicon. The pore structure exhibits a variety of morphologies depending on the experimental conditions governing the anodization process, namely,

- doping type
- doping level
- anodization current
- electrolyte concentration

A p-type silicon substrate forms a uniform and highly interconnected network of random pores, resulting in a spongy structure. In n-type, the pores are formed only under illumination and are relatively linear. For degenerately doped cases (both  $p^+$  and  $n^+$ ), the geometries are similar to the interconnected p-type structure, but with shorter and wider pores. At higher current densities, the pores widen further. In n-type, the linear pores tend to become pipe like in this case. At very high currents, silicon is uniformly etched away, leading to electropolishing. This can also occur at very low HF concentration.

Besides the electrochemical etching of crystalline silicon, several other techniques have been employed to fabricate Si nanocrystallite layers. Microwave plasma decomposition of Si-H<sub>4</sub> silane gas onto a quartz substrate gives rise to spherical nanocrystallites in the size range 2-7 nm. [13]. Laser breakdown of silane also results in silicon nanocrystallites with an oxide coating of  $\sim 1.6$  nm. thickness [14]. From SiO<sub>2</sub>, Si nanoparticles have been obtained by rf-magnetron co-sputtering techniques [4]. This method has also been employed to obtain Ge nanocrystallites. Another successful approach to fabricate porous silicon like layers is the high frequency spark erosion [15] of a silicon substrate using a tungsten anode. All these methods result in silicon nanocrystallites capable of luminescing in the visible range. Recently, light emitting

Si-SiO<sub>2</sub> superlattices have been grown by molecular beam epitaxy [16,17]. However, in this thesis, we will focus our attention on the anodization of silicon in HF.

The most common characterization parameter employed to describe porous silicon morphology is the sample porosity. Assuming a silicon wafer is completely converted to porous silicon, the porosity  $p$  is calculated as

$$p = \frac{\text{mass of Si wafer} - \text{mass of porous film}}{\text{mass of Si wafer}} \times 100$$

The preferential pore formation during anodization in comparison to a uniform etch raises the following questions, “Is it a chemistry related phenomena caused by competing reaction mechanisms, or is there more physics to it? Do the semiconducting properties of the system play any role in the process?” The earlier phenomenological models have focused on the chemistry of dissolution as the determining factor for pore formation. Then the attention shifted to possible surface effects on the electric field distribution in the Si substrate. The role of the semiconducting properties of the system in effecting an electric field redistribution assumed importance as a major factor. With the better understanding of non-equilibrium growth phenomena which has been achieved in the recent past, several statistical models based on computer simulations have also been formulated to explain porous silicon formation.

A satisfactory theory of PS formation must be able to (i) understand the formation of pores in preference to a uniform etch, (ii) explain the observed transition between pore morphologies obtained under various experimental conditions, and (iii) predict features such as the rate of growth of the film and the influence of initial conditions, say, the substrate roughness, on the porous layer. The eventual aim, as mentioned earlier, is the fabrication of a PS device under controlled conditions. Hence, models which can computationally simulate experimental configurations and predict the resultant device geometry and structure will be desirable. In chapters 2 and 3 we evolve a generalized computational model, premised on a possible underlying semiconductor phenomenology. This model successfully simulates the diverse morphological patterns described earlier and is successful in making experimentally verifiable predictions such as the rate of growth of the porous film and its dependence on the anodization potential.



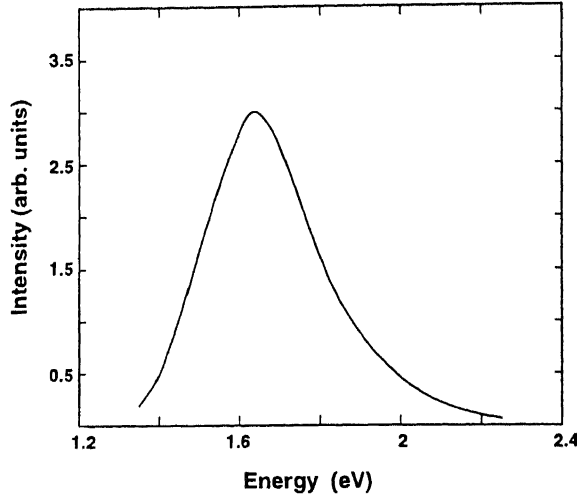


Figure 1.2: A typical photoluminescence spectrum.

### 1.3 Luminescence from Silicon

It is the visible photoluminescence (PL) of silicon and related optical properties that have invited maximum scientific attention. Porous silicon starts luminescing at a threshold porosity of around 45%, with the emission being in the range 1.2 - 2.8 eV, depending on the sample porosity. High porosity ( $> 60\%$ ) samples have an external absolute quantum efficiency [18] of 1 – 10%. A typical PL spectrum is depicted in figure 1.2. The spectrum is asymmetric about the peak, with a shoulder on the high energy side. The full width at half maximum (FWHM) is about 300 - 400 meV. Three bands have been identified in the emission spectrum of porous silicon. They are:

- The dominant red band with energies in the range 1.2 - 2.3 eV. This accounts for roughly 97% of the emission and has a slow luminescence decay with lifetimes from  $10^{-5}$  to  $10^{-3}$  s.
- The weak blue band with energies in the range 2.5 - 2.8 eV. This constitutes roughly 3% of the emission intensity and has a decay time in the nanosecond range.
- The infrared band with energies ranging from 0.8 to 1.3 eV.

Though the photoluminescence from porous silicon presents an interesting puzzle to the scientific community, the technological importance of this material is based on

its electroluminescence behavior - i.e., the emission of light when a current is passed through it. Porous silicon can electroluminesce both in aqueous electrolytes (wet electroluminescence) and solid state structures such as Au/PS/Si layers (dry electroluminescence). The luminescence efficiency for wet electroluminescence ( $\sim 10^{-3}\%$ ) is substantially higher compared to dry electroluminescence ( $\sim 10^{-5}\%$ ). However, for practical device fabrication, liquid-solid junctions are of little use. Further, wet electroluminescence is also affected by chemical reactions taking place on the porous silicon surface. In any case, the efficiency of electroluminescence is at best a thousand times less than that of PL. The spectra observed in photoluminescence and electroluminescence are remarkably similar. This suggests that the radiative mechanisms in both processes are of similar origin.

A variety of hypotheses have been advanced to explain the observed optical behavior of PS. The major models, namely, (i) the Quantum Confinement model, (ii) the Chemical Luminescence model, and (iii) the Hybrid model invoking radiative recombination via intermediate states are briefly reviewed below:

### 1.3.1 The Quantum Confinement Model

The carriers in high porosity samples of porous silicon are confined in microcrystallites whose typical size  $d$  is in the range 1-5 nm. This can be modeled by a simple picture - the particle in a box. From the uncertainty principle  $d\Delta p \sim h$ , the energy of the carriers relative to the band edge is given by the relation

$$\frac{(\Delta p)^2}{2m} = \frac{h^2}{2md^2} \quad (1.1)$$

This applies to both holes and electrons and a larger energy gap is plausible on these grounds.

We can extend the particle in a box picture using the well known effective mass approximation. The upshift of the conduction band can then be expressed as

$$\Delta E_u = \left(1 + \frac{m_T}{m_L}\right) \frac{h^2}{8m_T d^2}$$

where  $m_T$  ( $m_L$ ) is the transverse (longitudinal) effective mass, and  $d$  the confining length. For a 3nm wire, the conduction band upshift is estimated to be 252 meV [19]. Here we have assumed bulk values for the transverse ( $0.19m_e$ ) and longitudinal

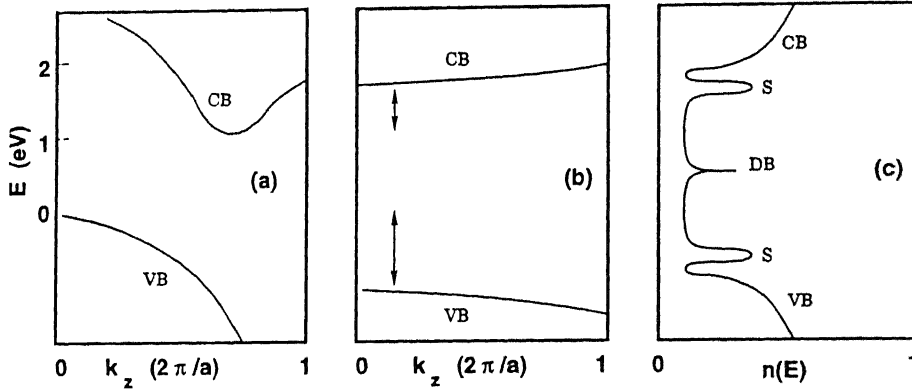


Figure 1.3: The effect of confinement on the band structure of silicon. (a) Crystalline silicon with an indirect gap of 1.17 eV (b) On confinement, the conduction band (CB) and valence band (VB) edges are pushed apart (see arrows) and become pseudo-direct (c) The density of states  $n(E)$  in a realistic nanocrystallite, with a U shaped distribution of surface states  $S$  near the band edges. The peak near the mid-gap region is due to dangling bonds (DB).

( $0.92m_e$ ) effective masses,  $m_e$  being the free electron mass. Because of the valence band degeneracy, the variation in the hole kinetic energy depends on the direction of the wire growth. Assuming growth in the (001) direction, the effective mass approximation yields the downshift of the valence band to be 371 meV [19] which is about one and a half times the conduction band upshift, the net enhancement in the gap being 0.6 eV. Thus energy gaps in the range 1.3 - 2.5 eV are possible. This can quantitatively account for the red luminescence.

Figure 1.3a depicts the bulk silicon band structure with a well defined indirect gap. The upshift due to confinement is depicted in Fig. 1.3b. A crystallite, however has discrete energy levels. The level spacing is ignored in the figure. Further, these calculations result in nearly flat bands at the valence band maximum and the conduction band minimum. This too can be understood on the basis of the uncertainty principle. We see that  $\Delta k \sim 1/d$  is large. The indirect gap is thus 'smeared' out and an almost direct gap may result. These arguments form the core of the basic quantum confinement model. Several microscopic electronic structure calculations have been carried out to verify this model. We shall discuss them in the next section (Sec. 1.4).

### 1.3.2 Chemical Luminescence Models

Visible luminescence from porous silicon has been found to be extremely sensitive to surface treatments. This has prompted some workers to contend that luminescence originates not from the silicon crystallites per se, but from chemical complexes found on the surface of porous silicon. Armed with an extensive knowledge of “ancient” literature, they came up with several molecules capable of luminescing in the observed spectral range. A particular favorite was ‘siloxene’- a complex of silicon, hydrogen and oxygen. This contention is supported by a comparison between the salient features of PL from both porous silicon and siloxene [20]. A review of the properties of siloxene is found in the article by Stutzmann and coworkers [21] who notes that

(i) annealed siloxene radiates in the same spectral range as porous silicon (600 - 800 nm) with long tails extending into the deep infrared.

(ii) The PL spectrum of annealed siloxene is broad, with a band width much larger than that of porous silicon. All the observed PL spectra fall within this range.

(iii) The temperature dependence of PL intensity for  $T > 100\text{K}$  in both materials is well described by the relation

$$\frac{I_0}{I(T)} = 1 + \exp\left(\frac{T}{T_0}\right)$$

with a characteristic temperature  $T_0$  between 50 K and 90 K.

(iv) The luminescence intensity is proportional to the excitation intensity over six orders of magnitude at both low and high temperatures for porous silicon and siloxene.

(v) The luminescence decays are non-exponential and become faster with increasing energy. Both nanosecond and microsecond to millisecond decays are observed in siloxene, as also with porous silicon.

(vi) Both materials exhibit similar photoluminescence excitation spectra.

The siloxene model has been disputed by some other workers [22] who report PL in freshly prepared porous silicon samples which exhibit infrared vibrational spectra lacking all oxygen related modes. Such a sample cannot have a very high intensity siloxene based luminescence. Besides this, the luminescence induced by soft x-rays in porous silicon (peak  $\sim 750\text{ nm}$ ) differs substantially from that produced in siloxene (peak  $\sim 520\text{ nm}$ ) [23].

Besides siloxene, some of the other molecules that have been hypothesized to be the luminescing agents in PS include polysilane chains [24,25] and non-bridging oxygen-hole complexes [26]. The polysilane hypothesis has also derived support from theoretical calculations carried out by various groups, which will be discussed in the next section (Sec. 1.4).

### 1.3.3 Recombination via Intermediate States - The Hybrid Model

The tug-of-war between the quantum confinement model and the chemical complexes model has led to a "hybrid model" where both the interior and the surface are involved in PL. Consider the case where an electron is radiatively excited into the conduction band in the interior of a crystallite. For a crystallite of size 3 nm, over 30% of the atoms will be on the surface, which can give rise to several surface states. Besides this, there could be dangling bond levels which fall in the mid-gap. The density of states in a nanocrystallite is represented in Fig. 1.3c. The surface states give rise to a U shaped distribution within the gap, and the dangling bond levels fall near the mid-gap region. The carrier has a high probability of reaching the surface and getting trapped there. It is then possible for surface related mechanisms to influence the radiative process.

Kanemitsu and coworkers [14] have proposed a simple phenomenological model based on their experimentally acquired data. The absorption edge for crystallites of sizes 9, 3.5 and 2 nm is observed at wavelengths 1200, 1000 and 850 nm respectively. The crystallite sizes were determined by TEM and analysis of the Raman spectra of the samples. The blue shift on size reduction may clearly be attributed to the quantum confinement effect. The PL peak energy is however invariant and located at 700-800 nm. They contend that the latter is thus an intrinsic effect common to all crystallites. The photogeneration of carriers is hypothesized to take place in the core of the crystallites and hence is size dependent. All crystallites have a large surface to volume ratio with a similar surface chemistry in terms of H and OH complexes. The recombination of carriers take place on the surface and hence PL is *size independent*. In another work [27] it is proposed that the red band PL has a slow decay and is from surface localized states while the blue PL band has

a fast decay and originates from the crystallite core. An implication of the model is that PL efficiency for smaller crystallites is enhanced since both the surface to volume ratio and the carrier transfer rate from the core to the surface increase with a decrease in the crystallite size. The PL intensity has a non-monotonic temperature dependence. At low temperatures, carrier diffusion to the surface is inhibited, hence PL intensity is low. At high temperatures, nonradiative recombination in the near surface regime increases and the PL intensity is lowered. Hence this model can also explain the peaking of PL intensity at around 100 K, which is an experimentally observed phenomena.

More detailed arguments for the surface states mechanism have been advanced by some workers [28,29] who also believe that radiative recombination occurs via the surface states on the silicon nanocrystallite. They propose that carrier recombination can occur in three ways (i) Carriers trapped in the bound states can recombine among themselves. These corresponds to the lower emission energies. (ii) Carriers from the band can recombine with carriers in the gap levels and (iii) there could be band to band recombination. They assign the infrared band to the capture of electrons by dangling bond states which fall in the mid-gap. The red band is mediated by the surface states in the gap which lie closer to the conduction band edge (see Fig. 1.3c). The fast blue emission is assigned to transitions from the conduction band to the valence band in the core of the crystallite. Thus the carriers can “choose” between several paths available for radiative recombination. Hence they term this the “smart quantum well” [30].

## 1.4 Microscopic theories

The enigma of porous silicon is its visible luminescence. One would like to understand the photoluminescence (PL), its excitation and decay characteristics. In the present section, we review attempts to explain PL based on explicit electronic structure calculations. These attempts must be distinguished from a host of phenomenological and qualitative theories which pervade the field, some of which were discussed in the previous section.

The calculation of the electronic properties of porous silicon is premised on an assumed geometrical structure and herein lies a major difficulty. Porous silicon is a

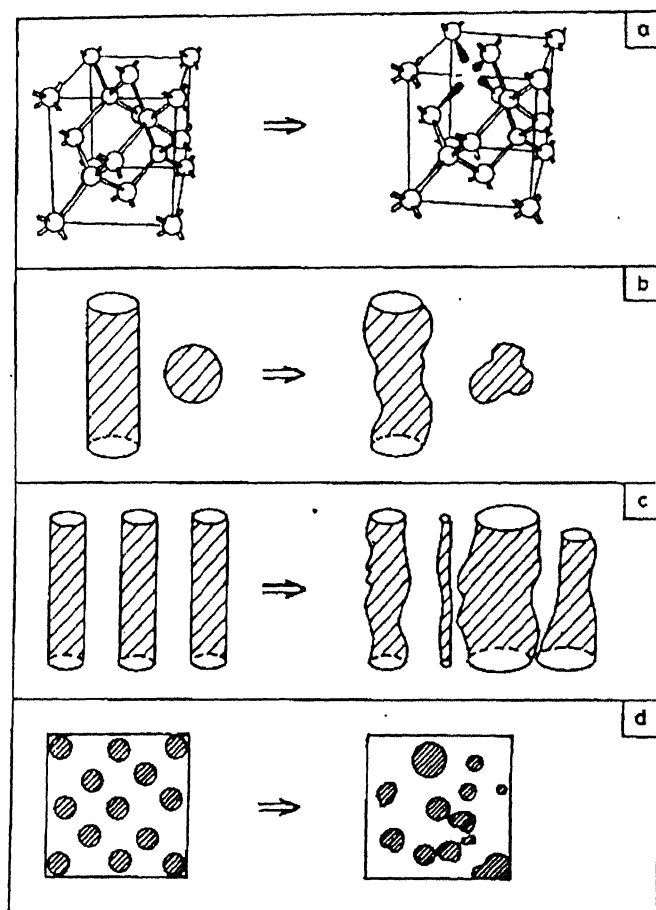


Figure 1.4: The levels of structural disorder in porous silicon may be staged thus. The left side represents the idealized structures normally used in electronic structure calculations. The right side is the more realistic view (a) Nanocrystallite at a microscopic level. The perfect crystal symmetry is disturbed by the presence of vacancies and multivacancies (not shown) accompanying dangling bonds. (b) The nanocrystallite is idealized in the form of a column (pillar) or dot (sphere). The surface of such a crystallite is highly irregular. The large surface area supports silicon hydride and oxide complexes and a large number of dangling bonds. (c) The columns or dots (not shown) are not of uniform diameter. They come in a distribution of sizes. (d) A cross sectional view of an idealized, regularly spaced and cylindrically or spherically shaped nanocrystallite. The more realistic view is one of irregularly shaped nanocrystallites forming a silicon skeleton against a backdrop of an intricate network of pores.

complex material which one would characterize by a hierarchy of disorders. Fig. 1.4 illustrates this complexity. The left side of Fig. 1.4 represents the idealized view adopted in most electronic structure calculations. The right side depicts the grim complex reality.

At the microscopic level one has nanocrystallites. The internal arrangement of silicon atoms is believed to be the same as the diamond like structure of crystalline silicon [31–33]. But one must accept a fair number of native defects: vacancies, divacancies, multivacancies and concomitant dangling bonds with bond rearrangements. The nanocrystallites occur in two forms: (i) columnar (also termed pillar or rod) or (ii) dots (spheres) or an admixture of both. However the surface is not all smooth. It is highly irregular and the surface area is large. The surface has dangling bonds and supports molecular complexes such as  $[\text{Si}_n\text{H}_m]$  polysilanes,  $\text{SiO}_2$  and siloxene derivatives. Further, the nanocrystallites may come in a variety of shapes and a range of sizes from 1–10 nm. Finally, these are not arranged in a regular fashion, but are randomly arranged with intervening spaces. One has a brittle, spongy silicon skeleton - hence the name porous silicon.

A calculation of the electronic properties which encompasses all levels of disorder is not feasible. The following points can be used to guide the calculations: (i) The local structure of the nanocrystallite is akin to crystalline silicon with lattice constant  $a_0 = 5.43\text{\AA}$ . (ii) The aspect ratio (height to radius) for the columnar structure is approximately 1000. (iii) The surface area of the nanocrystallite is large: 1–10  $\text{m}^2/\text{cm}^3$ . (iv) The porosity of the structure is high with  $p \approx 80\%$ .

The calculations assume an idealized structure such as the ones depicted on the left side of Fig. 1.4. Further, one may use periodic boundary conditions. In this case, Bloch's theorem holds and one can talk of the "band structure" of porous silicon. The other mode in which the calculation can be carried out is to use a cluster of  $N$  silicon atoms with  $N_b$  dangling bonds terminated by hydrogen. If one is using four atomic orbitals per silicon site, one obtains  $4N + N_b$  energy levels. The highest occupied (lowest unoccupied) energy level corresponds to the valence band maximum (conduction band minimum). The corresponding wave functions are termed HOMO (highest occupied molecular orbital) or LUMO (lowest unoccupied molecular orbital).

The methodology used can be classified as either semi-empirical or first principles based. Most of the semi empirical attempts are based on the tight binding scheme.



The advantages of this approach are: (i) it is easy to implement; (ii) large clusters of sizes comparable to the actual nanocrystallites can be studied (storage efficient); (iii) the algorithms run faster (time efficient). The disadvantage is the semi-empirical character itself, the reservation being that one can obtain a desired value by simply fine tuning parameters, or by adding a fresh one. The parameters of the Hamiltonian are determined with reference to some property or properties of the bulk host silicon. Thus optimized, the parameters are employed unchanged for porous silicon calculations.

The first principles methodology is based on the Kohn-Sham local density approximation (LDA) [34,35] using pseudopotentials. No adjustable parameters are employed in this scheme. LDA predictions for the ground state properties of silicon have been verified by a variety of works and further, heralded as a major triumph of band structure methodology [36–38]. The lattice constant  $a_0 = 5.43\text{\AA}$ , the bulk modulus ( $0.99 \times 10^{12}$  dynes/cm<sup>2</sup>), the total valence energy ( $-7.919$  Ry), the cohesive energy and the frozen ( $T \rightarrow 0$ ) phonon frequency are all reproduced to an accuracy of  $\approx 1\%$ . In spite of such an impressive list of achievements, there is a major problem with the LDA. The predicted band gap  $E_g$  of crystalline silicon is  $0.6$  eV, almost half of the observed value of  $1.14$  eV at  $T = 0$ . This corresponds to luminescence (if at all) in the far infra-red ( $\lambda = 2 \times 10^4\text{\AA}$ ). Given the fact that a primary aim of porous silicon electronic structure calculations is to explain the visible PL, the band gap underestimation by LDA is unfortunate. In LDA based investigations of porous silicon, the bulk  $E_g$  is engineered by upshifting the conduction band in various ways.

Read and coworkers have performed LDA based calculations on columnar wire geometries with a uniform rectangular cross section [39] as well as undulating columns which can be visualized as a periodic array of overlapping spheres [40]. The surface is passivated with H atoms. Periodic boundary conditions were employed so as to obtain a band structure. For a rectangular wire of diagonal thickness  $d = 2.3$  nm, a direct gap of  $0.78$  eV was obtained, which is larger than the reported LDA values of  $0.5 - 0.6$  eV [37]. The band upshift  $\Delta E_u$  could be expressed as

$$\Delta E_u = C/d^2$$

where  $C$  is a constant. Using this expression, they calculate the band gap for a  $3$  nm crystallite to be close to  $1.7$  eV, which is larger than the observed PL peak of  $\sim$

1.5 eV. Consequently, they have to invoke an unreasonably large excitonic binding energy of almost 200 meV. In chapter 4 we show that the inherent disorder in the PS system can lower the observed peak energy, and hence one need assume only physically reasonable exciton energies of about 60 meV.

In a similar first principles study employing square columns, Buda and coworkers [41] also obtain a direct gap  $E_g$  which is seen to vary with the crystallite size as

$$E_g = E_g(\infty) + \frac{c_1}{d} + \frac{c_2}{d^2}$$

where  $c_1, c_2$  are constants. This enhancement of the bandgap with decreasing  $d$  is also observed by Ohno and colleagues [42] in their LDA based calculations. They also find that the oscillator strength for transitions between the valence band maximum and the conduction band minimum is enhanced by 2 to 3 orders of magnitude as a result of confinement, though it is found to be a non-monotonic function of the size.

Semi-empirical calculations have also been carried out on free standing silicon wires [43] in the size range 7-27 Å. A complementary geometry of circular and square pores with interpore space occupied by Si has also been employed by some workers [44] (see Fig. 1.4d). All of them yield direct or nearly direct band gaps in the range 2.0 - 3.0 eV. The oscillator strength has also been found to increase with  $d$  [45], justifying light emission. Thus the quantum confinement model is theoretically validated for periodic arrays of Si crystallites.

Calculations have also been carried out for clusters of Si atoms passivated with H, within the LDA [46]. They report a decrease in the energy gap  $E_g$  with increasing cluster size  $d$ . Further, the oscillator strength is seen to exhibit a non-monotonic dependence on  $d$ , similar to the results of Ohno and coworkers [42] which were described earlier.

Some workers [47-49] employ a non-orthogonal tight binding framework to treat nearly spherical (closed shell) silicon clusters. They chart the gap dependence on size up to  $d = 4.3$  nm. (2058 silicon atoms). The attempted fit does not follow a  $1/d^2$  law, but

$$E_g(d) \sim 1/d^{7/5}$$

The calculated gap is compared with the experimental results on silicon nanocrystallites coated with hydrogen [50]. The PL emission energy is the difference of the

gap and the Coulomb energy ( $-3.752 e^2/\epsilon d$ ) as estimated by Kayanuma [51]. Further, they evaluate the radiative recombination lifetime  $\tau_r$ , and find it to be in the range  $10^{-4} - 10^{-6}$  sec. for  $E_g > 1.8$  eV and  $10^{-1} - 10^{-5}$  sec. for  $1.6 < E_g < 1.8$  eV. The dependence of  $\tau_r$  on the PL emission energy is found to compare favorably with experiment.

A noteworthy attempt to model the disorder in PS is due to Sawada, Hamada and Ookubo [52] who employ a semi-empirical tight binding methodology to study a two dimensional randomly porous cluster. The number of atoms in the cluster is around 450. A fraction (say, 100 atoms) are removed at random. The dangling bonds are terminated by hydrogen. The gap for a finite regular cluster of 350 atoms is 1.51 eV while that for 450 atoms is 1.39 eV. The difference of 0.12 eV can be ascribed to confinement effects. On the other hand, for the porous structure where 100 atoms are removed at random from the 450 atom cluster, the gap is 2.06 eV. The additional 0.55 eV enhancement is a *disorder* induced effect. Thus porous silicon has an enhanced gap due to both *confinement* and *disorder*.

Calculations have also been carried out in support of the chemical luminescence model. The electronic structure methods of quantum chemistry have been extensively employed for this purpose. Deak and coworkers [53] have considered siloxene structures which are planar  $[\text{Si}_2\text{H}(\text{OH})]_{3n}$ , linear  $[\text{Si}_2\text{H}_2\text{O}]_{3n}$ , and ring-like  $[\text{Si}_6\text{H}_6\text{O}_3]_n$  and substituted ring-like siloxenes  $[\text{Si}_6\text{H}_{6-x}(\text{OH})_x\text{O}_3]_n$ . It is found that the planar structure is metastable and will transform to a linear or ring like structure on heat treatment. Thus the surface of porous silicon is more likely to be covered by ring like siloxene and its other derivatives. The band is indirect and has a value 2.84 eV for the unsubstituted  $x = 0$  case and 1.82 eV for the fully substituted  $x = 6$  case. An analysis of the HOMO charge density reveals that it is high along the rings. The authors thus speak of a "chemical" quantum confinement in contrast to the "geometrical" quantum confinement.

In another quantum chemical study, Takeda and coworkers [54] consider a bridge model  $\text{Si}_{10}\text{-Cb}_{15}\text{-Si}_4\text{H}_8\text{-Si}_{10}\text{Cb}_{15}$ . Here  $\text{Si}_4\text{H}_8$  is the oligosilane bridge. Cb stands for a capped bond. The  $\text{Si}_{10}$  silicon cluster is terminated not by H, but the capped bond which is a  $1s$  orbital with electron affinity identical to Si. The gap 3.3 eV is *not* identified with PL emission, but with PL excitation. On excitation a fresh calculation employing configuration - interaction is carried out. The excited structure is once

again allowed to geometrically relax. The gap is now in the range 1.2 - 2.1 eV with the LUMO 50% *s*-like while the HOMO is 60% *p*-like. Given these symmetries, the optical transition matrix is non-negligible for the 1.2 - 2.1 eV de-excitation. This is identified with the PL emission. After de-excitation, it is found that the earlier structure is once again favored. The work thus attempts to explain why the PL excitation and emission energies generally differ by at least 0.5 eV.

Allan, Delerue and Lannoo [55,56] have calculated the electronic structure of linear  $\sigma$  bonded silicon atoms with H termination. They find that the radiative lifetime is independent of the size and falls in the nanosecond range. On the basis of the calculated energies and radiative lifetimes, they conclude that polysilanes may contribute to the blue band PL (1.8 - 2.8 eV) but certainly not to the dominant red band. From their earlier calculations [47,48] described on page 16, it is seen that the observed red band energies and decay times are compatible with the predicted emission from silicon clusters of size  $\sim 10^3$  atoms. It may then be possible to think of the red emission as originating from the core of the crystallite, whereas the blue band is due to the surface chemical complexes.

Though *almost* all calculations mentioned above yield a direct, enhanced band gap and a non-negligible oscillator strength between the valence band maximum and the conduction band minimum, certain worrisome points need to be mentioned. Firstly, the band gap underestimation by LDA makes any absolute comparisons with PL suspect. Within the first principle calculations themselves, there has been some disagreement on key issues such as geometry optimization. Buda and coworkers claim relaxation of atoms [41] on the crystallite surface, whereas some other workers [39] assume negligible relaxation. The effective masses calculated by two first principle approaches [40,42] show the same trend (i.e., they are larger than the bulk effective mass) but are significantly different. As far as the radiative lifetimes, and PL energies are concerned, one expects at best a semi-quantitative agreement. The presence of dangling bonds, excitonic binding and localization energies, non radiative relaxation and other radiative centers will defeat any attempt at absolute comparison. Finally, three elementary idealizations in most of the electronic structure calculations must be pointed out. The material considered is *not disordered, perfectly passivated and not porous*.

## 1.5 More on Luminescence from Silicon - Some Surprises.

The wealth of experimental results in this area is a challenge to the theorist, with many workers reporting conflicting observations. For instance, the work of Kane-mitsu, which reports a size independent PL emission [4], is at variance with the other experimental works in this field [17,57,58]. Some salient features of PL, about which a consensus seems to exist, have been described earlier in Sec. 1.3. The microscopic models of Sec. 1.4 have been able to explain - at least qualitatively - the observed emission energy range and the red and blue luminescence bands. However, several puzzles associated with the detailed nature of the light emitting process still remain. In this section, we list some such issues which need to be addressed within a common theoretical framework.

### The photoluminescence spectrum

The microscopic theoretical models have shown that the observed emission energies are justifiable within a quantum confinement scheme. The enhanced oscillator strength justifies the observed external quantum efficiency to some extent. However, the following points still need to be sorted out.

- The spectra have a large FWHM of 300 - 400 meV.
- The spectral line shape is asymmetric about the peak on the energy scale, with a shoulder on the high energy side.
- The energies computed for realistic crystallite sizes in electronic structure calculations are much larger than the observed PL peak energies [39]. To explain this, they need to invoke unphysically large values of the exciton binding energy.

It is evident that to explain the large linewidths, one needs to invoke a size distribution of crystallites. We find that such an assumption can also lead to the resolution of the other two problems listed here [59]. These calculations are discussed in chapter 4.

### Intensity and decay dynamics of PL

The intensity as well as the characteristic decay time of luminescence from porous silicon exhibit several features which cannot be accounted for within any one of the simple models outlined earlier in this chapter. Specifically,

- The PL intensity exhibits a non-monotonic variation with temperature, with a maximum in the range 50 - 150 K [4].
- The PL intensity drops exponentially with increasing pressure.
- The luminescence decay time falls by nearly two orders of magnitude as the temperature raised from 10 K to 300 K.
- The luminescence decay time is seen to decrease exponentially with increasing emission energy.
- The band gap of crystalline silicon is observed to red shift with increasing temperature. However, the observed temperature dependence of the PL peak is anomalous, with both blue and red shifts being reported by various groups [60,61].
- The crystalline silicon band gap redshifts with pressure. The PL peak of porous silicon may or may not show an initial blue shift depending on the pressure transmitting medium employed [62,63].

Several workers have attempted to model the luminescence decay dynamics by invoking a competition between the radiative and nonradiative process. We show that competing dynamics between an Arrhenius type ( $\propto \exp[-T_r/T]$ ) radiative recombination and a Berthelot type ( $\propto \exp[T/T_B]$ ) carrier hopping mechanism can successfully explain the diverse observations listed above.  $T_r$  and  $T_B$  represent characteristic temperatures associated with these processes. This “unified” model for the optical behavior of PS is discussed in chapter 5.

### Surface sensitivity of PL

The PL from porous silicon is seen to be highly sensitive to surface treatments. The spectral shape and intensity are seen to vary with aging and surface oxidation. The

PL is quenched on annealing, but a brief dip in HF can restore light emission. The PL characteristics can be affected by so much as a dip in boiling water. Given these vagaries in optical behavior, it becomes necessary to achieve a proper characterization of the sample surface.

The variation of PL with changing surface environments have also been substantiated by microscopic, theoretical calculations. In an LDA based approach to evaluate the energy levels of a planar polysilane, Van de Walle and Northrup [64] found the gap to be close to 2.75 eV and almost direct. When 50% of hydrogen was substituted with OH groups, the gap remained direct and was 1.7 eV. The lowered band gap in the OH substituted structure is attributed to the strong electronegativity of the O atom.

Infrared vibrational spectroscopy is a powerful tool to characterize the surface properties of porous silicon. The vibrational modes of the surface species can be related to the electronegativity of the surrounding environment. In chapter 6 we propose a phenomenological model which employs purely theoretical atomic scales to predict the stretching mode vibrational frequencies of hydrogen in silicon. This model is seen to provide a valuable tool for characterizing the PS surface.

## Absorption characteristics of PS

The excitation of light emission in PS also poses its share of problems. They are:

- The absorption edge in PS is at least 0.5 eV higher than the observed peak of emission.
- The PL spectral peak seems to blue shift linearly with increasing excitation intensity [65].
- The PL intensity initially increases linearly on increasing the excitation intensity, finally saturating to a constant value [66].

Besides these, there exists many other issues that stem from a lack of proper characterization of the material, leading to apparently contradictory observations. The dispute regarding the size dependence of the PL emission spectrum is a case in point. We also need to address the various unresolved questions regarding the formation process which were outlined in Sec. 1.2. In order to resolve these issues,

one may need to look well beyond the confines of traditional semiconductor theory. We now proceed to examine some of these problems in greater detail.

## **Key References**

The major references for the material contained in this chapter are listed below:

1. George C. John and Vijay A. Singh, Physics Reports **263**, 93-151 (1995).
2. Y.Kanemitsu, Physics Reports **263**, 1-91 (1995).



# Chapter 2

## Porous Silicon Formation: A Generalized Model for Aggregation and Etching

### 2.1 Introduction

The study of porous silicon formation spans four decades. Electrochemistry, semiconductor phenomenology, and more recently, computer simulations have been invoked to explain pore formation in silicon. The primary aim of porous silicon formation models is to explain, and reproduce, the diverse morphological patterns obtained under various experimental conditions, as described earlier in Sec. 1.2. We recall that a p-type silicon substrate gives rise to a uniform and highly interconnected network of random pores, resulting in a spongy structure. As the doping level is increased (i.e.,  $p^+$  substrate), the pores become shorter and wider. In n-type silicon, pores are formed only under illumination and are relatively linear compared to p-type silicon. Illumination is also seen to influence the anodization process in p-type silicon. For  $n^+$  type substrates, the pore patterns formed resemble those grown on  $p^+$  silicon.

The various attempts to model porous silicon formation can broadly be categorized into two, namely (i) Phenomenological theories and (ii) Computer simulations. The phenomenological theories generally aim to provide a qualitative understanding of the pore formation process in terms of competing long-range and short-range phenomena. For instance, the Beale model [12] which will be described in greater

detail in section 2.5 as well as the next chapter, hypothesizes local modifications to the electric field as a result of microscopic irregularities at the acid - semiconductor interface. A host of similar models have been proposed, which have been reviewed in detail elsewhere [2].

There exists another class of models which attempt to obtain a quantitative formalism by examining the stability conditions at the semiconductor surface [67,68]. This approach is patterned on the lines of the classical Mullins-Sekerka stability analysis [69,70]. However, because of the inherent mathematical complexity of the system, such attempts have enjoyed only a limited degree of success.

Another approach, which we wish to employ in tackling the problem of porous silicon formation takes recourse to computer simulations which have been extensively employed in the past to model aggregation and etching phenomena [71]. In the next section (Sec.2.2), we briefly survey existing studies of growth and aggregation phenomena. In section 2.3 we propose a generalized computational scheme termed the drift-diffusion model to simulate the classes of morphologies seen in porous silicon as well as in other processes such as electrochemical deposition (ECD), viscous fingering and amorphous annealing [72]. The results of these simulations are outlined in section 2.4. Section 2.5 constitutes a discussion where we examine the extension of the drift-diffusion model to the case of porous silicon formation. The subsequent chapter describes various phenomenological models proposed earlier to explain porous silicon formation and extends our computational model to simulate the specific instance of silicon anodization in HF.

## 2.2 Existing Models of Aggregation and Etching

The studies of various morphologies obtained in aggregation phenomena such as electrochemical deposition, viscous fingering, bacterial colony growth etc., have attracted a great deal of attention since the early eighties [73]. In electrochemical deposition experiments, two parameters, the electrolyte concentration ( $C$ ) and the applied potential ( $V$ ) are tuned to obtain (i) dendritic structures, both thick and needle like (or stringy); (ii) Dense branching morphologies (DBM) (also known in literature as Eden trees [74]), which are homogeneous and (iii) randomly ramified self similar structures as in diffusion limited aggregation(DLA) [75,76]. In a Hele-Shaw cell, similar transi-

tions are observed when the pressure and surface tension are varied [77]. In silicon, anodic etching gives rise to differing pore morphologies depending on the anodization potential and the substrate doping level [11,12], as described earlier in Sec. 1.2.

A first principles explanation of such phenomena will have to encompass (i) the diffusive field, (ii) the Laplace field, (iii) convective processes and (iv) surface tension, curvature and underlying anisotropy effects. Hence, even numerical solutions may prove difficult. Simple formal approaches have been attempted for obtaining stability conditions at the interface [69,78,79]. It has been hypothesized that the emergence of different characterizing length scales is the result of the interplay between the Laplace and diffusion fields governing the growth process in ECD [79]. Early phenomenological models for PS formation (to be described in detail in the next chapter), also invoke two scales in the form of a depletion layer width at the PS - HF interface and a barrier lowering at the pore tips depending on the curvature.

It is in this context that the statistical models which can simulate physical processes taking place in a large system become relevant. The modeling of complex growth phenomena has become increasingly possible with the advent of fast computers. Simple statistical algorithms have been able to reproduce the patterns obtained in varying phenomena like amorphous annealing and dielectric breakdown [77]. Some of the simplest "growth" laws proposed in literature [71] are outlined below. In these models, the central seed on a lattice can grow by

1. Random occupation of a surface site (i.e., nearest neighbor site) of the seed. This is known as the Eden model [80], which results in compact clusters.
2. The ballistic transport (i.e., movement in a straight line) of a particle generated at a randomly chosen site on the lattice boundary to the seed surface. This is called ballistic deposition.
3. The diffusive transport (i.e., a Brownian random walk) of a particle generated at a randomly chosen site on the lattice boundary to the seed surface. This is labeled diffusion limited aggregation [81].

Ever since the diffusion limited aggregation (DLA) model was suggested in 1981, a great deal of attention has been devoted to developing variations of the algorithm. Patterns generated by the DLA were found to resemble the growth geometries obtained in electrochemical deposition, dielectric breakdown and viscous fingering. The

present work constitutes a generalization of the DLA. We first outline the algorithm for the diffusion limited aggregation process:

1. Start with a central seed on a lattice.
2. A particle is launched on a random walk from a randomly chosen site on the lattice boundary (the step size of the walk should be much smaller than the lattice size).
3. When the particle comes into contact with the seed (i.e., walks into a nearest neighbor site of the seed) the random walk is stopped and the particle is added to the seed.
4. Steps 2 and 3 are repeated

This algorithm employs no controlling parameters. The resulting pattern can be characterized by the fractal dimension  $d_f$  [71,82] defined as

$$M = R^{d_f}$$

where  $M$  is the mass of the aggregate (the total number of particles) and  $R$  the radius of the cluster. For the DLA pattern this was found to be approximately 1.7 [73]. This is in good agreement with the fractal dimensions calculated for zinc leaves obtained in electrochemical deposition experiments at very large dilutions.

Generalizations of the DLA have been attempted by the introduction of additional parameters into the model. Surface tension effects have been modeled by the incorporation of a sticking probability at the aggregate surface [83]. In this model, a particle is allowed to stick to the cluster only after  $n$  contacts. Here,  $n$  is a scale characterizing surface tension effects. With increasing value of  $n$ , a transition was observed from the low density fractal clusters to regular patterns exhibiting a compact structure.

Yet another scale to represent the particle concentration can be introduced by employing a multi-walker algorithm [84] wherein several walkers are released simultaneously from the lattice boundary, instead of a single particle as in DLA. The number of particles at the lattice boundary is maintained constant throughout the simulation. This is indicative of a constant particle concentration at the boundary. Recently, a multi-walker DLA model has been proposed [85] wherein two parameters, namely

the particle concentration  $\rho$  and the width of a “migrational envelope”  $l$  are tuned to obtain dense branching morphologies as well as DLA patterns. In this simulation, the particles undergo diffusive motion outside the migrational envelope. On reaching the envelope, they migrate to the nearest point on the aggregate surface. The migrational envelope is continuously modified to maintain a minimum distance  $l$  from the aggregate contour. By varying the values of the parameters  $l$  and  $\rho$  one can obtain a transition from DLA to DBM.

It will be a desirable goal to arrive at a model which can reproduce the various morphologies obtained under different growth conditions as well as the transition from one morphological class to another. From the discussion in the preceding paragraphs, it is clear that the morphological variations result from the interplay of two or more parameters [86,87]. For the sake of simplicity, a minimal set of parameters should be employed. In the next section, we propose a drift-diffusion model which employs the competition between two antithetical parameters to simulate the various morphological classes described in the beginning of this section.

## 2.3 The Drift-Diffusion Model

In the classical DLA model [81] described in Sec. 2.2, a particle starts its random walk at an infinitely large distance from a seed or cluster. The random diffusive motion is terminated the moment it comes into contact with the aggregate cluster. It is conceivable that very close to the aggregate surface, particle movement is no longer controlled by the macroscopic diffusion field, but by microscopic, localized phenomena. To model such processes, additional parameters will have to be introduced into the simulation. We attempt to develop an algorithm which models pattern formation as a result of the interplay of a macroscopic field and localized surface phenomena.

The main control parameters in this model are: (i) a depletion layer width  $\Delta W$  which controls the diffusion and (ii) a drift length  $l$  governing the field driven processes in the proximity of the aggregate. The design of the algorithm is outlined below:

(i) A particle is launched from a randomly chosen lattice site beyond the depletion layer boundary which is at a distance  $\Delta W$  from the surface of the aggregate. This is illustrated in Fig. 2.1. We begin with a circular depletion zone of radius  $\Delta W$  around a central seed. As the aggregate grows, the depletion zone boundary is modified to

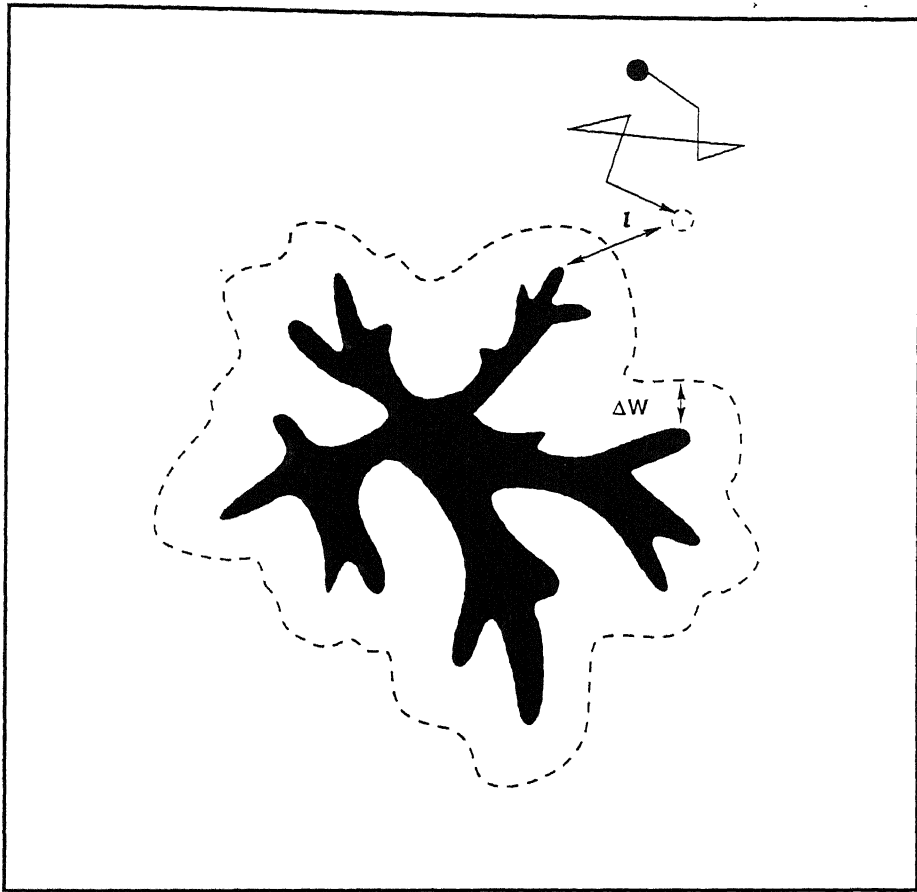


Figure 2.1: The drift-diffusion model. A particle is released beyond the depletion layer boundary (the closed curve) which dynamically follows the aggregate (solid circle cluster) contour at a distance  $\Delta W$ . When the particle wanders to within a radius  $l$  (see dotted arrow) of the aggregate surface, it is “field driven” to become a part of the cluster. Note that the figure depicts the case  $l > \Delta W$ .

follow the aggregate contour at a distance  $\Delta W$  as shown in the figure.

(ii) The particle executes a random walk as in ordinary off-lattice DLA algorithms [88,89]. A circular contour (of small radius compared to the lattice size) is drawn around the the particle. The particle is then moved at random to any of the lattice sites which fall on this contour.

(iii) The moment a part of the aggregate surface is encountered within a radius  $l$  of the particle location, the random walk is terminated. The particle is then moved to the surface (in a sense. “field driven”) and becomes part of the aggregate.

(iv) Steps (i) - (iii) are repeated.

The simulations were stopped when the aggregate had grown to a diameter of around 400 units, one unit being the diameter of a single particle. Approximately  $10^4 - 10^5$  particles had to be launched for various cases.

The two control parameters employed in this simulation have also been suggested, albeit separately, elsewhere in literature. To model porous silicon formation, a “finite diffusion length” similar to our  $\Delta W$  has been proposed [90]. The drift length  $l$  in our simulation is in a way similar to the width of the “migrational envelope” of Erlebacher *et al.* [85,91]. Our algorithm interpolates between existing growth models in various limiting cases. In the limit  $l = 1$  and  $\Delta W \rightarrow \infty$ , the algorithm is identical to the DLA.  $\Delta W = 0$  and  $l = 1$  approximates the Eden limit described in Sec. 2.2. As  $l$  becomes larger than  $\Delta W$  (the case depicted in Fig. 2.1), a fraction of the generated particles are directly transported to the surface without undergoing diffusion. This is akin to ballistic deposition (see Sec. 2.2). When  $l \gg \Delta W$ , the ballistic process dominates the diffusive process.

## 2.4 Results

Fig. 2.2 depicts the variety of morphologies obtained with varying  $\Delta W$  and  $l$ . For small  $l/\Delta W$ , we obtain DLA like patterns (Fig. 2.2a). A simple mass-radius scaling calculation for this pattern yielded a fractal dimension of  $1.65 \pm 0.05$ . Stringy structures similar to those reported in electrochemical deposition at high voltages [75] are seen in the large  $\Delta W$  limit with  $l/\Delta W \simeq 1$  (Fig. 2.2b). The mass-radius scaling exponent fluctuates around  $\sim 1.45$  for this pattern. The stringy morphology observed in some experiments is essentially one dimensional in character [76]. This is reproduced for very large  $\Delta W (= l) > 25$ . As  $\Delta W (= l)$  is increased, the scaling exponent approaches unity (see Fig. 2.3). On the other hand, for small  $\Delta W$  and  $l/\Delta W \simeq 1$ , we obtain short dense branches exhibiting a relatively smooth front which remains nearly circular throughout the growth period (Fig. 2.2c). This has been identified in experimental literature as homogeneous or tip splitting patterns or dense branching morphologies [75,76,78,92]. The mass radius scaling for these structures resulted in a fractal dimension  $\simeq 2$ . For  $l/\Delta W \geq 3$ , thick dendritic growths with side branching was obtained (Fig. 2.2d). For large  $\Delta W (> 5)$ , the patterns become too inhomogeneous to show any well defined scaling [75]. However, for small  $\Delta W$ , the model

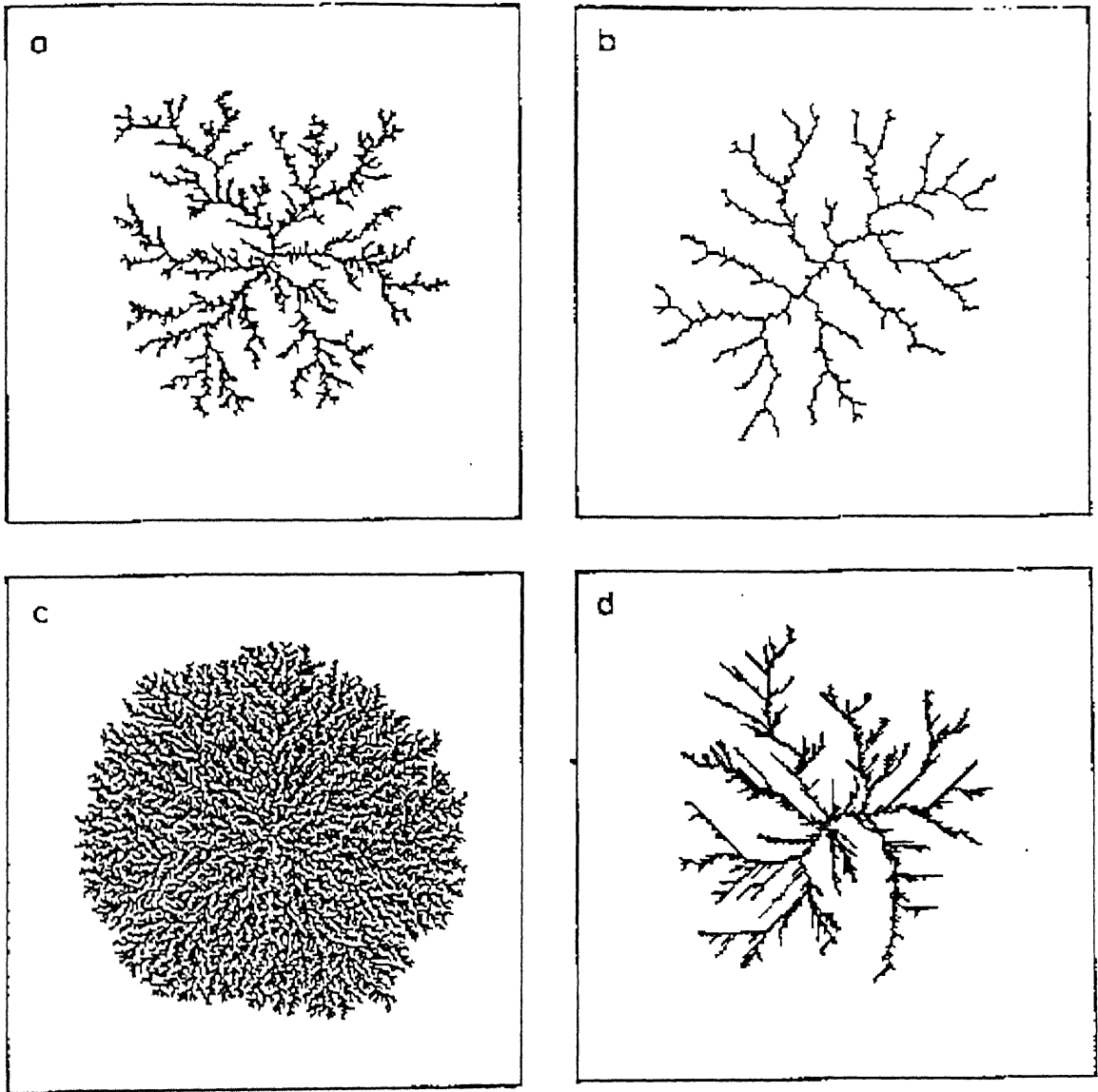


Figure 2.2: The simulated growth patterns obtained by varying the depletion width ' $\Delta W$ ' and drift length ' $l$ '. (a) Patterns resembling DLA ( $\Delta W = 10$ ,  $l = 2$ ), (b) stringy structures ( $\Delta W = 10$ ,  $l = 10$ ), (c) homogeneous, dense branching morphologies with a nearly circular growth front ( $\Delta W = 2$ ,  $l = 2$ ) and (d) thick dendritic growth with side branches ( $\Delta W = 8$  and  $l = 24$ ).

approaches the Eden limit and the resultant patterns are somewhat homogeneous.

The occurrence of dendritic growth (see Fig. 2.2d) in such a simulation is sur-



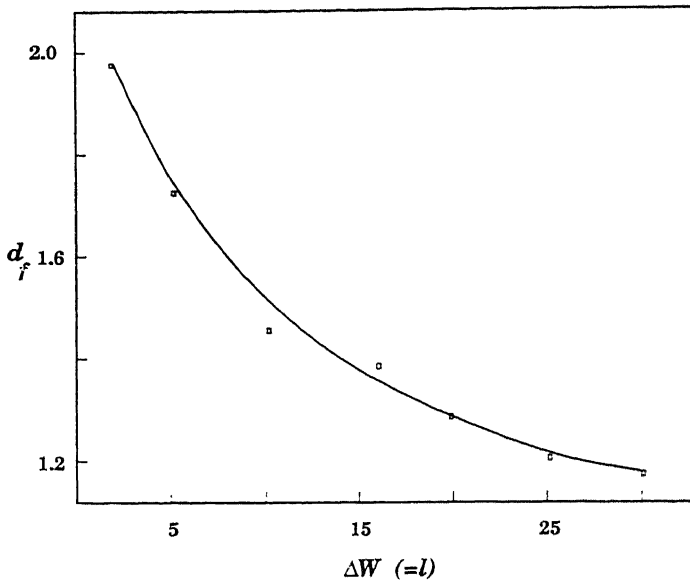


Figure 2.3: The fractal dimension  $d_f$  plotted against  $\Delta W$  (in lattice units) with  $l$  equal to  $\Delta W$ .  $d_f$  is seen to approach unity in the large  $\Delta W (=l)$  limit.

prising, since it is well understood that anisotropy is required in the interfacial dynamics for side branching to occur [77]. The present algorithm admits an underlying anisotropy in the way a particular surface site is chosen, when more than one point on the aggregate surface falls within a radius  $l$  of the random walker. This selection was done in three ways. (i) The nearest site was chosen. (ii) A site was chosen at random. (iii) The site nearest to the radial line connecting the random walker and the central seed was chosen. The morphologies remained similar for the case  $l \leq \Delta W$ . The three methods yielded different results in the limit  $l \gg \Delta W$ . Dendritic growth was observed only in case (iii), which corresponds to the imposition of a preferred radial field. In the case of electrodeposition, this could be interpreted as the applied radial electrostatic field.

Figures 2.3 and 2.4 show the variation in the mass-radius scaling exponent  $d_f$  with varying values of  $\Delta W$  and  $l$ . As  $\Delta W$  is kept equal to  $l$  and varied,  $d_f$  decreases steadily with increasing  $\Delta W (=l)$  and approaches unity. This is depicted in Fig. 2.3 and represents the emergence of stringy structures as shown in Fig. 2.2. The values obtained for various  $\Delta W$  when  $l$  is kept constant ( $l = 2$ ) are plotted in Fig. 2.4. The dimension  $d_f$  is seen to vary from 2.00 to  $1.65 \pm 0.05$  as  $\Delta W$  goes from very small ( $\sim 1$ ) to large ( $> 15$ ) values. This illustrates a smooth transition between Eden type

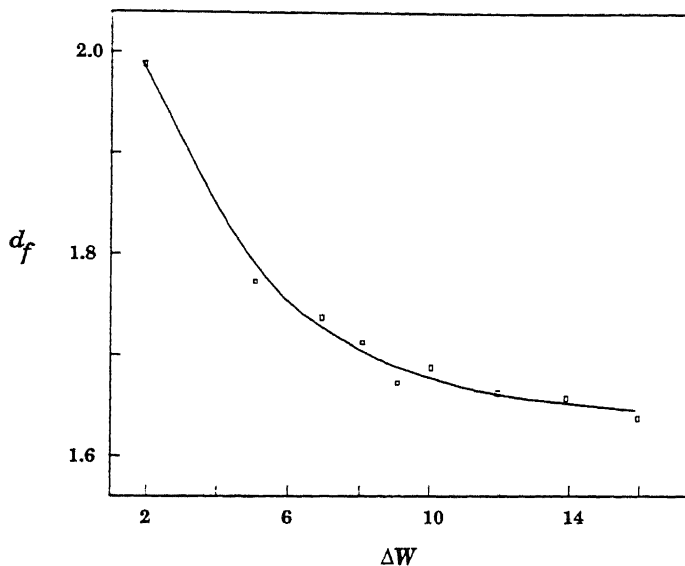


Figure 2.4: The fractal dimension  $d_f$  plotted against  $\Delta W$  (in lattice units) with  $l = 2$ . For small  $\Delta W$ ,  $d_f \simeq 2$  (see Fig. 2.2c), which is indicative of compact clusters. In the large  $\Delta W$  limit,  $d_f$  stabilizes at  $1.65 \pm 0.05$  (see Fig. 2.2a).

growth and DLA.

Fig. 2.5 codifies our observations into a “phase” plot <sup>1</sup>. The plot was constructed on the basis of approximately a hundred patterns, grown to aggregate diameters of around 400 units. The transitions from one phase to another being continuous, the boundaries are not rigidly defined. For example, in the  $l \gg \Delta W$  case, the dendritic patterns observed at large  $\Delta W$  become denser and more homogeneous as  $\Delta W$  approaches zero. The phases depicted have been reported earlier in electrochemical deposition experiments [75,76] and related processes [77].

## 2.5 Discussion

One can explore the phenomenological relevance of the parameters  $\Delta W$  and  $l$ . The existence of competing processes in electrochemical deposition and other phenomena is well established. The phase diagrams reported by Sawada *et al.* [75] and Grier *et al.* [76] represent various morphological classes resulting from varying the concentration and applied voltage. Assigning a direct correlation between our parameters and the

<sup>1</sup>the term “phases” is taken to mean classes of aggregates as reported earlier in literature

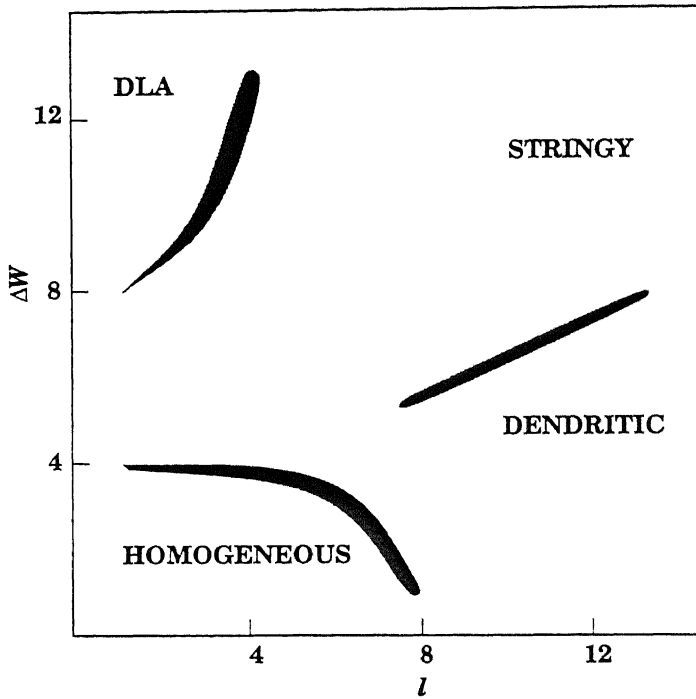


Figure 2.5: “Phase” plot of patterns observed in the simulations. The phases depicted transform into one another when the parameters  $\Delta W$  and  $l$  are varied. The boundaries must not be treated as rigidly defining a transition and are hence depicted by shaded regions. Both  $\Delta W$  and  $l$  are expressed in terms of lattice units.

experimental parameters based on a comparison between the phase diagrams of the simulation and experiment is difficult. In all probability,  $\Delta W$  and  $l$  are functions of concentration, applied voltage and the interface effects. We shall further explore the significance of these parameters in the anodization of silicon in the next chapter.

In the diffusion field versus drift field dynamics governing growth in our simulation,  $\Delta W$  is a control parameter for the macroscopic diffusion field, whereas  $l$  models microscopic surface effects. An example of a phenomenological model employing similar arguments is the Beale model [12] (this is discussed in greater detail in the next chapter) for porous silicon formation which hypothesizes the existence of a semiconductor depletion layer at the Si-HF interface. The width of this depletion layer varies as

$$\Delta W \propto \left[ \frac{(V_{BI} - V_A)}{n_0} \right]^{\frac{1}{2}} \quad (2.1)$$

where  $V_A$  is the anodization potential,  $V_{BI}$  is a constant built in voltage and  $n_0$  is

the substrate doping level. On the other hand, the parameter  $l$  can be related to the barrier lowering ( $\Delta\phi_s$ ) due to microscopic surface irregularities. This lowering,  $\Delta\phi_s \propto \sqrt{E_s}$ ,  $E_s$  being the enhanced local electric field. For planar interfaces,  $E_s \propto \phi_s/\Delta W$  where  $\phi_s$  is the overall barrier height. Due to surface irregularities, this height is enhanced locally as

$$E_s \propto \frac{\phi_s}{(\Delta W - l)} \quad (l < \Delta W) \quad (2.2)$$

As  $l \rightarrow \Delta W$ ,  $E_s$  is very large at the tips, leading to stringy patterns. In a recent work [93], it has been shown that  $\Delta W$  and  $l$  can be correlated to the depletion layer width and barrier lowering given in equations (2.1) and (2.2).

Several studies of two dimensional growth on a one dimensional substrate have been reported in the past. Matsushita *et al.* have grown zinc “trees” on a linear carbon cathode [94]. Such processes have also been modeled using a DLA like algorithm [95,96]. There exists a diffusion limited annihilation model [97] where a diffusing particle etches away a site on a flat surface. The etching process in porous silicon may also be viewed similarly. One approach [90] has been to introduce a “diffusion length” which is defined on similar lines as  $\Delta W$  in the drift-diffusion model. The muti-walker model of Erlebacher and coworkers has also been extended to model silicon dissolution [91]. In the next chapter, we attempt to extend the drift-diffusion model to porous silicon formation by using a linear substrate which is represented by a side of the lattice. The deposition is no longer radial, but “quasi-one dimensional”.

In a sense, the two scales  $\Delta W$  and  $l$  are antithetical, one separating the particle from the aggregate, the other driving it towards the aggregate. Various growth models (DLA, ballistic deposition, Eden) can be obtained as limiting cases of this algorithm. We stress that the two scales do not contain any *a priori* bias towards any specific morphological structure. Nevertheless, a variety of distinct morphological structures observed in experimental growth and dissolution is obtained in our simulation.

## Key Reference

The major reference for the material contained in this chapter is:

- George C. John and Vijay A. Singh, Phys. Rev. E **53**, 3920-3924 (1996).

# Chapter 3

## Porous Silicon Formation: The Diffusion Induced Nucleation Model

### 3.1 Introduction

As mentioned earlier, porous silicon is formed during the anodization of silicon in HF acid. The formation of diverse pore structures rather than a uniform 'peeling off' of the silicon layer presents an intriguing problem. One needs to explain the preferential pore formation in comparison to a uniform etch, as well as the observed transition in morphologies with varying experimental parameters. The early phenomenological theories sought to accomplish this in a qualitative fashion, by means of arguments premised on a particular model of the semiconductor - electrolyte interface.

The majority of the growth models proposed to explain pore growth in silicon do not concern themselves with the exact dissolution chemistry, but invoke physical arguments to explain the influence of anodizing conditions on porous silicon morphologies. This is because of the fact that the detailed dissolution chemistry of silicon is complex and not well understood. Several dissolution mechanisms have been proposed, an excellent review of which is found in the article by Smith and Collins [11].

In the Si - HF system of interest to us, the etching process can be influenced by a variety of factors such as (i) the electrochemistry of dissolution, (ii) the semi-conducting properties of silicon, (iii) transport of carriers in the semiconductor, (iv)

transport of ions in the electrolyte and (v) surface phenomena in the form of irregularities on the silicon surface or the surface tension of the liquid. The Si-HF system is forward biased when a p-type Si substrate is used as the anode. In n-type silicon, pore formation occurs only when some extraneous hole generation processes such as intense illumination or high electric fields are invoked. This seems to suggest that the presence of holes is essential for porous silicon formation.

A substantial amount of work has been done on diffusion limited models in the last decade and a half [71.88.98]. The recent models of porous silicon formation have been based on detailed computer simulations of diffusive carrier transport within silicon and are briefly reviewed in section 3.3. These models are premised on similar lines as the diffusion limited aggregation (DLA) which has been described in the previous chapter.

The drift-diffusion model outlined in chapter 2 is successful in reproducing the morphological classes observed in diverse growth phenomena. These patterns bear considerable resemblance to the pore morphologies in silicon. For instance, the dense branching morphologies seen in Fig. 2.2c are similar to the highly interconnected network of pores obtained with p-type substrates. The stringy structures (Fig. 2.2b) are characteristic of n-type silicon substrates, where pores grow in a relatively linear fashion. In degenerately doped silicon, thicker pores are obtained which resemble the  $\Delta W < l$  case of the drift-diffusion model (Fig. 2.2d). However, one would like to go beyond a picture-to-picture comparison and evolve a model which should be capable of explaining other features of the experimental growth process as well. Some of these are:

- Rate of growth: The porous layer is reported to exhibit a constant growth rate, with the velocity of the pore front remaining independent of time [99.100]. Further, one would also like to explore the dependence of the growth rate on the experimental parameters such as the anodization potential, electrolyte concentration etc.
- Porosity profile: PS exhibits a constant porosity vs. depth profile with a sharp planar film front [101]. Considering the strong dependence of visible luminescence on porosity, it would be desirable to have a model which can predict the variation in porosity with experimental conditions.

- “Piping”: At high anodic potentials, the linear pores formed on n-type substrates widen and become pipe-like [11]. This phenomenon is known as “piping” and is not well understood.
- Electropolishing: Silicon, both p and n-type, are seen to be uniformly etched away at high voltages, instead of forming porous silicon. This phenomenon, termed “electropolishing” is also seen to occur at low electrolyte concentration ( $\sim 10\%$ ).

In this chapter, we extend the drift diffusion model outlined in chapter 2 to the Si-HF system, based on a careful examination of the earlier phenomenological theories. We attempt to pick out the key processes and incorporate them into the algorithm. Two simple processes are identified as contributing to the primary dissolution mechanism, namely (i) the diffusion of holes from the bulk towards the Si-HF interface, and (ii) further propagation of a pore from the site of dissolution with a finite termination probability  $p_t$  (a nucleation process). The model incorporating these two processes, termed the diffusion induced nucleation (DIN) model is described in section 3.4. The various parameters and their numerical values are justified on the basis of physical arguments. Section 3.5 illustrates the different morphologies obtained using the algorithm and compares them with experimentally grown porous silicon structures. Section 3.6 constitutes a discussion, where experimental observations like the rate of growth of the film, variations in the pore diameters and electropolishing are compared with the results of the simulation. Some experiments for further study and elucidation are suggested.

## 3.2 Phenomenological Theories

Most of the early models of porous silicon formation are based on the I-V characteristic of the dissolution process. The general I-V behavior for the Silicon-HF system [11] is briefly summarized below (see Fig. 3.1):

(i) Porous silicon formation occurs in zone A, when the current  $I$  is less than the value at the first peak  $I_{PS}$ . Zone B is a transition region to the electropolishing regime depicted as zone C.

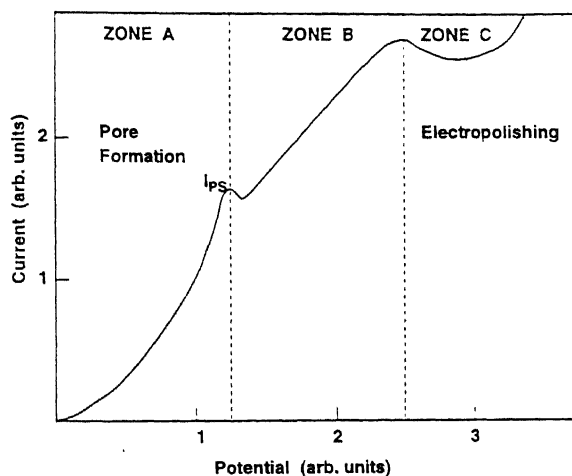


Figure 3.1: Typical I-V characteristic (schematic) for anodization of p-type silicon in HF. The three zones represent the pore formation regime, a transition region and the electropolishing regime.

(ii) Since Si is the anode, the system is forward biased for p-type silicon, whereas for n-type silicon it is reverse biased. Rectifying behavior is observed in both cases.

(iii) Under illumination, n-type and p-type Si exhibit similar I-V characteristics. For the heavily doped case (i.e.,  $n^+$  and  $p^+$ ) the characteristics are similar even under dark conditions.

(iv) In the porous silicon formation region (zone A), the curve is exponential.

Several models for porous silicon formation proposed in the last decade try to correlate these facts to the complex pore morphologies observed in silicon. The most prominent of these is perhaps the Beale model [12]. This model assumes that a current flow is necessary for porous silicon formation, with Si as the anode. In p-type silicon this is easily possible as the Si-HF system will be forward biased. But for n-type silicon which will be under a reverse bias, current flow requires intense illumination or high voltages which can cause breakdown. The current flow in silicon is localized as a result of surface inhomogeneities. This leads to a non-uniform dissolution of the surface, initiating pores.

The semiconductor - electrolyte system is modeled as a Schottky interface (Fig. 3.2) by Beale and coworkers [12], and some others [102]. The etched surface supports several surface states which can act as traps for carriers. The high density of surface states results in the pinning of the Fermi level in the mid-gap. This acts



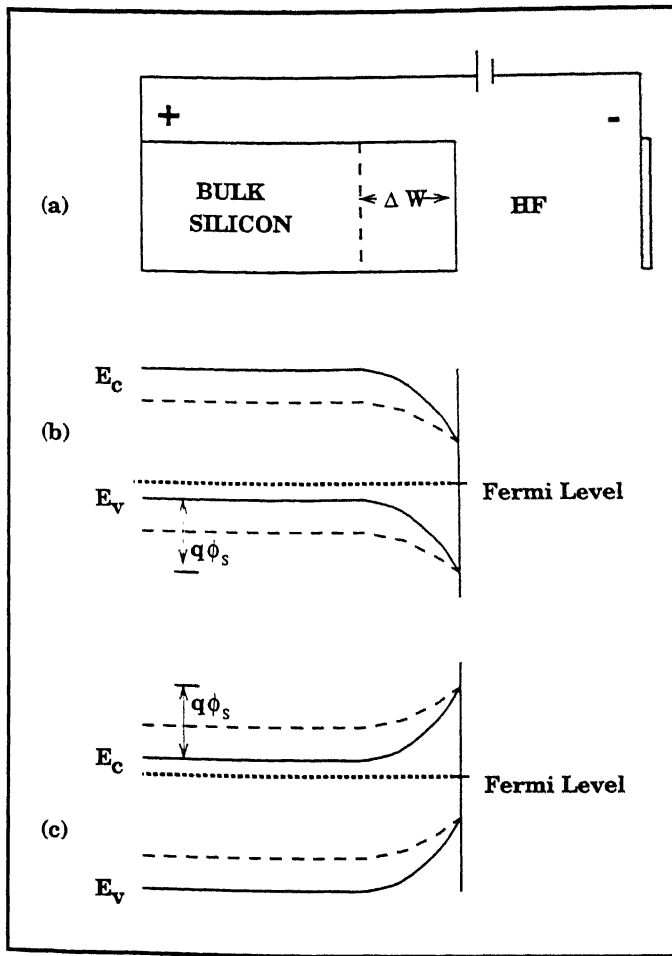


Figure 3.2: (a) Representation of the semiconductor - electrolyte system according to the Beale model [12]. Energy band diagrams are drawn assuming a Schottky barrier for (b) p-type Si, (c) n-type Si. The solid lines represent the conduction ( $E_c$ ) and valence ( $E_v$ ) bands without any anodizing potential. The dashed lines show barrier raising (lowering) after a potential is applied. The Fermi level (dotted line) is assumed to be pinned to the mid-gap at the interface because of the high density of surface defects.

as a barrier for current flow and can explain the observed rectifying behavior.

Carrier transport across the barrier can then occur through thermionic emission or by tunneling. In the case of lightly doped Si, the tunneling probability is small and hence the current flow is determined mainly by thermionic emission, which is controlled by the barrier height. The barrier height depends on the applied bias as well as the local electric field distribution. Charges near the barrier produce image

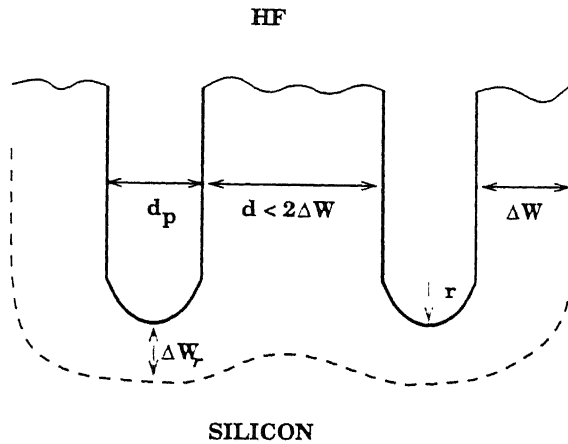


Figure 3.3: The “pinch off” effect due to the overlap of depletion layers (of width  $\Delta W$ ) associated with adjacent pores. The pore diameter is  $d_p$ , the pore tip radius is  $r$ . Note the reduction in the depletion layer width around the pore tip ( $\Delta W_r < \Delta W$ ).

charges in the electrolyte, thereby enhancing the local electric field. The barrier lowering is hence,

$$\Delta\phi_i = q(E_s/4\pi\epsilon_s\epsilon_0q)^{1/2}$$

where  $E_s$  is the electric field at the interface,  $\epsilon_s$  is the relative permittivity of silicon,  $\epsilon_0$  is the permittivity of vacuum, and  $q$  is the carrier charge. For a planar barrier with a depletion layer width  $\Delta W$ ,  $E_s$  is given by

$$E_s = 2\phi_s/\Delta W$$

where  $\phi_s$  is the barrier height. Around a surface irregularity which can be modeled as a hemispherical tip of radius  $r$ , ( $\Delta W \gg r$ ) this becomes (Fig. 3.3)

$$E_s = \phi_s/r$$

Thus we see that there is a considerable field enhancement at regions of high curvature. This leads to enhanced silicon dissolution as a result of increased local current.

For heavily doped silicon, the Si-HF system conducts in both directions. The behavior is non-ohmic. This is best explained by the theory that carrier transport is then governed by carrier tunneling and not thermionic emission over the barrier. In this case, the current is not controlled by the barrier height, but by the width (*i.e.*

the width of the semiconductor depletion layer) which can be written as

$$\Delta W = (2\epsilon_s \epsilon_0 \phi_s / q N_c)^{1/2} \quad (3.1)$$

where  $N_c$  is the carrier concentration. According to Eq. (3.1), the depletion layer width will be small for degenerately doped silicon. As in the case of lightly doped silicon, field enhancement around the pore tips can locally reduce the depletion layer width. Modeling the tip as a hemisphere of radius  $r$ , the width of the hemispherical barrier  $\Delta W_r$  is given by

$$1 - \left( \frac{\Delta W_r}{\Delta W} \right)^2 = \frac{2}{3} \left( \frac{\Delta W_r}{\Delta W} \right)^3 \frac{\Delta W}{r} \quad (3.2)$$

The depletion layer width thus acts as a regulating parameter for the pore growth. When depletion layers associated with adjacent pores overlap (Fig. 3.3), there is a pinch off effect, leading to depleted pore walls. This results in increased resistance of the porous layer, and the current preferentially flows down the electrolyte. The porous film is thus stable against further dissolution. This pinch off can also lead to a columnar pore structure which is observed for n-type substrates. However, perturbations due to defects and grain boundaries can redirect the pore growth.

If a pore outgrows its neighbors, tunneling can occur over an increased area of the tip, leading to a larger tip radius. This, in accordance with Eq. (3.2), results in a larger depletion layer, which serves to limit carrier tunneling resulting in a slowing down of the rate of growth. Such a regulating mechanism is considered responsible for the more or less planar porous film front.

The Beale model, described so far in this section, is thus constructed in terms of familiar semiconductor device physics, not accounting for the electrochemical reactions at the surface. In an attempt to explain pore growth in n-type silicon, Zhang [102] also takes recourse to a depletion layer as the controlling parameter. Carrier transport is assumed to take place through tunneling across the barrier. If a potential much higher than  $kT$  is applied, band bending occurs, which reduces the depletion layer width. The model is much the same as that of the Beale model and assumes that pore tips (irregularities) cause band bending leading to an enhanced current. A maximum limit is set on the pore wall thickness, which is twice the depletion layer width (Fig. 3.3) This is a consequence of the pinch off effect due to the depletion layer overlap. The main difference from the Beale model is that Zhang invokes carrier tun-

neling even in lightly doped silicon, whereas the Beale model assumes thermionic emission as the major carrier transport mechanism.

These models are consistent with the following experimental observations: Increase in dopant concentration leads to shorter pores with less spacing between them compared to the lightly doped case. The semiconductor depletion layer width  $\Delta W$  varies inversely with  $\sqrt{N_c}$  as indicated in Eq. (3.1). Besides, as the HF concentration is increased, the pore becomes narrower. This is expected, as the current at the pore tips increase. Also, p-type silicon has a much smaller depletion layer compared to n-type which can give rise to narrow and uniform pores. However, p-type silicon produces an interconnected network of pores which such models cannot satisfactorily explain.

Both the above models share the idea of a depletion layer, which is substantiated further by others [103]. An alternate theory exists [104,105], which assumes the formation of a passivating layer on the Si-HF interface. In this case, the etching is limited by the local dissolution of the layer. The pore formation dynamics is controlled by the competition between the growth and the dissolution of the passive layer. Analytical and numerical calculations on this model have been successful in reproducing the observed morphological variations with changes in the applied voltage  $V$  and the HF concentration. However, the pore wall thickness  $d$  is found to be strongly dependent on the doping concentration. This cannot be satisfactorily explained by this model.

An appealing model to explain the pore wall thickness is the quantum confinement model, proposed by Lehmann and Gosele [103,106–108]. The basic idea of this model is that as a result of carrier confinement in the nanostructures formed during silicon dissolution, there is a band gap enhancement. Only those carriers with energies high enough to overcome this barrier can now be present in the crystallite. This results in hole depletion in the porous structure. As holes are essential for dissolution, no further etching occurs.

We have seen that a simple depletion type model sets an upper limit on the wall thickness of the porous silicon film. Similarly, the quantum confinement effects are responsible for setting a lower bound on the crystallite size. According to Lehmann and Foll [99], the macropores formed in n-type silicon are covered with microcrystallites on the pore sides. The size of these microcrystallites could be limited by

quantum confinement. However, there exists other reports which indicate that this picture of n-type porous silicon is not necessarily true [11]. Reports of a possible fractal structure also exist [11], though this is contested by Lehmann and coworkers.

It is evident that the quantum confinement model cannot be regarded as a primary mechanism for porous silicon formation. At best, it is a secondary effect putting a lower bound on the crystallite size. For the onset of pore formation, a depletion layer seems to be necessary, the width of which controls many large scale features of the final morphology. However, it could be argued that in p-type silicon, the space charge region has a very small width, and hence the quantum confinement effects can play a major role.

The semiconductor depletion layer is functionally equivalent to a passivating layer, which can prevent dissolution of the pore walls. Thus we see that the semiconductor depletion layer, the passivating oxide layer and the nanocrystallites with an enhanced gap serve the same function, namely create a carrier depletion at the surface. In short, one can view this depletion layer width as a control parameter which serves to "push" the pores apart. This is reminiscent of the role of the depletion parameter  $\Delta W$  in the drift-diffusion model of chapter 2, which serves to keep the diffusing particle away from the aggregate. The idea of such a depletion layer has been gainfully employed by several computer simulation studies of porous silicon formation, which we shall now examine.

### 3.3 Computer Simulations of Porous Silicon Formation

Diverse patterns are observed in natural processes such as dielectric breakdown, viscous fingering and electrochemical dissolution [88] which have been successfully modeled using the diffusion limited aggregation (DLA) model described in the previous chapter. Since the pore morphologies in porous silicon appear to resemble the DLA patterns, several diffusion limited mechanisms have been proposed to model porous silicon formation.

In a computer simulation, Smith, Chuang and Collins [90] assume that the diffusion of an 'electro-active species' (holes) from the bulk to the Si-HF interface is the controlling factor in porous silicon growth. The bulk silicon is represented by a two

dimensional rectangular lattice of sides  $M \times N$ . Periodic boundary conditions are implemented in the lateral directions, which means that a particle 'walking off' one side of the lattice reappears at the opposite side. This algorithm, termed the "finite length diffusion model" is briefly described below:

(i) A hole is released from an isoconcentration surface within the lattice. This is similar to the depletion layer boundary of the drift diffusion model (see Fig. 2.1 on page 27). The isoconcentration surface is constituted by the locus of all points at a distance  $\Delta W$  from the Si-HF interface (in this case, a side of the square lattice).

(ii) The hole executes an on-site random walk on the lattice, till it contacts a surface site. Then that surface site is dissolved with the annihilation of the hole.

(iii) The isoconcentration surface is modified to follow the contour of the freshly dissolved surface.

(iv) Another particle is released from the isoconcentration surface. Steps (ii) and (iii) are repeated.

The pore geometries resulting from this simulation bear some resemblance to TEM micrographs of porous silicon. The morphological features were controlled by the parameter  $\Delta W$ , which Smith and coworkers assume to be a diffusion length. The pore spacing is found to depend on  $\Delta W$  because of the following reason. When two pores are separated by a distance less than or equal to  $2\Delta W$ , the isoconcentration surfaces associated with each overlap. Now the holes released from this surface have a much lesser probability of reaching a site deep in the resulting wall like structure. This phenomenon is similar to the pinch-off effect caused by the depletion layer overlap in the Beale model (Fig. 3.3). Smith and Collins claim [11] that the diffusion length is in a sense related to the width of the semiconductor space charge region.

One can also perceive an in-built mechanism wherein the hole diffusion is preferentially directed towards the pore tips. The sites at the tips sample a greater extent of the isoconcentration contour (depletion layer boundary) than a site on the pore sides, because of reduced interference from other surface sites. Therefore, the pore tips grow much faster, resulting in a uniform density of the porous film.

This model does not yield the high porosity values observed in the case of light emitting porous silicon. The maximum reported values in the simulation are around 40%. Besides, the pores are never interconnected as in the case of p-type porous silicon. The model does not produce wide pores which are seen in the 'piping' phe-

nomena in n-type silicon [11] described earlier in Sec. 3.1.

This model is functionally similar to the Beale model, though it avoids many of its assumptions such as pinning of the Fermi level at mid-gap and the oversimplified model of a Schottky barrier at the semiconductor electrolyte interface. For a comparison between the two models, we refer the reader to the review article of Smith and Collins [11]. The microscopic features are better modeled by the diffusion limited scheme. This model also predicts a fractal to non-fractal transition at a depth  $\Delta W$  from the surface of the porous film [109]. Experimentally it is known that porous silicon consists of a nanoporous layer at the top and a macroporous layer of uniform porosity below [101]. However, the observed thickness of the nanoporous layer ( $\sim 1\mu\text{m}$ ) is too large to be explained by a simple relation to the diffusion length which is of the order of the nanocrystallite size as seen from the Beale model (Fig. 3.3).

Further, the finite length diffusion model is extremely oversimplified, assuming only one control parameter  $\Delta W$  for the entire process. Therefore, the claim that it is an exact equivalent of the Beale model [11] is invalid, as more parameters would be required to represent the effects of the dopant type, concentration and the electric field. Besides, a simple one to one correlation between parameters of both models as established by Smith and Collins does not seem convincing.

A similar model employing a control parameter  $\rho$ , which represented the concentration was proposed in 1984 by Voss and Tomkiewicz [110] to simulate electrodeposition in metals. There the simultaneous diffusion of a large number of particles was employed, with the population of such walkers being controlled by the parameter  $\rho$ . The same model is applicable for porous silicon formation if we regard the aggregation of particles in an opposite sense, *i.e.*, the removal of sites. The morphologies are similar to those obtained by Smith and coworkers, though a better variation is achieved by employing a second control parameter in the form of a 'sticking probability' at the surface. A random walker, on contacting a surface site may stick to it with a finite probability or continue to walk. At low sticking probability, mossy deposits which resemble the transition region to the electropolishing regime in porous silicon was observed. When the sticking probability was maximum, dendritic growth resulted. Thus a transition between mossy deposits and fully developed dendritic growth was recorded. Note that these parameters are similar to those discussed earlier in Sec. 2.2 for the case of radial growth simulations.

Erlebacher and coworkers [85.91] introduce a two scale model which employs a multi-walker algorithm as described above. They attempt to model the effect of the high electric field focused at the pore tips by a 'migrational envelope' which is constructed as a locus of points equidistant from the pore surface. This follows the contour of the growth front at a fixed screening distance  $l$ . A particle, on contacting the migrational envelope during the course of its random walk is preferentially transported (field driven) to the nearest pore tip, as in the case of the drift-diffusion model. The migrational envelope is claimed to be analogous to the depletion layer in n-type silicon. The other control parameter is the concentration  $\rho$  of particles, which determines the number of holes in the system. The concentration is maintained constant at the edges of the lattice, far from the interface. Particles were not allowed to overlap during the course of their on-site random walk.

Many of the characteristic morphologies of porous silicon are obtained in simulations with low concentration and large screening lengths. Highly directional pores are seen, which do not grow into each other. This is characteristic of porous silicon formed from n-type substrates. The simulation would correspond to illuminating the sample from the back where the carrier concentration due to hole generation will be maintained constant. As the concentration increases, the spacing between the pores decreases. The density profile with depth remains constant. When  $l$  is set to zero, the simulation mimics that of Voss and Tomkiewicz with sticking probability one. The porosity obtained in each simulation was approximately equal to  $\rho$ . If  $\rho$  is taken to represent the hole concentration, such a result is clearly unphysical.

We can also study two dimensional growth on a linear substrate using the drift-diffusion model described in chapter 2. This is achieved by using a linear substrate which is represented by a side of the lattice. The deposition is no longer radial, but "quasi-one dimensional." Fig. 3.4 depicts the dependence of the mean aggregate density on the drift length  $l$ . Deposits were grown on a linear substrate of length 300 units for a given  $\Delta W$ . A cross-over behavior is discernible, with a minima at  $\Delta W = l$ . This can be understood in terms of our phase plot (Fig. 2.5 on page 32). The minima corresponds to the stringy region, where  $\Delta W \simeq l$ . On either side of the stringy phase, there exists phases of higher density. A similar behavior is seen in porous silicon where transitions are observed from a uniform network of thin pores to shorter, wider pores on increasing the doping level in the substrate [12]. On the other



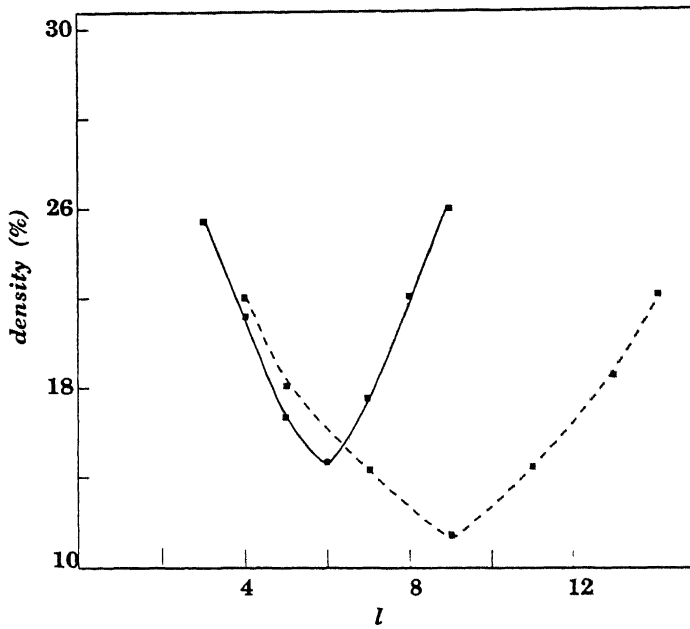


Figure 3.4: Plot of the percentage aggregate density vs.  $l$  (in lattice units) obtained in deposition on to a linear substrate of length 300 units. The two curves are for  $\Delta W = 6$  (solid line) and  $\Delta W = 9$  (broken line). In each case, a minimum is observed at  $\Delta W = l$ .

hand, increasing the applied potential leads to the formation of thick and relatively linear pipe-like pores [11]. These similarities suggest that the drift-diffusion model can be extended to model porous silicon formation.

The computer simulations with an underlying diffusion limited process are thus seen to premise some kind of a depletion zone similar to the concept of the semiconductor depletion layer which is invoked extensively in the phenomenological theories of Sec. 3.2. However, to produce the complex pore geometries of porous silicon, it is quite evident that other competing mechanisms must also be at work. For instance, the formation of an interconnected network of pores as seen in p-type silicon is forbidden by this very “depletion layer” which tries to keep them separate. Hence we introduce a pore propagation probability which allows an etched site to propagate at random with a finite probability. Such a diffusion induced nucleation model (DIN) is outlined in the next section.

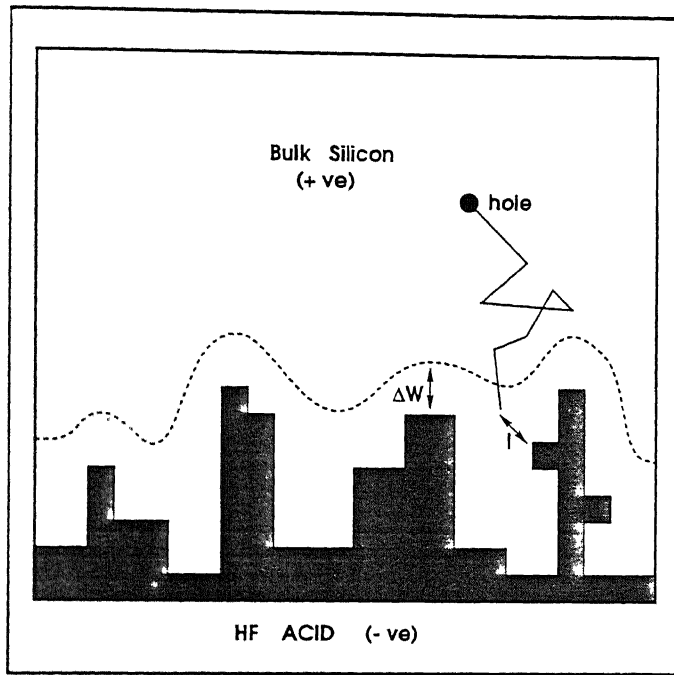


Figure 3.5: The diffusion induced nucleation model. Hole (filled circle) from the p-type substrate diffuses towards the HF electrolyte and etches a surface site. The broken line represents the depletion layer edge at a distance  $\Delta W$  from the interface. The hatched area represents the pores.  $l$  (dotted line) is the drift-diffusion length. The substrate is kept at a positive potential with respect to the HF electrolyte.

### 3.4 The Diffusion Induced Nucleation Model

The experimental conditions for porous silicon formation outlined earlier (Secs. 1.2 and 3.1) suggest that holes constitute the diffusion limited electro-active species [11]. A hole generated in the bulk undergoes diffusive motion until it comes within an interacting distance  $l$  of the surface. It is then field driven to the surface site and dissolution occurs. We designate  $l$  as the drift-diffusion length.

Dissolution of an atom can create upto three dangling bonds in the nearest neighbor atoms. These dangling bonds can act as secondary electro-active species, promoting further dissolution with a finite probability  $p_p$ . Thus the dissolution can either continue or terminate with a termination probability  $p_t$ .

$$p_t = 1 - 4p_p \quad (3.3)$$

The simulation is carried out on a two dimensional  $M \times N$  lattice with periodic boundary conditions (i.e., a wraparound configuration of modulo  $N$  in the lateral direction). Fig. 3.5 elucidates the geometry and the primary processes involved. Each unit of the lattice corresponds to one silicon atom with four nearest neighbors. The HF-Silicon interface is represented by a single side of the lattice which we term the 'surface'. Close to the surface there is a depletion region where no free carriers are present. The algorithm used to simulate etching in p-type silicon is outlined as follows.

### Diffusion

(i) Holes are generated in the lattice sites beyond the depletion region of width  $\Delta W$ , with uniform probability.

(ii) If a surface site is present within the drift-diffusion distance  $l$  of the hole, the hole moves to that site, causing dissolution.

(iii) If no surface sites are located within a radius  $l$ , the hole moves to one of the nearest neighbor sites at random. This random walk is repeated till it moves to a site within a radius  $l$  of the surface. It then proceeds to dissolve the detected surface site.

(iv) If the hole wanders beyond a distance  $3\Delta W$  from the interface, that hole is aborted and a new one generated.

### Pore Propagation

(v) Following the dissolution of a site, one of its nearest neighbors is chosen with a probability  $p_p$  and removed. This process is repeated till termination occurs with probability  $p_t$  where  $p_p$  and  $p_t$  are related by Eq. (3.3).

### Quantum Effects

(vi) Due quantum confinement effects, holes have a smaller probability of being generated in the porous silicon structure. We take this into account by employing a Boltzmann probability within a Metropolis like algorithm.

For n-type silicon the algorithm stands modified as follows:

As mentioned earlier, it is observed that pores are formed in n-type silicon only under illumination. Therefore, we assume that optical generation of holes is the major controlling mechanism in this case.

According to the Fermi thin slab approximation, intensity attenuation in silicon is given by

$$I(z) = I_0 \exp(-\mu z) \quad (3.4)$$

where  $I_0$  is the incident intensity and  $\mu$  is the attenuation factor associated with silicon. The number of carriers generated within a region is assumed to be proportional to the optical intensity in that region.

An optically generated carrier can recombine in several ways. The diffusion of these carriers is therefore limited by the carrier lifetime  $\tau$ . To take this into account, the hole is allowed to walk only for a proportionately smaller number of steps.

As the surface region gets etched, confinement effects increase the band gap causing these regions to become transparent to higher frequencies of illumination [111]. As a result, the carrier generation zone continually moves inwards. Taking into account these factors, the 'diffusion' part of the algorithm is modified as follows.

- (i) Holes are generated beyond the depletion region in the lattice, with an exponentially decaying probability from the surface in accordance with Eq. (3.4).
- (ii) If no surface sites are found by the hole after a short number of steps ( $\approx 5$ ), it is aborted.

The rest of the algorithm proceeds exactly as described for p-type silicon.

We also define a time scale for the simulation as follows: (i) each hole movement corresponds to one unit of time and (ii) each pore propagation chain also constitutes one time unit. This scale is used in later sections to make meaningful comparisons with experiment.

### 3.5 Morphologies in Diffusion Induced Nucleation

The diffusion induced nucleation model described in the previous section has been employed successfully to simulate structures similar to those resulting from the anodization of p-type and n-type silicon. A large number of runs were made<sup>1</sup> with

---

<sup>1</sup>The runs were carried out on a HP 900 workstation. The random number generator employed had a periodicity of  $2^{32}$ .

varying parameters. The resulting pore geometries exhibited a strong dependence on the parameters  $\Delta W$  and  $l$ . Typical results obtained are reported in this section.

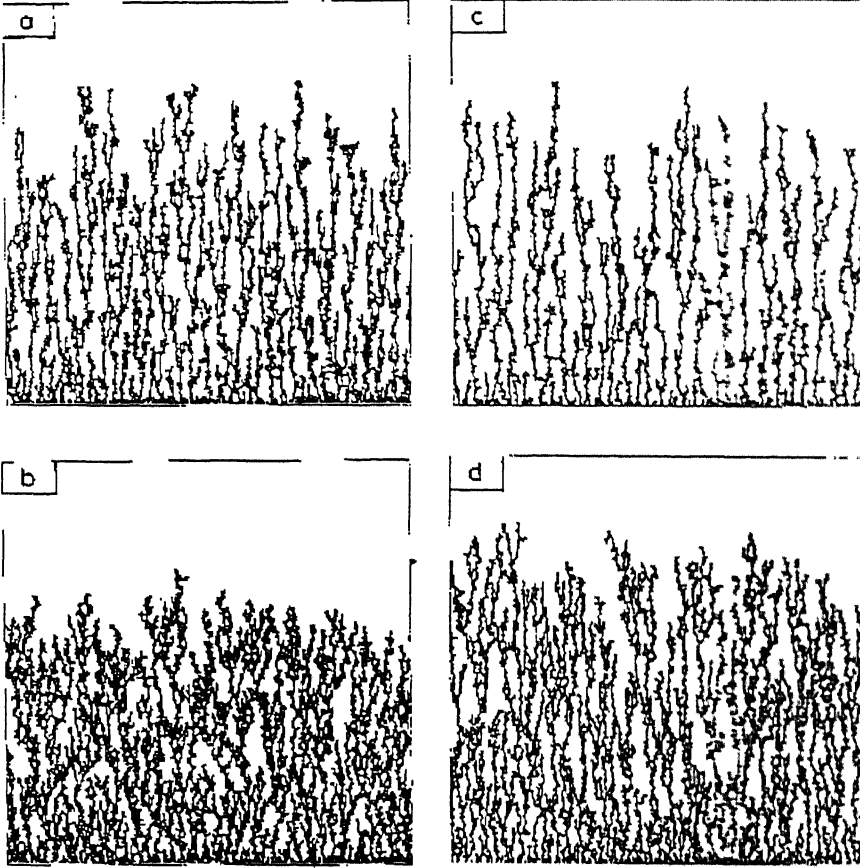


Figure 3.6: Typical morphologies obtained in the diffusion induced nucleation simulations on  $300 \times 300$  lattices. (a) Structure similar to the porous film formed on a p-type substrate, obtained using  $\Delta W = 6$ ,  $l = 11$ . (b) shorter and wider pores, similar to those formed on  $p^+$  substrate obtained using  $\Delta W = 3$  and  $l = 4$ . (c) Simulation done for an n-type substrate. ( $\Delta W = 8$ ,  $l = 9$ ). Note the relatively linear pore formation, compared to (a). (d)  $n^+$  substrate, simulated using  $\Delta W = 3$  and  $l = 4$ . The pore propagation probability is 0.15 in all cases. Note that (b) and (d) have almost identical structures. These morphologies are similar to TEM visualizations of porous silicon [11,12].

Using the algorithm for p-type silicon, the simulations were carried out on a  $300 \times 300$  square lattice. With  $\Delta W = 6$ ,  $l = 11$  and  $p_p = 0.15$ , the structure shown in

Fig. 3.6a was obtained. This has a spongy nature with long and highly interconnected pores and resembles the TEM visualizations of porous silicon fabricated from p-type substrates [11,12].

To model the increase in doping concentration, one has to account for both the decrease in the depletion layer width and the shorter interaction distance due to screening. A screened Coulomb potential can be written as

$$\phi(r) = \frac{q}{r} \exp(-k_s r)$$

where  $q$  is the carrier charge,  $r$  the distance from the carrier, and the inverse screening length  $k_s \propto n_0$ , the number of carriers present. The depletion layer width  $\Delta W$  decreases with increasing  $n_0$  both in the Beale type depletion and in the quantum confinement case. For a semiconductor depletion layer, this relation is given by Eq. (3.1). In the quantum confinement theory, the probability of finding a carrier in the enhanced band gap zone increases with carrier concentration. This can also be modeled as a decrease in  $\Delta W$ . To incorporate these dependences, smaller values were used for both  $\Delta W (= 3)$  and  $l (= 4)$  with all the other parameters being the same as that in Fig. 3.6a. The resulting structure, depicted in Fig. 3.6b has wider and shorter pores with numerous side branches and compares well with the results obtained for  $p^+$  material.

In order to carry out the same procedure on n-type silicon, the algorithm is modified as explained in the previous section. Fig. 3.6c represents a typical structure that was obtained using the algorithm for n-type silicon, with  $\Delta W = 8, l = 9$  and  $p_p = 0.15$ . Holes were generated in the lattice according to the distribution given by Eq. (3.4), with the attenuation constant  $\mu = 1$ . The pores are no longer random as seen in p-type, but exhibit a strong tendency to form straight channels [11]. At higher potentials, this leads to "piping" where we get straight, wide pores [11,99]. Our model can replicate this phenomenon if the depletion layer width is reduced (corresponding to a large applied potential) and the pore propagation probability is increased (a higher current would increase the etching probability). In all likelihood, the observed pipe formation has other processes contributing to an increased pore diameter, but it is heartening to note that the basic structure can be obtained through our simulation.

The pores in Fig. 3.6c are found to propagate in a linear fashion because of the following reason. Since the carrier lifetimes are very short, the chances of it tunneling

through to an interior site are very small. If the holes are unable to locate a tip site as soon as they are formed, they recombine and hence do not contribute to silicon dissolution. This virtually assures pore propagation in the tip direction, leading to straight channels. However, in the case of  $n^+$  material, the inter-pore spacing is smaller and the pores get interconnected. This is shown in Fig. 3.6d, which shows the result of a simulation carried out with  $\Delta W = 3$  and  $l = 4$ , all the other parameters remaining the same as in Fig. 3.6c. Note that Fig. 3.6b and Fig. 3.6d are almost identical, in conformity with TEM visualizations [11].

To sum up, our diffusion induced nucleation model successfully reproduces the morphologies of porous silicon films grown on both p-type and n-type silicon substrates.

### 3.6 Discussion

In Sec. 3.4, we have outlined the diffusion induced nucleation model used to simulate porous silicon formation on both p-type and n-type structures. Sec. 3.5 illustrates the differing morphologies obtained by varying the parameters and compares them with experimentally obtained structures. The values chosen for the parameters in each simulation were based on the experimental conditions. In this section, we attempt to place our efforts on a firmer footing by highlighting the agreement between the simulation and experimental growth literature. The results reported in this section are averaged over typically 10 simulations. Runs were made for lattice sizes ranging from 300 to 1000. Finite size effects were seen to be negligible.

We first investigate the rate of growth of the porous silicon film as a function of the controlling parameters. To monitor the growth of the film, we pause to define a root mean square height

$$h = \left[ \frac{1}{N} \sum_{i=1}^N h_i^2 \right]^{\frac{1}{2}}$$

where  $h_i$  is the pore height on the  $i^{th}$  row of the lattice.

Fig. 3.7 depicts the variation of the height  $h$  of the film as a function of the time  $t$ . Beyond a certain initial period, the plot is linear, which is indicative of a constant growth rate. This behavior is in conformity with several experimental observations

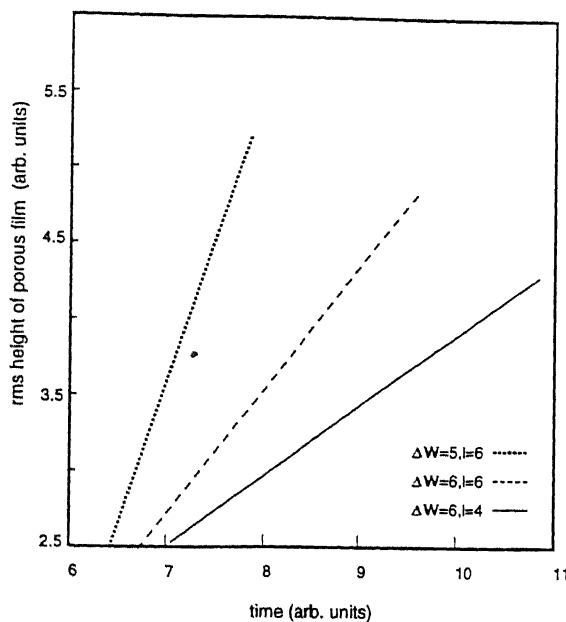


Figure 3.7: Plot of the film thickness  $h$  vs. time  $t$ . The plot is linear after beyond a small initial period. This figure is for a  $300 \times 300$  lattice with  $p_p = 0.15$ . Similar behavior was obtained for sizes upto 1000. Such linear rate growths have been reported by several workers [12,99,100].

which report film growth rates which are linear in time. Beale and coworkers [12] report that the film thickness is proportional to the anodization time. Searson [100] has found that this linearity is sustained over a large range of values for the film thickness (up to  $\sim 500\mu\text{m}$ ). These observations are confirmed by Lehmann and Foll [99], who report that the rate of growth is a function of parameters other than time.

Further, we note from Fig. 3.7 that the rate of growth ( $\dot{h}$ ) depends on the width of the depletion region ( $\Delta W$ ) and the interaction distance ( $l$ ) associated with the hole

$$\dot{h} = \dot{h}(\Delta W, l)$$

The growth rate is seen to increase with increasing values of  $l$ , as illustrated in Fig. 3.7 for  $l = 4$  and  $l = 6$ , all the other parameters being held constant. Also,  $\dot{h}$  increases with decreasing  $\Delta W$ , as portrayed by the two plots for  $\Delta W = 5$  and  $\Delta W = 6$ .

The dependence of  $\dot{h}$  on  $\Delta W$  is investigated in Fig. 3.8 which depicts a log-log



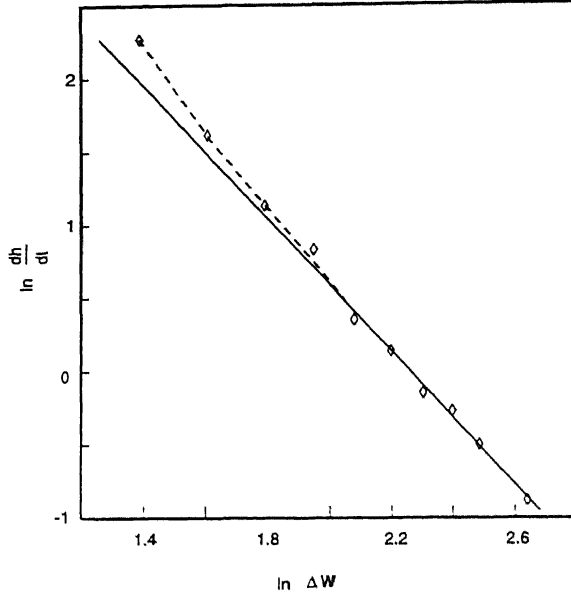


Figure 3.8: Log-log plot of the rate of growth  $\dot{h}$  ( $\frac{dh}{dt}$ ) of the film vs. the depletion layer width  $\Delta W$  ( $l = 5$ ). For large  $\Delta W$ , the graph follows the solid line with a slope  $\simeq -2$ , but exhibits a steeper slope for smaller values of  $\Delta W$  (broken line).  $p_p$  was kept constant at 0.15. A semi-quantitative discussion for this behavior is given in Sec. 3.6.

plot of  $\dot{h}$  vs.  $\Delta W$ . In the large  $\Delta W$  range,  $\dot{h}$  is seen to vary as

$$\dot{h} \propto \Delta W^{-2} \quad (3.5)$$

whereas for smaller values of  $\Delta W$ , the plot becomes steeper. This behavior maybe explained by invoking the dependence of the depletion region width on the applied potential across a semiconductor electrolyte junction.

$$\Delta W \propto (V_{BI} - V_a)^{\frac{1}{2}} \quad (3.6)$$

where  $\Delta W$  is the depletion layer width,  $V_{BI}$  is the contact potential across the junction and  $V_a$  is the applied potential. From Eq. (3.6) we obtain, for  $V_a \ll V_{BI}$

$$\frac{V_a}{V_{BI}} \simeq -2 \ln \Delta W \quad (3.7)$$

and for higher values of  $V_a$

$$\frac{V_a}{V_{BI}} \simeq -(2 + \epsilon) \ln \Delta W \quad \epsilon > 0 \quad (3.8)$$

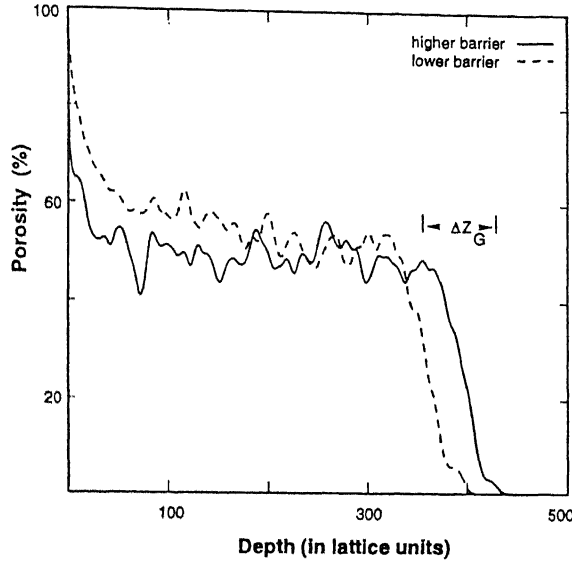


Figure 3.9: Porosity vs. depth plot for a typical simulation. The surface layer has high porosity (70-90%) and exhibits a fractal character [109]. This is followed by a constant porosity region ( $\simeq 60\%$ ). In the growth region  $\Delta Z_G$ , there is a sharp fall in the porosity. This simulation was done for a p-type substrate with  $l = 5$ ,  $\Delta W = 3$  and a  $300 \times 300$  lattice. The porosities are comparable to those of samples exhibiting visible photoluminescence. The broken line shows the porosity profile when a reduced barrier height is employed.

Searson [100] has shown  $\dot{h}$  to be linearly dependent on the current density. In the pore formation region, a typical silicon  $I - V_a$  characteristic [11] is exponential. Therefore,  $\dot{h}$  should vary as  $\Delta W^{-K}$ , where  $K$  is a constant. Thus we see that Fig. 3.8 is in good agreement with Eqs. (3.7) and (3.8).

In the context of the quantum confinement model, we expect  $\Delta W$  to decrease as the voltage is increased.  $\Delta W$  is inversely proportional to  $\exp[-(E_g - \Delta V)/kT]$ . The barrier height is effectively lowered because of the higher carrier energy. This will also lead to a similar monotonic dependence of  $\dot{h}$  on  $\Delta W$ .

This model yields much higher values for the porosity ( $\sim 80\%$ ) unlike the finite length diffusion model proposed by Smith and Collins [90], which typically reported porosities in the range 20-40%. In Fig. 3.9 we show a typical porosity vs. depth plot. The surface region has high porosity (70-90%). Porous silicon samples with porosities in this range are capable of causing photoluminescence in the visible range

[1,112]. Beyond the surface region, the porosity stabilizes around 60% and remains depth independent. It has been reported recently that further “passive” etching (i.e., HF can dissolve Si very slowly in the absence of any anodizing current) can result in depth inhomogeneities [113], but that regime is not of interest to the present work. The growth zone, denoted by  $\Delta Z_G$  in Fig. 3.9 shows a sharp fall in porosity. The dependence of porosity on quantum confinement is illustrated by the dotted line. We assume a smaller barrier height in our simulation, which results in a higher probability of hole occurrence in the porous silicon layer. This leads to higher porosity values as argued by Lehmann [108].

The high porosity surface region exhibits a fractal character, as has been reported earlier by other workers [109]. This region is probably mainly responsible for the high frequency component of the photoluminescence spectrum of porous silicon. Experiments have reported the suppression of the high energy part of the spectrum if the surface layers are made nonradiative [114]. It has also been shown that such inhomogeneities can lead to a ‘Lifshitz tailing’ of the photoluminescence spectrum [59] (See discussion in chapter 4).

It would be desirable to define a statistical measure which can differentiate between the morphologies depicted in Fig. 3.6 in a quantitative fashion. As seen in Fig. 3.9, the porosity is nearly depth independent beyond the initial high porosity region. Hence a mass-depth scaling exponent will have value  $\sim 1$ . This points to a possible non-fractal nature of the pore network. Hence the use of a conventional fractal dimension may not prove fruitful. We examine the degree of branching in terms of a dimensionless quantity  $\mathcal{B}$  which is defined to be the ratio of the distance between two adjacent nodes (branching points) on a pore to the mean thickness of the pore. Preliminary calculations yield approximate values of  $\mathcal{B}$  as follows: for Fig. 3.6a (p-type silicon)  $\mathcal{B} \approx 9$ , for Fig. 3.6b (p<sup>+</sup>)  $\mathcal{B} \approx 3$ , for Fig. 3.6c (n-type)  $\mathcal{B} \approx 17$  and for Fig. 3.6d (n<sup>+</sup>)  $\mathcal{B} \approx 5$ .

Unlike other models, our simulation can successfully reproduce the electropolishing regime in the anodization of porous silicon. At high anodic overpotentials, it has been observed that silicon uniformly etches away instead of forming porous structures. In our simulation, this corresponds to small values of  $\Delta W$ , which leads to structures with porosities greater than 90%. The simulation carried out using  $\Delta W = 2$ ,  $l = 5$  and  $p_p = 0.15$  exhibited a uniform removal of the surface. The etched

region in this case resembled the aggregates obtained using the ballistic deposition model [71].

Earlier models attributed electropolishing to the formation of an insulating oxide at the pore tips, which leads to preferential dissolution in the lateral directions. In the finite length diffusion model [90,115] the pore density is a function of the diffusion length  $\Delta W$ . Smaller values of  $\Delta W$  result in high porosity values. The limit  $\Delta W \rightarrow \infty$  mimics DLA algorithms, whereas the  $\Delta W \rightarrow 0$  limit yields the Eden [80] cluster. The compact Eden pattern may be invoked to explain electropolishing, though this is not the contention of Smith and coworkers. However, no convincing physical correlation has been established between varying the value of  $\Delta W$  and changing the experimental conditions. While this *may be* one of the processes that is taking place, we emphasize that in our model, electropolishing occurs as a *natural consequence* of decreasing  $\Delta W$ , without having to invoke any additional parameters. The dependence of porosity on  $l$  is illustrated in Fig. 3.4.

Besides the diffusion limited approach, percolation models have also been employed for simulating pore growth in silicon [116,117]. Given the nature of the Si-HF system where the acid eats into the crystal lattice, a percolation like approach seems appealing. However, such simulations have not been as successful as their diffusion limited counterparts in reproducing realistic morphologies. Further, no serious attempt was made in any of these simulations to establish a meaningful correspondence with experimentally relevant parameters. The present work (a) successfully reproduces porous silicon morphologies similar to those observed in TEM, including the well known ‘piping’ phenomenon in n-type silicon, (b) obtains structures of porosity 60-80% which in porous silicon are responsible for visible photoluminescence, (c) accounts for constant growth rates and its dependence on the anodizing potential, and (d) explains electropolishing in a natural fashion without taking recourse to additional processes or parameters. Further, the role of quantum confinement in determining the porosity is illustrated.

We have presented a simple, pragmatic diffusion induced nucleation model which explores the generic features in porous silicon formation. Our model successfully captures the essential physics of the dissolution process by employing mainly three parameters, namely the depletion layer width  $\Delta W$ , the drift-diffusion length  $l$  and the pore propagation probability  $p_p$ . It must be noted that the simulation is of a classical

nature. The quantum confinement effects are included by invoking a depletion region wherein hole generation occurs in a probabilistic fashion. These effects are seen to play a role in determining the lower limit of the crystallite size (Fig. 3.9). Further investigations need to be carried out on the model to work out better correspondences with the experimental conditions. For example, it may be worthwhile to look into the pore morphologies when inert masks are placed on parts of the silicon surface [97]. This will enable us to determine the feasibility of fabricating optical interconnects using porous silicon, a procedure which requires sharp edges. At a theoretical level, the fractal character of the surface layer may also be explored. Detailed experiments could be conducted to verify the dependence on the depletion region width, doping and temperature.

## Key Reference

The major reference for the material contained in this chapter is:

- George C. John and Vijay A. Singh, *Phys. Rev. B* **52**, 11125-11131 (1995).

# Chapter 4

## Shape of the Luminescence Spectrum in Porous Silicon

### 4.1 Introduction

Primarily, porous silicon is a disordered system. It consists of an intricate network of crystallites with varying sizes and shapes. The large surface supports hydrogen and oxygen complexes. At the microscopic level there exists dangling bonds and voids. Constructing a theory for the photoluminescence (PL) spectrum which encompasses all levels of disorder is a difficult task. Further, it may not be a desirable goal as it would entail the use of a large set of parameters whose numerical values are not accessible either by microscopic calculations or by experimental observations. Hence, a modest approach to explain the overall features of the PL spectrum, which operates within a circumscribed and limited set of plausible parameters is a desirable alternative [59].

The salient features of the PL spectra of porous silicon have been outlined in chapter 1. We briefly recapitulate them below (also see Fig. 4.1):

- The dominant red band in the PL spectra falls in the energy range  $1.2 - 2.3$  eV. This constitutes about 97% of the observed luminescence intensity.
- The PL spectra are broad, with FWHM around  $300 - 400$  meV.
- The spectral line shape is asymmetric on the energy scale, with a shoulder on the high energy side.

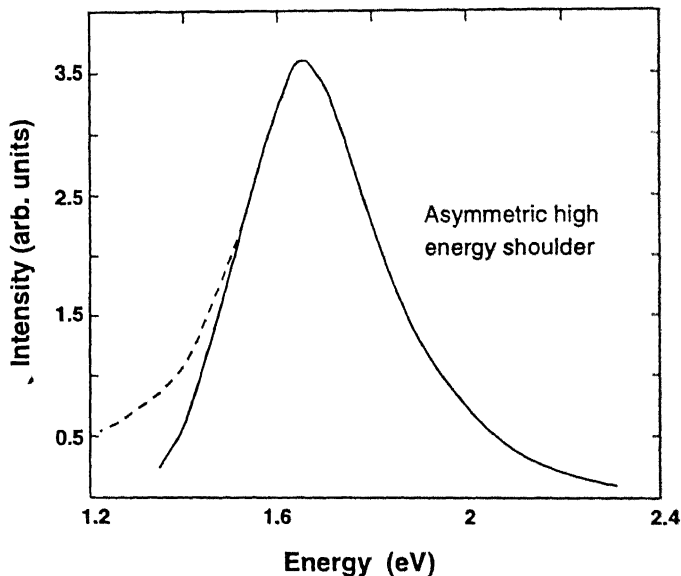


Figure 4.1: Salient features of the PL spectra in porous silicon. Note the asymmetry in shape, with a shoulder on the high energy side. The FWHM is approximately 300 meV. Some spectra show a low energy tail, which is represented by the broken line.

- A small number of experimentally reported spectra show a low energy tail, which extends into the infrared.

Our work is based on the quantum confinement model [1,19,103]. Most workers employ a simple quantum confinement model (Sec. 1.3.1) where the PL peak alone is sought to be explained. We believe that *disorder plays a key role* and model it by a distribution of crystallite sizes. This work, described in Sec. 4.2, is similar in spirit to the mean field approach of Kane and the probabilistic arguments of Lifshitz to explain the Urbach tail in optical absorption [118,119]. A large body of theoretical work in the Urbach tail problem assume that the absorption edge  $\alpha(E)$  is simply proportional to the electronic density of states and ignore the energy dependence of the transition matrix element and the electron-electron interaction [120]. There are several features which we choose to ignore in our formalism. Some of these are, relaxation of carriers, gap states due to voids and defects, thermal disorder and the distinction between hole and electron contributions to exciton energies. We wish to employ a small set of plausible parameters, and further, observe that these explain several reported PL spectra (Sec. 4.3). Our formalism can be extended to include the

above mentioned factors as well as important experimental parameters such as the frequency and intensity of the incident excitation. These are indicated later (Sec. 4.4).

In Sec. 4.2, we describe our theoretical formalism. We derive expressions for PL spectra originating from both column and dot distributions. The presence of local inhomogeneities where either columns or dots might dominate requires a Lifshitz like argument for modeling the edges of the PL spectrum. The PL spectra, which may appear Gaussian when plotted against the wavelength has a distinct asymmetry on the energy scale. This is naturally obtained in our formalism. A further noteworthy feature is a shift in the PL peak due to the distribution of crystallite sizes (Fig. 4.2). This enables us to employ a small and physically reasonable exciton binding energy.

In Sec. 4.3 we outline how the numerical values of the parameters employed are obtained from experimental observations and microscopic calculations. Our calculations compare favorably with the PL spectra obtained by several workers.

In Sec. 4.4, we briefly discuss earlier works based on the quantum confinement model. We outline extensions of our formalism to include some of the features which have been neglected in Sec. 4.2. We also indicate how some insight into related experimental observations such as photoluminescence excitation (PLE) can be attained based on our model.

## 4.2 Theoretical Framework

Our aim is to explain the photoluminescence (PL) spectra employing a minimal set of broad and plausible assumptions. There exists in literature a variety of approaches to the Urbach tail in optical absorption. We propose to work along the lines of two sister approaches : the one due to Kane and the well known Lifshitz argument [118,119]. We base our arguments on the quantum confinement model (see Sec. 1.3.1) but avoid the oversimplifying assumptions made by some of its proponents.

Columns of mean diameter  $d_0$  in the nanometer range have been reported by several independent groups [103,121,122]. The growth of these columns is a stochastic process as discussed in chapter 3 and it appears reasonable to assume columns of silicon with a Gaussian distribution of diameter  $d$  centered around a mean  $d_0$ , with



variance  $\sigma$ .

$$P_d = \frac{1}{\sqrt{2\pi}\sigma} \exp \left[ -\frac{(d - d_0)^2}{2\sigma^2} \right]$$

The number of electrons in a column of diameter  $d$  participating in the PL process is proportional to  $d^2$ . The heights of the columns depend only on the growth time and are approximately the same. Hence

$$N_e = N_e(d) = ad^2 \quad (4.1)$$

where  $a$  is a constant.

For a PS sample consisting of varying column diameters the probability distribution of electrons participating in the PL process is given by a product of the above two expressions:

$$P_{ed} = \frac{1}{\sqrt{2\pi}\sigma} bd^2 \exp \left[ -\frac{(d - d_0)^2}{2\sigma^2} \right] \quad (4.2)$$

where  $b$  is a suitable normalization constant.

In the quantum confinement model, the PL process is attributed to the energy upshift of the electrons and is proportional to  $1/d^2$ .

The PL energy  $\hbar\omega$  is given by

$$\hbar\omega = E_g - E_b + \frac{c}{d^2}$$

where  $E_g$  is the bulk silicon gap (1.17eV),  $E_b$  the exciton binding energy and  $c$ , an appropriately dimensioned constant. The energy upshift due to confinement  $\Delta E_u$  is

$$\Delta E_u = \hbar\omega - (E_g - E_b) = \frac{c}{d^2} \quad (4.3)$$

$$\Delta E_0 = \frac{c}{d_0^2} \quad (4.4)$$

where we have also paused to define a mean upshift  $\Delta E_0$  related to the mean column diameter  $d_0$ .

The PL line shape is then determined by transforming Eq. (4.2) to the energy axis as is commonly done.

$$P(\Delta E_u) = \frac{1}{\sqrt{2\pi}\sigma} b \int_0^\infty \delta \left( \Delta E_u - \frac{c}{d^2} \right) d^2 \exp \left[ -\frac{(d - d_0)^2}{2\sigma^2} \right] d(d)$$

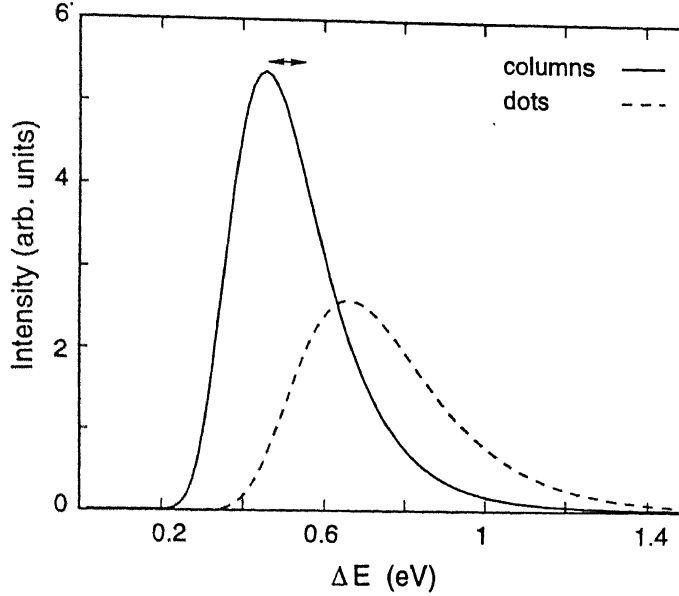


Figure 4.2: Theoretical PL spectra. The solid line is due to columns (peak at  $\Delta E_p = 0.46$  eV) and the dashed line is due to dots (peak at  $\Delta E_p = 0.67$  eV). The mean diameter is  $d_0 = 30$  Å and variance  $\sigma = 4$  Å for both spectra. The quantum confinement constant  $c$  (in  $c/d^2$ ) =  $485.816$  eV.Å<sup>2</sup> (the same as calculated by Read *et al.* [39]) and the binding energy  $E_b \simeq 0.14$  eV. The horizontal bar at the peak of the column spectrum indicates a downshift ( $\simeq 0.1$  eV) from  $\hbar\omega_0 = c/d_0^2$  on account of the statistical distribution of the column sizes. (See text in Sec. 4.2 for further discussion). Both spectra are normalized to unity.

The Dirac delta function facilitates a straight forward integration using the relation

$$\int_{-\infty}^{\infty} \delta(f(x))g(x)dx = \sum_{x_i} g(x_i) \left[ \frac{\partial f}{\partial x} \Big|_{x=x_i} \right]^{-1},$$

where  $x_i$  are the roots of  $f(x)$ . This yields,

$$P(\Delta E_u) = \frac{1}{\sqrt{2\pi}\sigma} \frac{b}{2\Delta E_u} \left( \frac{c}{\Delta E_u} \right)^{3/2} \exp \left[ -\frac{1}{2} \left( \frac{d_0}{\sigma} \right)^2 \left( \sqrt{\frac{\Delta E_0}{\Delta E_u}} - 1 \right)^2 \right] \quad (4.5)$$

The PL line shape is approximately Gaussian if  $\sigma$  is small. For finite  $\sigma$  the  $\sqrt{1/\Delta E_u}$  factor in the exponential outweighs the polynomial dependence in the pre-factor, resulting in an asymmetric curve with the shoulder on the high energy side (see Fig. 4.2).

Another aspect we need to note is that the mean energy of the upshift  $\Delta E_0$  (Eq. 4.4) and the location of the PL peak  $\Delta E_p (= \hbar\omega_p - (E_g - E_b))$  are not identical. To see this, we differentiate and set to zero the above expression (Eq. 4.5). This yields

$$\Delta E_p = \Delta E_0 \left[ \frac{1}{10} \left( \frac{d_0}{\sigma} \right) \left\{ - \left( \frac{d_0}{\sigma} \right) + \left( \left( \frac{d_0}{\sigma} \right)^2 + 20 \right)^{1/2} \right\} \right]^2 \quad (4.6)$$

For  $\sigma/d_0 \rightarrow 0$ ,  $\Delta E_p = \Delta E_0$  as expected. However, for reasonable  $\sigma$  the above expression can be Taylor expanded to yield

$$\Delta E_p = \Delta E_0 \left( 1 - 10 \left( \frac{\sigma}{d_0} \right)^2 \right)$$

From the values reported by Read *et al.* [39]:  $d_0 = 30 \text{ \AA}$ ,  $\sigma \simeq 3 \text{ \AA}$ ,  $\sigma/d_0 \simeq 0.1$ ,  $\Delta E_p = 0.9\Delta E_0$ .

Thus, there is a downshift. This is depicted by a horizontal bar in Fig. 4.2. It is important to realize the physical significance of this. As will be explained in the next section, the downshift dispenses with the need to invoke large and physically unreasonable exciton binding energies.

The peak in PL intensity is  $P(\Delta E_p)$ . We can obtain an approximate expression for the FWHM ( $\Delta E_{FWHM}$ ) of the PL spectrum. We can write the expression for the PL spectrum (Eq. (4.5)) as

$$P(\Delta E_u) = \frac{\mathcal{K}}{\Delta E_u^{5/2}} \exp \left[ -\frac{\Delta E_0}{2} \left( \frac{d_0}{\sigma} \right)^2 \left( \frac{1}{\sqrt{\Delta E_u}} - \frac{1}{\sqrt{\Delta E_0}} \right)^2 \right],$$

where  $\mathcal{K}$  is an appropriate normalization constant. If the pre-factor energy dependence  $\Delta E_u^{-5/2}$  is ignored, this expression represents a Gaussian distribution of the variable  $\xi = 1/\sqrt{\Delta E_u}$ , with a variance  $\bar{\sigma} = \sigma/(d_0\sqrt{\Delta E_0})$ . The FWHM on the  $\xi$  scale is then given by  $2\bar{\sigma}$ . Transforming this to the energy axis, we find,

$$\Delta E_{FWHM} = \Delta E_0 \left[ \left\{ 1 - \left( \frac{\sigma}{d_0} \right) \right\}^{-2} - \left\{ 1 + \left( \frac{\sigma}{d_0} \right) \right\}^{-2} \right]$$

For small  $(\sigma/d_0)$ ,

$$\Delta E_{FWHM} \simeq \frac{4\Delta E_0 \left( \frac{d_0}{\sigma} \right)}{\left( \frac{d_0}{\sigma} \right)^2 - 2} \quad (4.7)$$

A similar result can be obtained using a simple quantum confinement approach. Noting that  $\Delta E_u = c/d^2$  (Eq. (4.3)),

$$\begin{aligned}\Delta E_{FWHM} &= 2 \left| \delta(\Delta E_u) \right|_{d=d_0} \\ &= \frac{4c \delta d}{d_0^3} \\ &= \frac{4\Delta E_0 \sigma}{d_0}\end{aligned}\quad (4.8)$$

The above expressions are identical for large  $(d_0/\sigma)$ . Using  $c = 485.816 \text{ eV } \text{\AA}^2$ ,  $\delta d = \sigma = 3 \text{ \AA}$ , and  $d_0 = 30 \text{ \AA}$  (see the next section, Sec. 4.3 for a discussion of the numerical values), we obtain from Eq. (4.8),  $\Delta E_{FWHM} \simeq 200 \text{ meV}$ . A larger and experimentally reported  $\Delta E_{FWHM}$  is obtained if the exact expression Eq. (4.5) is employed.

Some workers have hypothesized the existence of dots instead of columns of silicon [58,123]. An analysis similar to the above can be carried out for dots. Employing  $N_c \propto d^3$  in Eq. (4.1) and carrying out the integration, the line shape for the dot is

$$P_{\text{dots}}(\Delta E_u) = \aleph \frac{1}{\Delta E_u^3} \exp \left[ -\frac{1}{2} \left( \frac{d_0}{\sigma} \right)^2 \left( \sqrt{\frac{\Delta E_0}{\Delta E_u}} - 1 \right)^2 \right] \quad (4.9)$$

where  $\aleph$  is a normalization constant.

#### 4.2.1 The Low Energy Tail in PL

It is conceivable that both columns and dots are present in porous silicon. The experimental PL spectrum is a weighted sum of the column and dot spectra. Statistically speaking, there would be inhomogeneities resulting in a region (say of volume  $V$ ) having an overwhelming column concentration  $c_c$  ( $\gg c_{c0}$ , the mean column concentration). The dot concentration in this region  $c_d$  ( $\ll c_{d0}$ , the mean dot concentration). One can then invoke a methodology along the lines of the Lifshitz argument [119].

One attempts to evaluate the probability of occurrence of  $n$  column crystallites in a volume  $V$ , which contains a total of  $N$  crystallites. This is given by

$$\begin{aligned}P(n) &= \frac{N!}{n!(N-n)!} c_{c0}^n c_{d0}^{(N-n)} \\ &= \exp[\ln N! - \ln n! - \ln(N-n)! + n \ln c_{c0} + (N-n) \ln c_{d0}]\end{aligned}$$

Making use of the Stirling approximation  $\ln N! \simeq N \ln N - N$ , we can write,

$$P(n) = \exp \left[ -N \left( c_c \ln \frac{c_c}{c_{c0}} + c_d \ln \frac{c_d}{c_{d0}} \right) \right]$$

Note that we have substituted  $n = Nc_c$  and  $(N - n) = Nc_d$ . Taking the limit  $c_d \rightarrow 0$ , we get

$$P(n) \simeq \exp \left[ -Nc_c \ln \frac{c_c}{c_{c0}} \right] \quad (4.10)$$

If  $\bar{v}_c$  is the mean volume of the column crystallite in this region, then

$$N \propto \frac{V}{\bar{v}_c} \quad (4.11)$$

$\bar{v}_c \propto d^2$  for a column crystallite, hence the confinement energy varies as (Eq. 4.3),

$$\Delta E_u \propto 1/\bar{v}_c \quad (4.12)$$

Using Eq. (4.11) and (4.12) in Eq. (4.10)

$$P(n) \simeq \exp [-K_1 \Delta E_u] \quad (4.13)$$

where  $K_1$  is a constant. The low energy part of the PL spectrum is modulated by this factor, and hence exhibits a tail. The presence of this tail accounts for some discrepancy between the theoretical PL spectrum based on Eq. (4.5) and the experimentally reported ones.

## 4.3 Results

We shall now present calculations based on our expressions in the previous section and compare them with experimentally reported photoluminescence spectra. Almost all reports on porous silicon report at least one PL spectrum. We have selected a representative set which highlights both the promises and problems associated with the natural theoretical framework outlined in the previous section. Variations in the proposed model and alternative explanations are outlined in the next section.

We note that the majority of the PL spectra reported have been recorded against the wavelength  $\lambda$  on the  $x$ -axis. In our comparison, we have faithfully transformed  $\lambda$  to the energy  $\hbar\omega$ . Note that  $\hbar\omega$  (in eV) =  $1.24/\lambda$  where  $\lambda$  is in  $\mu m$ . Recall that  $\hbar\omega = \Delta E_u - (E_g - E_b)$  from Eq. (4.3).

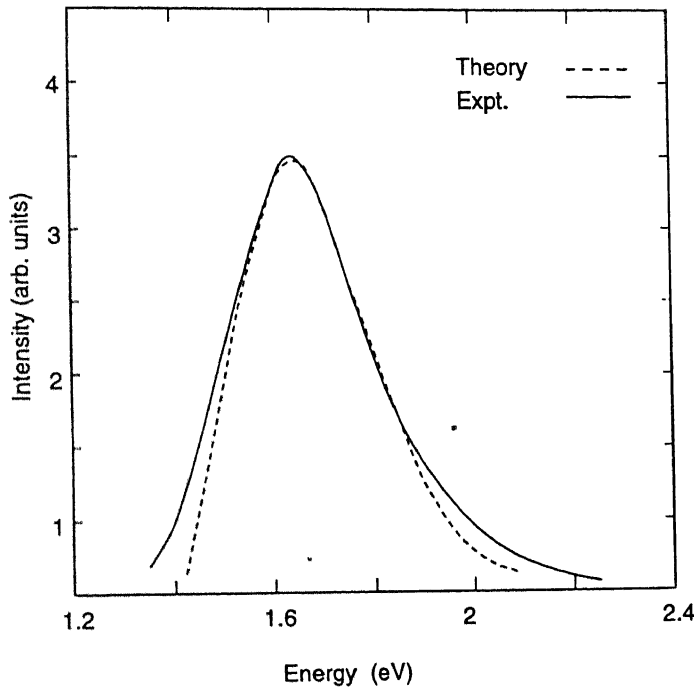


Figure 4.3: Comparison of experimental (broken line) and theoretical (solid line) PL spectra. The experimental curve, from Cullis and Canham [124] (their Fig. 1, sample 3), has also been discussed by Read and coworkers [39]. The theoretical spectrum is obtained using a mean diameter  $d_0 = 30 \text{ \AA}$  and variance  $\sigma = 4 \text{ \AA}$  for both dots and columns. The dot and column concentrations are 10% and 90% respectively.

The numerical values of physically important variables in our calculations are as follows: The band gap of silicon  $E_g$  ranges from 1.17 eV at 0 K to around 1.14 eV at 300 K. The existence of a distribution of column diameters results in a downshift from the mean peak (see the horizontal bar in Fig. 4.2). This allows us to use a smaller exciton binding energy ( $E_b \simeq 0.06 \text{ eV}$ ) which is physically more reasonable (than, for example, 0.16 eV proposed by Read and coworkers [39]). Thus  $E_g - E_b = 1.10 \text{ eV}$ . The constant  $c$  associated with the confinement energy ( $= c/d^2$ ) is taken from the calculations of Read *et al.* [39]. Its value is  $485.816 \text{ eV-\AA}^2$ .

Electron microscopy measurements suggest that the crystallite sizes are in the range  $20 - 40 \text{ \AA}$  [39,124]. The distribution can then be modeled as a Gaussian, with variance  $\sigma \simeq 10/3 \simeq 3 - 4 \text{ \AA}$ . Thus 99% of all columns or dots lie within  $3\sigma$ . We take  $d_0 \simeq 30 \text{ \AA}$ , a number reported by several workers [39,103,124]. The specific values of  $\{d_0, \sigma\}$  for a given spectrum are cited in the figure captions and these happen to lie

close to the above quoted values. In all our calculations we take the mean diameter ( $d_0$ ) of the column and/or dot to be the same. A priori, there is no reason for them to be different.

In Fig. 4.3 we compare the theoretical spectrum (solid line) with one experimentally obtained by Cullis and Canham (broken line) [124]. The experimental spectrum with a peak at  $\hbar\omega_p = 1.48$  eV, a full width at half maximum (FWHM) of 325 meV has also been theoretically studied by Read and coworkers [39]. The theoretical spectrum is obtained with mean diameter  $d_0 = 30$  Å and  $\sigma = 4$  Å. These values are the same as the ones suggested by Read *et al.* and so no “fitting” or “adjustment” on our part has been carried out. The agreement is excellent ( $\hbar\omega_p = 1.45$  eV, FWHM = 300 meV) except at the low energy end. The Lifshitz-like argument outlined at the end of the previous section provides a substantial improvement at the lower end with constant  $K_1 = 0.13$  eV<sup>-1</sup>. We do not wish to overemphasize its importance at this juncture except to indicate that it suggests inhomogeneities in porous silicon.

In Fig. 4.4 the experimental PL spectra of Vial and coworkers (broken line) is compared with our theoretical calculations (solid line) [58]. The experimental PL spectrum has a peak at  $\hbar\omega_p = 1.54$  eV with a FWHM = 270 meV. It was obtained for an oxidation rate of  $Q_0/4$  where  $Q_0$  is a threshold exchanged charge and is proportional to the layer thickness. The theoretical PL spectrum was obtained for a mean diameter of  $d_0 = 28$  Å whereas the experimental work quotes a theoretically calculated value of 30 Å. The variance  $\sigma = 4$  Å (same as for Fig. 4.3). Vial *et al.* propose a purely quantum dot model. We need to invoke dot and column concentrations of 15% and 85% respectively with both dots and columns having the same  $\{d_0, \sigma\}$  as mentioned above. Our calculations are in excellent agreement with the experimental curve.

In Fig. 4.5 an experimental PL spectrum (broken line), due to Zhang *et al.* is compared with our theoretical calculations (solid line) [125]. The theoretical spectrum is obtained on employing mean diameter  $d_0 = 28$  Å, variance  $\sigma = 3$  Å, assuming that only dots are present in the sample. The peak position is consequently much higher ( $\simeq 1.9$  eV) compared to the previous figures. The agreement with the experimental curve is good.

The above results have been demonstrated for representative experimental PL spectra. We have also performed a number of calculations for experimental spectra

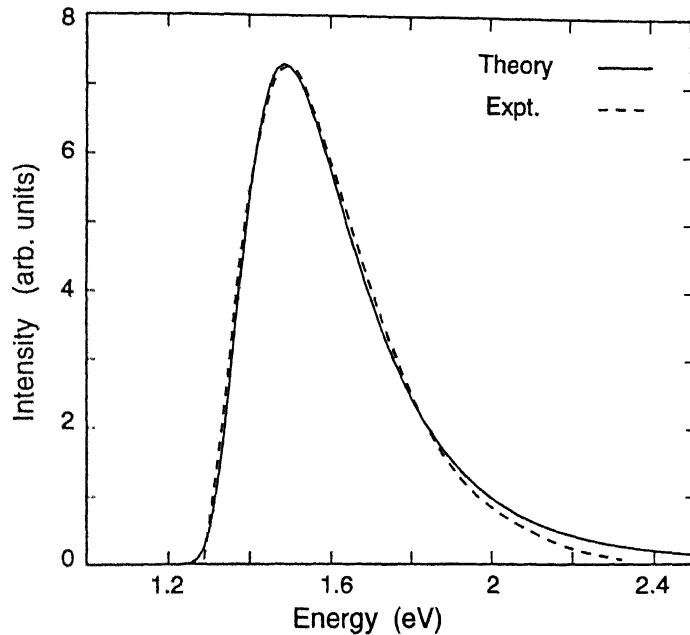


Figure 4.4: Comparison of experimental (broken line) and theoretical (solid line) PL spectra. The experimental curve, is due to Vial and coworkers (their Fig. 2, with oxidation level  $Q_0/4$ ) [58]. The theoretical curve was generated employing the presence of both dots (as conjectured by Vial and coworkers) and columns, each with mean diameter  $d_0 = 28 \text{ \AA}$  and variance  $\sigma = 4 \text{ \AA}$ . Dots and columns are present, the concentrations being 15% and 85% respectively.

reported by several other workers in the field. These include the ones by Banerjee *et al.* (their Fig. 2, curve c) [126], Hummel and Chang after spark erosion (their Fig.3) [127], Tsai *et al.* on Si:H passivation and immersion in HF (their Fig.1) [128], and Jung *et al.* (their Fig. 3) [129]. The numerical values of the parameters used have not been adjusted and are the same as those outlined in the beginning of this section. The agreement in all cases is good.

## 4.4 Discussion

The simplified assumption of free standing quantum wires due to Canham [1] cannot explain the broad photoluminescence (PL) spectra in porous silicon, which typically exhibits a FWHM of 300 - 400 meV. Though there has been suggestions in the literature that a distribution of crystallite sizes may be responsible for this [45],



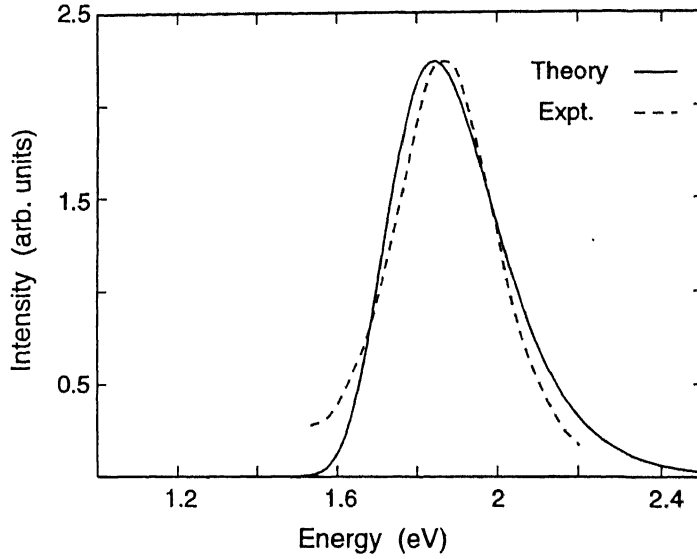


Figure 4.5: Comparison of experimental (broken line) and theoretical (solid line) PL spectra. The experimental curve is from Zhang *et al.* [125] (their Fig. 1, sample g). The theoretical curve (Eq. (4.5)) assumes a distribution of quantum dots alone with mean diameter  $d_0 = 28 \text{ \AA}$  and variance  $\sigma = 3 \text{ \AA}$ .

formal calculations have been attempted by only a few groups. In this section, we briefly review these attempts and examine our work critically in comparison with them.

In an earlier model, Fishman *et al.* [130] model the PL spectrum on lines similar to the work described in Sec. 4.2, but assume equal population of states in the crystallites. The energy upshift  $\Delta E_u$  is taken to be

$$\Delta E_u = \frac{K}{d^n}$$

where  $n=2$  if a simple infinite potential well is assumed, and  $K$  is a constant calculated from an effective mass approximation. They further account for a variation in the nonradiative rate with the photon energy  $E$ ,

$$R_n(E) \propto \exp(E/p_{NR}),$$

where  $p_{NR}$  is a constant ( $=0.29 \text{ eV}$ ). The PL spectrum is then given by

$$I(E) = \frac{P(E)}{R_n(E)}, \quad (4.14)$$

where

$$P(E)dE = P(d)d(d),$$

$P(d)$  being the crystallite size distribution, which is assumed to be Gaussian. They plot (4.14) for two different  $n$  ( $n = 1.64$  and  $n = 2$ ). The FWHM in both cases is seen to compare well with the experimentally obtained values. However, the low energy tail perceived in the PL spectra is not reproduced accurately by (4.14).

Xie and coworkers [31] account for the nonradiative recombination by modeling the probability that a given crystallite can luminesce according to Poisson statistics

$$P_r(d) = \exp \left[ - \left( \frac{d}{\bar{d}} \right)^3 \right], \quad (4.15)$$

where  $(\bar{d})^3$  is the mean volume occupied per dangling bond. Using this modulating factor along with a size distribution, the emission spectrum is calculated and is found to yield a PL efficiency of 0.5%, which is slightly lower than the generally observed external absolute quantum efficiency. The expression (4.15) may not be appropriate, since the number of non-radiative centers are more likely to depend on the surface area than the volume. In this case the exponent of  $d$  could lie between 2 and 3. In addition, if the oscillator strength dependence is included in this calculation, the PL efficiency can fall further.

Our work, described in Sec. 4.2, has attempted to obtain analytical expressions for the lineshape by assuming a Gaussian distribution of sizes and a simple quantum confinement model. The calculations have been performed for both columnar and spherical crystallites. One could also consider the case where  $\Delta E \propto d^{-n}$ ,  $1 \leq n \leq 2$ , as suggested by several workers [47,130] or consider polynomial dependences

$$\Delta E_u = \frac{c_1}{d} + \frac{c_2}{d^2}$$

as reported by others [46]. In the extreme case of a  $d^{-1}$  dependence, Eq. (4.5) is modified to

$$P(\Delta E_u) = \frac{\hat{N}}{\Delta E_u^5} \exp \left\{ -\frac{1}{2} \left( \frac{d_0}{\sigma} \right)^2 \left[ \left( \frac{\Delta E_0}{\Delta E_u} \right) - 1 \right]^2 \right\}$$

which has a comparatively narrower FWHM. ( $\hat{N}$  is a normalization constant).

The oscillator strength  $f_{vc}$  of the radiative transition may also vary with the crystallite size. Effective mass theory based approaches claim a size dependence of the form  $f_{vc} \propto d^{-6}$  for the oscillator strength [131,132], whereas some other workers claim a dependence of the form  $f_{vc} \propto d^{-5}$  [45]. LDA based calculations [42,46] ascribe a strong, but non-monotonic size dependence to the oscillator strength. We ignore the variation of oscillator strength with crystallite size in our formalism so that a minimal set of parameters can be employed. Despite this simplified approach, the success of Eq. (4.5) and (4.9) in modeling the observed PL spectra is heartening.

There are other attempts to model the effect of the size distribution on the PL spectrum. Behrensmeier and coworkers attempt to model the PL spectra as a superposition of distinct peaks due to discrete wire diameters [133]. Wang *et al.*, in a similar calculation, obtain pinning of peaks at certain discrete energies [49]. The growth process is however, stochastic, and wire diameters have a range as observed in transmission electron microscopy and scanning electron microscopy [39,103]. Hence our approach has, as its basis, a continuous distribution of sizes.

The irregular shape of the nanocrystallites are also seen to contribute to the gap enhancement. Electronic structure calculations employing a randomly porous cluster [52] report a disorder induced enhancement of the gap in addition to the upshift due to confinement. This can be understood as follows. In order to minimize the ground state kinetic energy, it is necessary for the wave function to have near zero amplitudes in the constricted regions such as “necks” or protrusions in an irregular structure. In a recent study [134] Sapoval, Russ and Chazalviel have shown that this can lead to localization of the wave function in the broader regions of the crystallite. Thus, the presence of disorder can reduce the ‘effective size’ of the crystallite as perceived by the carrier, and lead to a further enhancement in the energy gap. Thus, the disorder in shapes may also contribute to a broad PL spectrum.

One approach is to fit the PL spectra to a single or series of peaks with a Gaussian convolution. Employing this, Narasimhan and coworkers [61] have reported three peaks. A sum over exponentials representation is non-unique [135]. Further, the physical origin of these peaks needs to be elucidated for such an endeavor to be meaningful. In the absence of this, one merely has a curve fitting exercise. In contrast, our approach assumes a physical basis wherein not the spectra, but the underlying structure of crystallites has a Gaussian distribution.

In an earlier work, Murayama and coworkers [66] interpret the broad luminescence band by a model in which the electron hole pair created in the silicon nanostructure recombines radiatively through an excited luminescence center with strong phonon coupling. The excited lattice center has an energy minimum away from the ground state minimum, because of the lattice distortion induced by strong coupling with phonons. The visible transitions occur to the ground state according to the Franck-Condon principle. This can lead to an enlarged spectral broadening because of the vibration of the atoms around the luminescence center. It must be noted that lattice vibrations yield a typical broadening  $\sim kT$  ( $\leq 25$  meV) which is too small to explain such a large FWHM. An explanation of this kind would involve unphysical values of the Huang-Rhys factor and is improbable. Further, the majority of PL spectra observed in porous silicon show an inhomogeneous broadening as opposed to the Gaussian lineshape assumed by Murayama *et al.*

We observe that in seeking an agreement with the reported PL spectra, we need to invoke both columns and dots. Further, as mentioned in Sec. 4.2.1, a Lifshitz like argument could ensure that the tail states are properly accounted for. Thus, local inhomogeneities where columns pre-dominate over dots (or *vice versa*) exist.

There has been speculations about a possible fractal character for porous silicon [11]. Lehmann [136] points out that the experimentally observed size distributions of crystallites cannot account for a fractal character. It must be emphasized that the mere fact that the structure is porous and random does not imply a fractal geometry. The porosity is reported to be almost depth independent beyond the nanoporous layer [101]. This has also been supported by our simulation studies discussed in chapter 3. This results in a mass-depth scaling exponent of one, which implies a non-fractal character. Any possible fractal geometry will be present only in the top nanoporous layer. Fishman, Mihailescu and Romestain [130] in their work on PL broadening assume a fractal character and a resultant crystallite size distribution of the form  $d^{-d_f}$  where  $d$  is the crystallite diameter and  $d_f$  the fractal dimension. The computed PL lineshapes show an unphysically large FWHM. Because of this they rule out a fractal nature.

Our model can be extended further to incorporate several phenomena associated with the luminescence process, but at the cost of analytical transparency. Recombination to defect states is a distinct possibility. Defect states, primarily those due

to dangling bonds and voids, lie in the band gap (see Sec.1.3.3). These states may also be broadened due to the existing disorder in PS. Relaxation processes where the excited electron decays to an appropriate energy state and subsequently recombines is perhaps also present. The distribution of sizes in PS would exercise its influence over physical phenomena other than the PL spectrum. Murayama and coworkers [66] have reported an exponential Urbach tail in the PLE spectrum and this may be attributed to the above mentioned distribution and inhomogeneities. The effect of the surface contribution to the PL may be accounted for in our model by modifying the pre-factor in the distribution in Eq. (4.2) from  $bd^2$  to  $(b_1d^2 - b_2d^\alpha)$  where  $b_1$  and  $b_2$  are volume and surface dependent constants respectively. If the surface has a fractal character, the exponent  $\alpha$  may be different from unity. Further, Eq. (4.3) for the PL energy may be modified to

$$\hbar\omega = E_g - E_b + \frac{c}{d^2} + \mathcal{E}(I, \omega_I, \dots)$$

Here,  $\mathcal{E}$  accounts for non-linear processes arising out of the influence of experimental parameters such as the intensity  $I$  and the frequency  $\omega_I$  of the incident radiation. These extensions which are not included in our work may be relevant in explaining the PLE spectrum and an associated exponential Urbach tail. We hope to extend our work to explain these and other experimental observations.

In conclusion, we emphasize that the attractive aspect of our model is the choice of a minimal set of parameters whose numerical values are dictated not by the exigencies of an individual PL spectrum, but by independent microscopic calculations and experiments.

## Key Reference

The major reference for the material contained in this chapter is:

- George C. John and Vijay A. Singh, Phys. Rev. B **50**, 5329-5334 (1994).

## Chapter 5

# Model for the Photoluminescence Behavior of Porous Silicon

### 5.1 Introduction

A great deal of attention has been devoted to an understanding of the microscopic mechanisms responsible for the visible PL from porous silicon [2]. A considerable amount of data has accumulated from investigations of the dependence of PL on the temperature, pressure, excitation energy, luminescence energy etc. The present work is an attempt to explain and systematize this large body of data.

The properties of porous silicon have been known to depend on a range of factors. [2,57]. Briefly, some of these are: preparation conditions, size distribution of the crystallites and the surface chemistry of the nanostructures. Nevertheless, there is near unanimity about the photoluminescence behavior of high porosity samples ( $\geq 60\%$  porosity). Further, a careful study of the literature reveals systematic trends in the optical properties under various conditions for the dominant red band ( $\hbar\omega \in [1.2 - 2.2]$  eV). These trends have been discussed earlier in sections 1.3 and 1.5. We recapitulate some of them below:

1. The PL intensity shows a maximum with temperature, the peak being in the range 50K - 150K
2. The luminescence decay time falls by an order of magnitude or more as the temperature is increased from  $\sim 10$ K to room temperature.

3. The PL intensity falls steeply with pressure.
4. The luminescence decay time decreases systematically with emission energy in the range 1.4 - 2.5 eV
5. The PL peak position exhibits an anomalous behavior (both blue and red shifts) with temperature.
6. The PL peak position exhibits an initial blue shift and a subsequent red shift with pressure, when the pressure transmitting medium is alcohol.
7. The electroluminescence from porous silicon is weak, the quantum efficiency being at least 3 orders of magnitude lower than that of PL.
8. Radiative efficiency of porous silicon is higher than that of GaAs, but the luminescence lifetime is in the micro to millisecond range unlike GaAs (nanosecond lifetime).

Studies on carrier transport in porous silicon have asserted that the current predominantly follows a surface mechanism [137–139]. The carriers localized on the surface can (i) recombine radiatively, (ii) recombine nonradiatively, or (iii) escape to another localized state from where they may recombine either radiatively or nonradiatively. Since the electroluminescence is found to be weak despite a strong surface current, one can assume that the majority of charge transfer occurs through either process (ii) or (iii).

The luminescence decay time is normally expressed in terms of the competing radiative decay dynamics and nonradiative decay dynamics [58]. In recent years, some workers [140] have hypothesized the existence of a hopping term which also plays a role in determining the luminescence decay time. The resultant luminescence lifetime  $\tau$  can be written as

$$\frac{1}{\tau} = R_r + R_n + R_{hop}$$

where  $R_r$  represents the radiative recombination rate,  $R_n$  the nonradiative recombination rate and  $R_{hop}$  the hopping escape rate. Earlier studies [141,142] of the radiative process posit a temperature dependence of the Arrhenius type

$$R_r = \nu_r \exp\left(\frac{-T_r}{T}\right)$$

where  $T_r$  is a characteristic activation temperature and  $\nu_r$  a characteristic frequency. Since the photoluminescence efficiency of porous silicon is high, we propose that the nonradiative recombination term  $R_n$  is small compared to the hopping term  $R_{hop}$ . Several workers [143,144] report that the conductivity of porous silicon exhibits a Berthelot type [145] temperature dependence. Therefore, we now hypothesize that the hopping term varies with temperature as

$$R_{hop} = \nu_B \exp\left(\frac{T}{T_B}\right)$$

where  $T_B$  is the characteristic Berthelot temperature associated with the escape process and  $\nu_B$  a characteristic frequency. The varied optical behavior can then be analyzed in terms of the competition between the radiative and the hopping process. This approach is similar to the recent suggestions of a competition between radiative and non-radiative processes [140,146-148].

Section 5.2 describes the proposed model. In section 5.2.1, we describe an expression for the time integrated PL intensity in terms of  $\{T_r, T_B\}$  and the reduced frequency  $\nu_0 = \nu_B/\nu_r$ . Following Hurd [149], we then relate this expression to the properties of the barrier namely its height, width and frequency of vibration. This is described in section 5.2.2. In this section, we also discuss and circumscribe the range of numerical values that the parameters  $\{\nu_r, \nu_B, T_r, T_B\}$  may assume for porous silicon. This *a priori* assignment of numerical values enables our model to possess a firm predictive status.

In section 5.3, we analyze the temperature and pressure dependence of the PL intensity. Section 5.3.1 explores the temperature dependence of the time integrated luminescence intensity based on our model. It is found that the PL intensity exhibits a maximum at  $T_m \sim 50 - 150\text{K}$ . In section 5.3.2, we investigate the temperature dependence of the luminescence decay time and show that it falls by an order of magnitude or more as the temperature is raised from 10K to 300K. In section 5.3.3, we demonstrate that the PL intensity falls exponentially with increasing pressure. In each of these investigations, we make a detailed comparison with experiments conducted independently by a number of workers across the world.

A number of microscopic mechanisms have been proposed to explain the photoluminescence in porous silicon. A popular microscopic model is the quantum confinement model which assumes an enhanced, direct band gap due to carrier confinement



in the nanocrystallites. In our scheme as outlined in sections 5.2 and 5.3, we do not commit ourselves to any specific microscopic model. In section 5.4, we interpret our scheme to include an energy upshift due to quantum confinement. This enables us to explore the dependence of lifetime on luminescence energy (section 5.4.1) and the dependence of the peak position on temperature (section 5.4.2) and pressure (section 5.4.3). In each case we again carry out wide ranging comparisons with experiment.

Section 5.5 constitutes the discussion. We examine the validity of the approximations made by our model and suggest further experimental verification. We demonstrate that our model is analytically transparent and can successfully explain a wide variety of experimental measurements on the dominant red band in nanocrystalline and porous silicon. A preliminary account of our work along these lines has been reported earlier [150].

## 5.2 The Model

### 5.2.1 The Photoluminescence Intensity

The intensity of the PL line is expressed as

$$I(t) = N(t)R_r$$

where  $R_r$  is the radiative recombination rate and  $N(t)$  is the population of the excited carriers at time  $t$ ,

$$N(t) = N_0 \exp \left[ - \left( \frac{t}{\tau} \right)^p \right] \quad (5.1)$$

Here  $\tau$  is the characteristic lifetime associated with the Kohlrausch (stretched exponential) decay. Porous silicon is a disordered system and the time dependence of the PL intensity has been reported to be of the Kohlrausch type with  $0 < p < 1$  [58,140,141,151]. Thus

$$I(t, \tau) = N_0 R_r \exp \left[ - \left( \frac{t}{\tau} \right)^p \right]$$

The time-integrated luminescence intensity is then given by

$$\begin{aligned} I(\tau) &= \int_0^\infty I(t, \tau) dt \\ &= \frac{N_0 \Gamma(\frac{1}{p}) R_r \tau}{p} \end{aligned}$$

Note that the above expression reduces to  $N_0 R_r \tau$  for the pure exponential case ( $p = 1$ ). Defining  $I_0 = N_0 \Gamma(\frac{1}{p})/p$  we have

$$I(\tau) = I_0 R_r \tau \quad (5.2)$$

The characteristic lifetime is determined by the radiative recombination rate ( $R_r$ ), the nonradiative recombination rate ( $R_n$ ) and the hopping escape rate ( $R_{hop}$ ). As mentioned in section 5.1,  $R_n$  is taken to be small compared to  $R_{hop}$ . We can then express the luminescence decay time as

$$\frac{1}{\tau} = R_r + R_{hop} \quad (5.3)$$

The radiative rate has a weak Arrhenius dependence [142]

$$R_r = \nu_r \exp \left[ - \left( \frac{T_r}{T} \right) \right] \quad (5.4)$$

Suemoto and coworkers obtain a value of 3.5 meV for the activation energy ( $kT_r$ ) based on the time dependence of PL [141]. They also obtain a value of  $5000 \text{ s}^{-1}$  for  $R_r$ . Porous silicon is a highly disordered sample dependent system. The singlet triplet splitting energy of the exciton is in the range 3-10 meV. We therefore assume that the activation energy is in the range 3-10 meV and this translates to the range 25-135 K for the characteristic temperature  $T_r$ . This is in consonance with the 3-17 meV range reported recently by Kanemitsu [142].

As mentioned in Sec. 5.1 we hypothesize that the escape rate has a Berthelot type behavior

$$R_{hop} = \nu_B \exp \left[ \frac{T}{T_B} \right] \quad (5.5)$$

Employing Eqs. (5.3-5.5) in Eq. (5.2) we obtain

$$I(T) = \frac{I_0}{1 + \nu_0 \exp \left[ \left( \frac{T}{T_B} + \frac{T_r}{T} \right) \right]} \quad (5.6)$$

where  $\nu_0 = \nu_B/\nu_r$  is the reduced frequency. The temperature dependence of the PL intensity is explicitly displayed in Eq. (5.6). This expression also embodies information on pressure, emission energy and related dependencies which we shall examine in the present work.

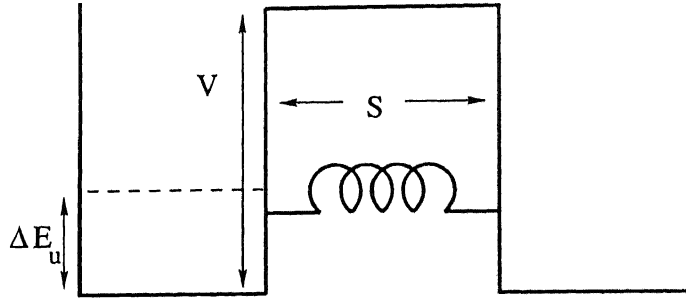


Figure 5.1: Possible model of tunneling through a vibrating barrier of width  $S$  and height  $V_0$ .

### 5.2.2 Dynamics of Carrier Hopping

The carriers can recombine radiatively or nonradiatively, or escape recombination via a hopping mechanism. Our hypothesis is that the hopping escape occurs as a result of tunneling across a vibrating barrier (see Fig. 5.1).

The transfer probability of thermally assisted tunneling has been obtained earlier by Tredgold [152] and Hurd [149]. We briefly recapitulate the salient features of their derivation. The tunneling probability  $\Gamma$  of a carrier of mass  $m$  across a stationary barrier of width  $S$  and height  $V$  and in the quantum state having energy  $\Delta E_u$  (see Fig. 5.1) is

$$\Gamma = \Gamma_0 \exp(-2\alpha S) \quad (5.7)$$

where  $\alpha^{-1}$  is the extent of the carrier wave function and is given by

$$\alpha^2 = \frac{2m(V - \Delta E_u)}{\hbar^2} \quad (5.8)$$

For a harmonically vibrating barrier the thermally averaged tunneling rate  $\langle \Gamma \rangle$  is determined by two competing scales, the thermal energy  $kT$  and the harmonic energy  $M\Omega^2/2\alpha^2$  where  $M$  is the mass of the vibrating ion and  $\Omega$  its frequency. Thus

$$\langle \Gamma \rangle = \Gamma_0 \exp(-2\alpha S) \exp \left[ \frac{2\alpha^2 kT}{M\Omega^2} \right] \quad (5.9)$$

Here,  $\Gamma_0$  is a characteristic tunneling rate. A more rigorous derivation by Hurd [149] yields

$$\langle \Gamma \rangle = \Gamma_0 \exp(-2\alpha S) \exp \left[ \frac{\hbar \alpha^2}{M\Omega \tanh(\frac{\hbar \Omega}{2kT})} \right] \quad (5.10)$$

Note that in the classical limit  $\hbar\Omega \ll kT$ , Eq. (5.10) reduces to Eq. (5.9)

We identify the escape rate  $R_{hop}$  with  $\langle\Gamma\rangle$ . Thus,

$$R_{hop} = \nu_B \exp\left(\frac{T}{T_B}\right) \quad (5.11)$$

with

$$\nu_B = \Gamma_0 \exp(-2\alpha S) \quad (5.12)$$

$$T_B = \frac{M\Omega^2}{2\alpha^2 k} \quad (5.13)$$

where  $\nu_B$  and  $T_B$  define the characteristic Berthelot frequency and temperature of the sample.

A number of assumptions are made in the above derivation. The Born-Oppenheimer approximation is employed. A single frequency  $\Omega$  is assumed for the vibration which implies that the escape process is probably linked to a defect related phenomena. The microscopic nature of the phenomena, whether it is vacancy or void or surface related, can be speculated on, but we shall at present refrain from doing so. Earlier studies of carrier tunneling across barriers exist [58,141,153]. These studies do not consider vibrations as we have done above.

Before we proceed further we examine the possible range of numerical values of the above-mentioned quantities. The mass  $M$  maybe associated with the silicon mass [149] and is  $4.7 \times 10^{-26}$  kg. The wave function extent  $\alpha^{-1}$  is taken to be 3-7 Å as argued by Deresmes and coworkers [144] in the context of electrical behavior of porous silicon. The earlier work of Hurd [149] in  $\text{SiO}_2$  assigns  $\alpha^{-1}$  the value of 3.4 Å. We assume  $\alpha$  to be in the range 0.2-0.8 Å<sup>-1</sup>. The frequency of the vibrating barrier  $\Omega$  is assumed [144,149] to be  $10^{11} - 10^{12}$  rad/s. These considerations yield the force constant  $M\Omega^2$  to be in the range  $3 \times 10^{-5}$  to  $3 \times 10^{-3}$  eV/Å<sup>2</sup> and hence the Berthelot temperature  $T_B$  ( $= M\Omega^2/2\alpha^2 k$ ) to be in the approximate range 10-200K. This is similar to the range suggested by conductivity experiments [143,144]. The latter is also the quantity most directly accessible from experiments. Later, we will modify these assignments based on comparisons with actual experiments. For example, the results of Sec. 5.3.1 suggest  $M\Omega^2$  to be in the higher range [ $3.5 \times 10^{-4} - 1.65 \times 10^{-2}$ ] eV/Å<sup>2</sup>.

## 5.3 Photoluminescence Intensity

### 5.3.1 Temperature Dependence

The explicit temperature dependence for the PL intensity is given in Eq. (5.6), namely,

$$I(T) = \frac{I_0}{1 + \nu_0 \exp \left[ \left( \frac{T}{T_B} + \frac{T_r}{T} \right) \right]}$$

The asymptotic limits of the above expression are

$$I(T)_{T \rightarrow 0} \rightarrow 0 \quad (\text{as } \exp[-T_r/T]) \quad (5.14)$$

$$I(T)_{T \rightarrow \infty} \rightarrow 0 \quad (\text{as } \exp[-T/T_B]) \quad (5.15)$$

It is clear from the above expressions that the PL intensity will have a maximum at some intermediate temperature  $T_m$ . This can easily be obtained to be the geometric mean of the characteristic temperatures

$$T_m = \sqrt{T_r T_B} \quad (5.16)$$

The possible range of the characteristic temperatures have been discussed earlier. Based on these *a priori* assignment of ranges the maxima for a PL emission line  $T_m \sim 100\text{K}$ .

A normalized PL spectrum based on equation (5.6) is depicted in Fig. 5.2. For the solid line we had assumed  $T_r = 75\text{ K}$  and  $T_B = 100\text{K}$ . The maximum temperature  $T_m = 87\text{K}$ . Notice that the intensity drops gradually for  $T > T_m$  and somewhat steeply for  $T < T_m$ . The latter behavior is on account of the strong exponential character at low temperatures ( $\sim \exp[-T_r/T]$ ). Also depicted in the figure is the experimental plot of Kanemitsu and coworkers for the PL intensity variation with temperature at 750 nm and for crystallite size of roughly 20 Å in diameter. The agreement is good.

The variation of PL intensity with temperature for crystallite of sizes 35 Å and 90 Å also shows a similar behavior, with maxima around 80K. Intensity maxima have been reported at lower  $T$  by other workers. For example, Banerjee has reported that the PL intensity for a PS sample at 810 nm shows a maximum at 31K [154]. The dashed line in Fig. 5.2 depicts the theoretical curve with  $T_r = 20\text{ K}$ ,  $T_B = 50\text{ K}$ . The agreement with Banerjee's result is encouraging. Banerjee also reported studies

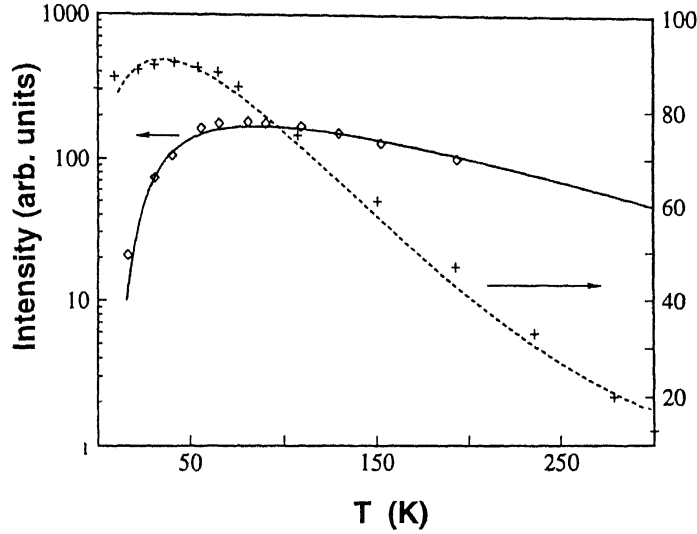


Figure 5.2: The variation of the luminescence intensity with temperature. The boxes denote data from Ref. [14] and crosses, data from Ref. [154]. The solid (dashed) line shows a theoretical plot based on Eq. (5.6) with  $\nu_r = 9000(6000)s^{-1}$ ,  $\nu_B = 5000(1000)s^{-1}$ ,  $T_r = 75(20)K$  and  $T_B = 100(50)K$ .

on emission lines of lower wavelengths which exhibited well defined maxima around 125K.

We note that similar temperature dependence of the PL line consistent with our model has been reported by a large number of workers. Xu, Gal and Gross [155] report that the PL from high porosity samples exhibited a maximum at 150-200K, whereas for low porosity samples, the PL intensity seemed to be constant below 80K. Mauckner and coworkers [156] also report a maxima at 150K for the 684 nm emission line from a p-type sample. Sucmoto, Tanaka, and Nakajima [141] report an intensity maximum for the 850 nm line around 80K. Their PL intensity falls slowly below 80K and by a factor of 40 from 80K to 300K. A similar behavior with  $T_m$  near 100K has also been reported for n-type samples [157]. We also note that there are reports of a monotonic increase in PL intensity [158] from 2K to 200K. In studies on partially oxidized porous silicon samples, Tsybeskov and coworkers [159] found a steady increase in the PL intensity for the orange band from 15 - 300 K indicating that  $T_m$  could be over 300 K in this case. Some other groups [31,160,161] have observed that the PL intensity remains nearly constant for low values of  $T$ , and decreases above  $T_m$ . This behavior is similar to that observed by Xu, Gal and Gross [155] for

their low porosity samples. We examine the expression for the intensity in the limit of low  $T$  to see that this behavior can be attributed to a low activation energy ( $kT_r$ ) associated with the radiative process.

$$I(T) |_{T \rightarrow 0} \sim \frac{I_0}{\nu_0} \exp\left(-\frac{T_r}{T}\right)$$

The  $T_m$  is thus low in these samples.

Some workers have chosen to plot the PL peak intensity with temperature [162] which yields a maximum at 210K and a sharp fall for  $T > 210$  K. Zheng, Wang and Chen [60] report maxima in the PL peak intensity between 100-200K for various p-type samples. A majority of the samples show a sharper dip in intensity below  $T_m$  than at  $T > T_m$ . The PL peak position is itself a function of temperature and we shall address this issue later in this chapter.

We also note that in most cases  $T_r < T_B$ . For  $T > T_B$  the expression for the PL intensity (Eq. (5.6)) reduces to

$$I(T) \xrightarrow{T > T_B} \frac{I_0}{1 + \nu_0 \exp\left[\frac{T_r}{T_B}\right]} \quad (5.17)$$

This type of behavior, e.g.

$$\frac{I_0}{I(T)} - 1 \propto \exp\left[\frac{T_r}{T_B}\right] \quad (5.18)$$

has been reported earlier in chalcogenide glasses, amorphous silicon [163], siloxene [164], and porous silicon [21,165]. From several fits to experimental data we also obtain a revised range of  $M\Omega^2$  to be  $3.5 \times 10^{-4} - 1.65 \times 10^{-2}$  eV/Å<sup>2</sup>.

### 5.3.2 The Luminescence Decay Time

The luminescence decay time is given by equations (5.3-5.5) to be

$$\begin{aligned} \tau &= \frac{1}{R_r + R_{hop}} \\ &= \frac{1}{\nu_r \exp\left(-\frac{T_r}{T}\right) + \nu_B \exp\left(\frac{T_r}{T_B}\right)} \end{aligned} \quad (5.19)$$

In the low temperature limit, the lifetime approaches a constant value,

$$\tau \rightarrow \frac{1}{\nu_B} \quad (T \rightarrow 0) \quad (5.20)$$

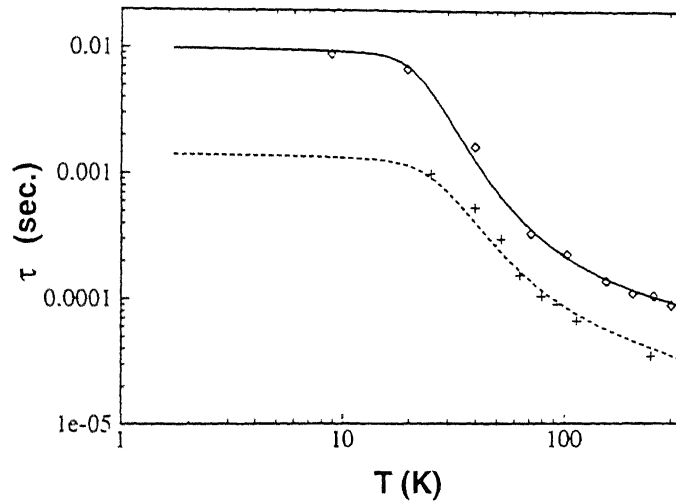


Figure 5.3: The temperature dependence of the luminescence decay time. Shown are the experimental values obtained from Ref. [156] (crosses) and Ref. [157] (boxes). The solid (dashed) line represents a theoretical fit based on Eq. (5.19) with  $\nu_r = 15000(35000)s^{-1}$ ,  $\nu_B = 100(700)s^{-1}$ ,  $T_r = 125(125)K$  and  $T_B = 150(150)K$ .

For the small but finite temperature limit where  $T \ll T_r$ , we can approximate Eq. (5.19) as

$$\begin{aligned}\tau &\simeq \frac{1}{\nu_B \exp(\frac{T}{T_B})} \\ &\simeq \frac{1}{\nu_B} \left[ 1 - \frac{T}{T_B} + \dots \right]\end{aligned}$$

The lifetime is thus seen to decrease as  $T$  is increased from  $T = 0$ . A theoretical curve based on Eq. (5.19) is plotted in Fig. 5.3. This depicts a  $\log(\tau)$  vs.  $\log(T)$  plot which compares well with the experimentally reported values (boxes) for the 700 nm line due to Finkbeiner and Weber [157](their figure 3). The lifetime  $\tau \sim 10^{-2}$  s at  $T = 10K$ . As the temperature is increased to  $\sim 200K$ , it falls by two orders of magnitude, and then levels off near room temperature. The low temperature value of the luminescence decay time (Eq. (5.20)) serves to fix the value of the hopping escape rate  $\nu_B \simeq 10^2 s^{-1}$ . The values of the other parameters employed in computing the theoretical curve are:  $\nu_r = 15000 s^{-1}$ ,  $T_r = 125K$  and  $T_B = 150K$ .

The detailed behavior of the plot in Fig. 5.3 can be understood from the expression



for the slope of the  $\log \tau$  vs.  $\log T$  curve

$$\frac{d(\log \tau)}{d(\log T)} = -\frac{T_r}{\left[1 + \nu_0 \exp\left(\frac{T_r}{T} + \frac{T}{T_B}\right)\right] T} - \frac{T}{\left[1 + \nu_0^{-1} \exp\left(\frac{T_r}{T} + \frac{T}{T_B}\right)\right] T_B} \quad (5.21)$$

where  $\nu_0 = \frac{\nu_B}{\nu_r} \sim 10^{-2} - 10^{-3}$ . In the intermediate range  $\frac{T_r}{T} \approx \frac{T}{T_B} \approx 1$ , therefore the second term on the right hand side of Eq. (5.21) is negligible. We can approximate the slope in this range to be

$$\frac{d(\log \tau)}{d(\log T)} \simeq -\frac{T_r}{\left[1 + \nu_0 \exp\left(\frac{T_r}{T} + \frac{T}{T_B}\right)\right] T}$$

Comparing the slope at  $T = T_r$

$$\left. \frac{d(\log \tau)}{d(\log T)} \right|_{T=T_r} \simeq -\frac{1}{\left[1 + \nu_0 \exp\left(1 + \frac{T_r}{T_B}\right)\right]}$$

and at  $T = T_B$

$$\left. \frac{d(\log \tau)}{d(\log T)} \right|_{T=T_B} \simeq -\frac{T_r}{\left[1 + \nu_0 \exp\left(\frac{T_r}{T_B} + 1\right)\right] T_B}$$

We find that the absolute value of the slope decreases as we increase the temperature. This is clearly discernible in Fig. 5.3, where we observe a flattening of the curve around  $T \sim 150\text{K}$ . Note that the slope always remains negative. At very large temperatures ( $T \gg T_B$ ), the second term of Eq. (5.21) is again dominant, i.e.,

$$\left. \frac{d(\log \tau)}{d(\log T)} \right|_{T \rightarrow \infty} \simeq \frac{-T}{T_B}$$

Thus the lifetime falls rapidly to zero for temperatures over 400K. This range is not of much experimental interest.

A similar dependence of the luminescence decay time on temperature has been reported by other workers. Pavesi and Ceschini [140] observe lifetimes to be independent of the excitation energy. Their measurements of the luminescence decay time vary over an order of magnitude of time from 10K to 300K. Mauckner and coworkers [156] measure the lifetime at 689.3 nm. Eq. (5.19) yields an excellent fit to their data. This is depicted in Fig. 5.3. They find  $\tau$  to vary from  $10^{-3}\text{s}$  at 25K to  $\sim 5 \times 10^{-5}\text{s}$  at 200K and seek to explain this as being caused by the excitonic exchange splitting proposed earlier by Calcott and coworkers [166]. Amato, Di Francia and Menna [160]

have carried out luminescence decay studies on samples of varying porosity. They observe a larger decrease ( $\sim$  two orders of magnitude) for 80% porosity samples as compared to 60-70% porosity samples ( $\sim$  1.5 orders of magnitude) in the temperature range 10 - 200 K. A similar decrease of one and a half orders of magnitude in the lifetime is reported by t'Hooft and coworkers [167]. Tsuboi, Laiho and Pavlov [168,169] postulate the observed red band luminescence decay time to be due to two states with lifetimes  $\tau_2$  and  $\tau_3$ , with  $\tau_2 \simeq 0.1\tau_3$ . In agreement with our results,  $\tau_3$  increases slowly with decreasing temperature from 300 K upto 100 K, and then increases rapidly. Our formalism can successfully reproduce these experimental results, working within a numerical range of parameters that has been *a priori* fixed.

### 5.3.3 Pressure Dependence

Our formalism enables us to gauge the pressure dependence of the PL intensity. We once again write down our expression for the PL intensity (Eq. (5.6))

$$I(T) = \frac{I_0}{1 + \nu_0 \exp \left\{ \frac{T_r}{T} + \frac{T}{T_B} \right\}}$$

we recall that

$$\begin{aligned} \nu_0 &= \frac{\nu_B}{\nu_r} \\ &= \frac{\Gamma_0}{\nu_r} \exp(-2\alpha S) \end{aligned} \quad (5.22)$$

where we have used Eq. 5.12. The application of pressure will modify the barrier width  $S$

$$S \rightarrow S(1 - KP) \quad (5.23)$$

where  $K$  is the isothermal compressibility. Hence from equations (5.6), (5.22) and (5.23), the pressure dependence of intensity can be explicitly stated.

$$I(P) = \frac{I_0}{1 + \left[ \frac{\Gamma_0}{\nu_r} \exp \left\{ \frac{T_r}{T} + \frac{T}{T_B} \right\} \exp \{ -2\alpha S(1 - KP) \} \right]} \quad (5.24)$$

It is clear that the intensity will drop with pressure. At room temperature, one can ignore the first term (unity) in the denominator of Eq. (5.24) and write

$$I(P) \simeq I_0 C(T) e^{-2\alpha KSP}$$

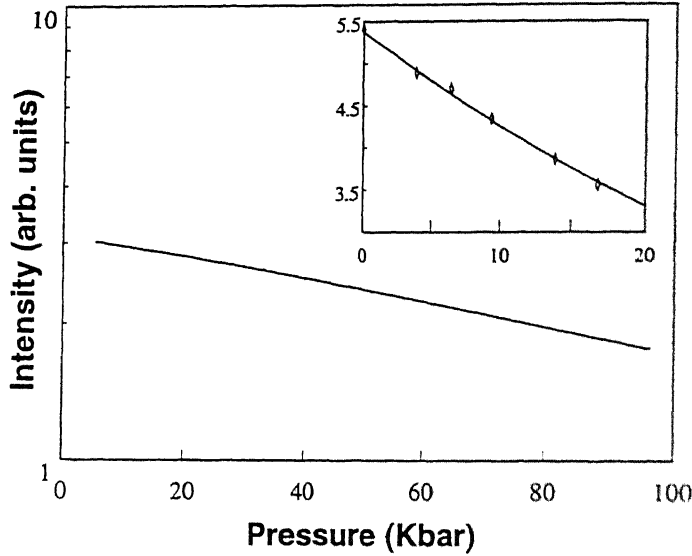


Figure 5.4: The variation of luminescence intensity with pressure, computed from Eq. (5.24) with  $\frac{\Gamma_0}{\nu_r} = 1000$ ,  $T_r = 75K$ ,  $T_B = 100K$ ,  $\alpha = 0.25\text{\AA}^{-1}$ ,  $S = 20\text{\AA}$  and  $K = 1\text{ Kbar}^{-1}$ . The inset shows a fit to the data reported by Zhou and coworkers (Ref. [170]).

where  $C(T)$  contains the temperature dependent factors. Thus we see that

$$\log I(P) \sim -P$$

The intensity falls exponentially with increasing pressure. In Fig. 5.4 we have plotted the pressure dependence of the intensity based on Eq. (5.24). Because of the uncertainties in the value of the compressibility for porous silicon (note that for silicon,  $K$  is  $1.012 \times 10^{-3} / \text{Kbar}$ ) and the arbitrary scale for intensity, a detailed quantitative comparison with experiments cannot be attempted. However, the trend predicted by our formalism is experimentally observed.

Zhou and coworkers [170] report that the PL intensity falls exponentially upto 20 Kbar for two different samples fabricated from p-type silicon. This is indicated in the inset of Fig. 5.4 This is in agreement with the experimental results of Ookubo, Matsuda and Kuroda [171] who note that the intensity is strongly reduced by the application of pressure and is almost quenched for pressures over 40 Kbar. This reduction is not entirely reversible. On restoring the pressure to its original value, the intensity returns only to a quarter of its initial magnitude. Interestingly, they note that the decrease in PL intensity due to increased pressure can originate partly from the increased non-radiative recombination due to an enhancement in tunneling.

Ryan, Wamsley and Bray [172] report a rapid quenching of luminescence upto 90 Kbar where the signal becomes very difficult to detect. In a recent work, however, Zeman and coworkers [173,174] have been able to observe PL upto 150 Kbar of pressure. These experimental results are in consonance with the predictions of our theory.

## 5.4 Model Dependent Results

Several microscopic models to explain the PL in porous silicon have been proposed (see Sec. 1.3). A popular model is the quantum confinement model which posits an enhanced direct gap on the basis of carrier confinement in silicon nanocrystallites. The results presented in sections 5.2 and 5.3 are not necessarily partial to any microscopic model. They can be derived solely in terms of the competition between an Arrhenius type radiative recombination term and a Berthelot type escape term. It would be interesting to explore our proposed scheme further in the light of the existing microscopic models. In this section we undertake this task in the light of the quantum confinement model.

In the quantum confinement model, the luminescence energy  $\hbar\omega$  is related to the bulk gap of silicon  $E_g$ , the confinement energy of the carrier  $\Delta E_u$ , and a subtractive term ( $-E_s$ ) coming from the exciton binding energy, the transverse optical phonon energy, etc. Thus

$$\hbar\omega = E_g + \Delta E_u - E_s \quad (5.25)$$

Recall from Fig. 5.1 that the escape rate is given in terms of the barrier height ( $V - \Delta E_u$ ). The carrier is in the level marked by  $\Delta E_u$  and we can ascribe to  $\Delta E_u$  the upshift due to the quantum confinement of the carrier in the nanocrystallite. From Sec. 5.2, the detailed form of the escape rate is (Eq. (5.5))

$$R_{hop} = \nu_B \exp\left(\frac{T}{T_B}\right) \quad (5.26)$$

$$= \Gamma_0 \exp(-2\alpha S) \exp\left[\frac{2\alpha^2 kT}{M\Omega^2}\right] \quad (5.27)$$

where from Eq. (5.8)

$$\alpha^2 = \frac{2m(V - \Delta E_u)}{\hbar^2}$$

Taking the logarithm and making only the energy related term explicit

$$\log(R_{hop}) = \gamma_0 - \gamma_1(V - \Delta E_u)^{1/2} + \gamma_2(V - \Delta E_u) \quad (5.28)$$

where  $\gamma_0 = \log \Gamma_0$ ,  $\gamma_1 = 2\sqrt{2m}S/\hbar$ , and  $\gamma_2 = \frac{2kT}{M\Omega^2} \left( \frac{2m^*}{\hbar^2} \right)$  and the constants  $\gamma$  are all positive. This establishes the framework within which we can examine the luminescence decay time dependence on emission energy, and the variation of the PL peak with temperature and pressure. Note that the subtractive term of Eq. (5.25) is small ( $\sim 0.1$  eV [59]) and serves as a correction term to the barrier height. Thus we take

$$V - \Delta E_u \rightarrow V + E_g - \hbar\omega \quad (5.29)$$

#### 5.4.1 Dependence of the Lifetime on Luminescence Energy

The dependence of the lifetime on the luminescence energy has been studied by several workers. In our formalism this dependence occurs explicitly in the non-radiative term and perhaps implicitly in the prefactor  $I_0$  term. We recall Eq. (5.19) for the lifetime

$$\tau = \frac{1}{R_r + R_{hop}}$$

The radiative recombination rate  $R_r$  is small compared to the hopping escape rate  $R_{hop}$  at  $T \simeq 300\text{K}$ . Hence

$$\log(\tau) = -\log(R_r + R_{hop}) \quad (5.30)$$

$$= -\log(R_{hop}) + \mathcal{O}\left(\frac{R_r}{R_{hop}}\right) \quad (5.31)$$

Substituting in the above equation, the expression for  $\log R_{hop}$  given in Eq. (5.28)

$$\log(\tau) = -[\gamma_0 - \gamma_1(V - \Delta E_u)^{1/2} + \gamma_2(V - \Delta E_u)] \quad (5.32)$$

where the dependence of the activated radiative term  $R_r$  on the confinement energy, if any, will be ignored for the present. The behavior of  $\log(\tau)$  on the confinement energy is depicted in Fig. 5.5. Recall that the hopping term is dependent on the confinement energy as indicated above. The plot in Fig. 5.5 is almost linear and the lifetime falls over an order of magnitude in the confinement energy range 0.2 to 1.0 eV (corresponding luminescence energy range is 1.4 to 2.2 eV). The parameters used are within the circumscribed ranges outlined in the previous sections. For comparison we

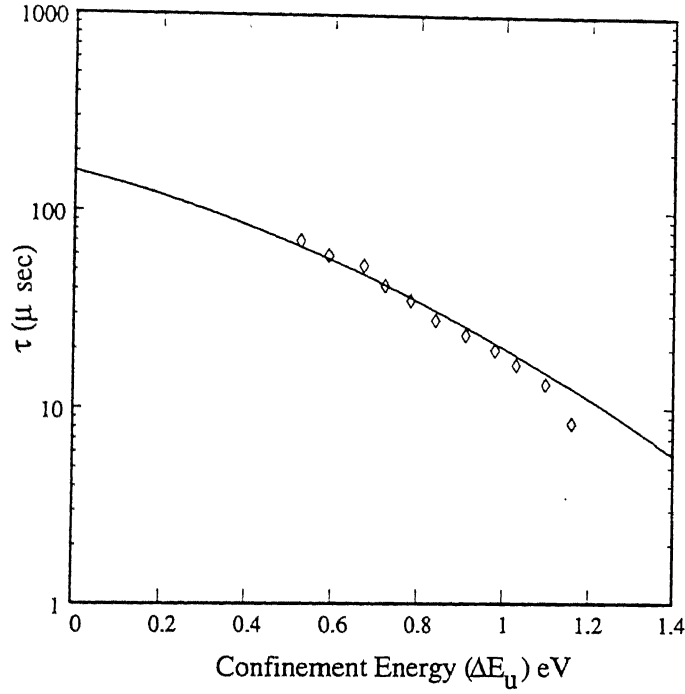


Figure 5.5: The variation of the luminescence decay time  $\tau$  with confinement energy  $\Delta E_u$ . The experimental data (boxes) is from Ref. [146]. The solid line depicts a theoretical plot based on Eq. (5.32) with  $R_r = 4000s^{-1}$ ,  $\Gamma_0 = 5 \times 10^8 s^{-1}$ ,  $\gamma_1 = 8(eV)^{-1/2}$ ,  $\gamma_2 = 0.4(eV)^{-1}$  and  $V = 2.5eV$ .

plot the experimentally reported lifetime data due to Pavese and coworkers [146] for a 87% porosity sample at room temperature. They extracted the lifetime from a fit of the time dependent PL intensity to a stretched exponential form as given in Eq. (5.1). The uncertainties inherent in extracting the lifetime inhibit a detailed quantitative comparison. Nevertheless the agreement between theory and experiment is excellent.

Past studies of the dependence of the lifetime on the energy reveal uncertainties in assigning a functional relationship. t'Hooft and coworkers [167] postulated a power law dependence  $\tau \sim \Delta E_u^{-3/2}$ . We have been able to replot their data along lines similar to Fig. 5.5. On the basis of effective mass theory, Hybertsen has proposed [132] that  $\tau \sim \Delta E_u^{-3}$ . He has also suggested that for phonon dominated processes,  $\tau \sim \Delta E_u^{-3/2}$ . On the other hand, several experimental groups have proposed that the inverse of the lifetime depends exponentially on the luminescence energy ( $\ln \tau = -\xi \hbar \omega$ ). This has been the observation of Vial and colleagues [58] who obtained  $\xi = 3.57 eV^{-1}$ , Ookubo, Hamada and Sawada [148] (their Fig. 2) and Kanemitsu [4] who

observed a linear variation of  $\ln(\tau^{-1})$  with the emission energy at high temperatures ( $\xi = 3.4 \text{ eV}^{-1}$ ). The data of Pavesi and coworkers depicted in Fig. (5.5) has also been modeled by a similar expression with  $\xi = 1.1 \text{ eV}^{-1}$  in a later work [175]. Since  $\hbar\omega \simeq E_g + \Delta E_u$ , the reports from these three distinct experimental groups are in conformity with the our model.

The influence of the confinement energy on the lifetime can be understood in a simple way. Since  $\Delta E_u < V$  we Taylor expand Eq. (5.32) to obtain

$$\log(\tau) = -[\gamma_0 - \gamma_1 V^{1/2} + \gamma_2 V] - \Delta E_u \left[ 1 - \frac{2\gamma_2 \sqrt{V}}{\gamma_1} \right] \frac{\gamma_1}{2\sqrt{V}} - \mathcal{O}(\Delta E_u^2) \quad (5.33)$$

From the numerical values quoted earlier  $\gamma_2 \ll \gamma_1$ , and the second term in square brackets on the r.h.s. is positive. Hence, using Eq. (5.29),

$$\log(\tau) \sim -\hbar\omega - \mathcal{O}(\Delta E_u^2)$$

This is the behavior observed in Fig. 5.5 and also in the experiments discussed above.

### 5.4.2 Temperature Dependence of the PL Peak

In Sec. 5.3.1 we described the temperature dependence of the PL intensity. Several workers have also mapped the temperature dependence of the peak PL emission energy  $\hbar\omega_p$ . There are reports of a blueshift with perhaps a subsequent redshift with temperature. Our model provides some insight into this anomalous behavior of the peak emission energy.

Recall our expression for the PL intensity in terms of the tunneling parameters  $\alpha$  and  $S$  (equations (5.4), (5.6), (5.12) and (5.13)),

$$I(T) = \frac{I_0}{1 + \frac{\Gamma_0}{\nu_r} \exp\left(\frac{T}{T_r}\right) \exp(-2\alpha S) \exp\left[\frac{2\alpha^2 kT}{M\Omega^2}\right]} \quad (5.34)$$

The emission energy is contained in the parameter  $\alpha$ . Recall that

$$\begin{aligned} \alpha^2 &= \frac{2m(V - \Delta E_u)}{\hbar^2} \\ &= \frac{2m(V + E_g - \hbar\omega_p)}{\hbar^2} \end{aligned}$$

where we have absorbed the small subtractive term due to exciton binding energy, phonons etc. into  $V$ . The peak energy is located by differentiating Eq. (5.34) with

respect to  $\alpha$ ,

$$\alpha_p = \frac{SM\Omega^2}{2kT} \quad (5.35)$$

$$\sim \frac{1}{T} \quad (5.36)$$

Combining the above expressions we obtain the PL peak emission energy

$$\hbar\omega_p = V + E_g - \frac{c_2}{T^2} \quad (5.37)$$

where  $c_2$  is a constant

$$c_2 = \frac{\hbar^2}{2m} \left( \frac{SM\Omega^2}{2k} \right)^2$$

The above expression for  $\hbar\omega_p$  implies a blue shift of the peak energy with temperature. It is known that the band gap of silicon decreases with temperature  $E_g = E_g^0 - c_1T$  where  $c_1 = 2.3 \times 10^{-4}$  eV/K. Using this as a guide and working within the quantum confinement model as noted earlier, we have

$$\begin{aligned} \hbar\omega_p &= V + E_g^0 - c_1T - \frac{c_2}{T^2} \\ &= c_0 - c_1T - \frac{c_2}{T^2} \end{aligned} \quad (5.38)$$

Clearly this expression implies an initial blue shift followed by a red shift. The crossover is determined by  $T = (2c_2/c_1)^{\frac{1}{3}}$ . Depending on the value of this cross over temperature, the PL peak may exhibit an initial blue shift or a red shift. In other words the anomalous dependence of the peak PL emission energy is possible.

This discussion must be viewed as a qualitative way of understanding the anomalous temperature dependence of the peak energy. The barrier frequency ( $\Omega \simeq 10^{11} - 10^{12}$  sec<sup>-1</sup>) occurs as the fourth power in the coefficient  $c_2$ . There is a large uncertainty in the parameter  $S$ . Besides, all parameters may be affected by post-anodization treatments. The temperature coefficient of the band gap in a silicon quantum wire may not necessarily be the same as of bulk silicon. Some uncertainty in the quantitative determination of the crossover temperature is thus inevitable. The crossover temperature may range between 20 to 1000K depending on the value of  $c_2$ . Eq. (5.38) may be taken as encapsulating the correct physical behavior. The term  $c_2/c_1$  can be obtained from experimental fit to data and can be used as a characterizing parameter.



An anomalous temperature dependence of the peak position, similar to that predicted by Eq. (5.38) has been reported in earlier experimental studies. Zheng, Wang and Chen [60] perform temperature dependent studies of the PL peak from four different samples of porous silicon, prepared with different current densities and anodization times. They observe an initial blue shift in the PL peak in three of their four samples as the temperature is increased from 20 K. One of the samples show a consistent red shift with increasing temperature. Xu, Gal and Gross [155] also observe both positive and negative shifts of the PL peak with temperature. Narasimhan and coworkers have reported an increase in the PL peak energy till 310 K. The PL spectra reported by Kesan and coworkers [158] also exhibit an anomalous behavior in the temperature dependence of the peak position. Shimuzu and coworkers have reported a steady blue shift for one sample and a steady red shift for two others samples [161]. Based on experiments carried out on silicon nanocrystallites Kanemitsu [142] reports that the PL peak energy is almost temperature independent and exhibits only a small red shift from 100K to 300K.

### 5.4.3 Pressure Dependence of the PL Peak

A number of studies of the pressure dependence of the peak PL emission energy  $\hbar\omega_p$  have been conducted. Some workers have found that  $\hbar\omega_p$  exhibits a small blueshift with applied pressure and then redshifts significantly [63,170,172,176]. Others have found only a red shift. These anomalous reports can be understood on the basis of our model.

In Sec. 5.4.2 we have obtained an expression for the peak energy (Eq. (5.38))

$$\hbar\omega_p = V + E_g - \frac{c_2}{T^2}$$

Note that  $c_2$  contains information on the barrier width  $S$  (e.g.  $c_2 \propto S^2$ ). The application of pressure will modify  $S$  as discussed in Sec. 5.3.3 (Eq. (5.23)). It will also modify the gap  $E_g$ . The indirect gap in crystalline silicon redshifts with pressure and with a pressure coefficient -1.41 to -1.5 meV/Kbar [177,178]. In amorphous silicon a larger redshift has been reported [179] with pressure coefficient  $-2 \pm 0.5$  meV/Kbar. Theoretical calculations by Yeh, Zhang, and Zunger [180] on silicon quantum wires also suggest a redshift but with a pressure coefficient smaller than in crystalline

silicon. Thus

$$E_g = E_g^0 - \eta P$$

where  $\eta$  may range from 0.1 to 2 meV/Kbar. The peak energy will then display a pressure dependence of

$$\begin{aligned} \hbar\omega_p &= (V + E_g^0 - \frac{c_2}{T^2}) + P \left( \frac{2Kc_2}{T^2} - \eta \right) - \frac{P^2 K^2 c_2}{T^2} \\ &= a_0 + a_1 P - a_2 P^2 \end{aligned} \quad (5.39)$$

Working within the numerical range of values chosen earlier, one can see that  $a_1$ , the co-efficient of the term linear in  $P$  can assume both positive and negative values. This in turn depends on the specific surface conditions. If  $a_1$  is positive, the r.h.s of Eq. (5.39) has a maximum and an initial blueshift can thus be explained.

Experimental studies of the pressure dependence of the PL peak are strongly dependent on the hydrostatic pressure transmitting medium employed. The experiments conducted in alcohol [63,170,172,176,181] show an initial blueshift upto pressures of  $\sim 20$  Kbar. beyond which there is a significant redshift. In another work employing a fluorocarbon medium. Ookubo, Matsuda and Kuroda [171] report redshifts above 20 Kbar. but are uncertain about the PL peak behavior at lower pressures. Sood, Jayaraman and Muthu [62] report a redshift at all pressures when the medium is paraffin oil. Their peak energy vs. pressure plot appears to be parabolic, which is again consistent with Eq. (5.39).

Cheong and coworkers [63] argue that due to these inconsistencies, pressure experiments could not be used as critical tests of the quantum confinement model. They conducted pressure studies using both alcohol and helium as the transmitting media. The PL peak shift in alcohol was consistent with the earlier results, where a blue shift was observed upto  $\sim 25$  Kbar. When helium was used instead of alcohol, only a red shift was seen. Based on this medium (and therefore, surface) dependence of photoluminescence, they asserted that the results are inconsistent with the standard quantum confinement model. In our framework, these results can be explained within a quantum confinement scheme.

## 5.5 Discussion

We have proposed a simple theoretical framework to understand and systematize the behavior of the dominant red band in the photoluminescence of porous silicon and silicon nanocrystallites. Our basic model as outlined in Sec. 5.2 and 5.3 uses a limited set parameters  $\{\nu_r, \nu_B, T_r, T_B\}$ , each of which can be ascertained in an independent, *a priori* fashion. These values can further be confirmed and refined by comparing our predictions with a variety of experiments. We do not take recourse to computer modeling or simulations. Our framework, which employs only analytical manipulations, is physically transparent.

The photoluminescence in porous silicon has been seen to be extremely sensitive to post-anodization surface treatments. This has led many workers to hypothesize a radiative recombination process involving intermediate surface states. Our model explains the surface dependence by hypothesizing an escape mechanism involving the surrounding environment. The parameters  $M, \Omega$  and  $V$  are surface dependent. The fact that the observed variations in photoluminescence with temperature and pressure can be reproduced by our model supports this assumption.

Porous silicon is a disordered system and its properties are dependent on sample preparation conditions and on surface chemistry. This is reflected in our model. We have assumed in Sec. 5.2.1 that the time dependence of the PL intensity is of the Kohlrausch type  $\exp[-(t/\tau)^p]$  with  $0 < p < 1$ . The parameters  $\{\nu_r, \nu_B, T_r, T_B\}$  assume a range of values reflecting the disordered nature of the sample. In Sec. 5.4.3 we have noted that the PL peak energy has an initial blue shift when the hydrostatic pressure transmitting medium is alcohol. If - as noted recently [63] - the medium is helium, the peak is uniformly redshifted. In our formalism this is accounted for by the sign of the linear coefficient of the peak (Eq. (5.39)).

A key hypothesis in our study is the presence of a Berthelot component in the PL intensity. As noted earlier, some previous studies on a-Si, siloxene, and porous silicon have reported an  $\exp[-T/T_0]$  dependence of the PL intensity  $I(T)$ . These studies do not ascribe this dependence to tunneling of carriers across a thermally vibrating barrier. We have shown in Sec. 5.3.1 that their expression for  $I(T)$  maybe viewed as a limiting case of our formalism. Some studies on the conductivity of porous silicon [137,144] do explicitly mention a Berthelot process. An issue of relevance

then, is the nature of the barrier. The phenomenological models for PL behavior by Vial *et al.* [58], Sacillotti *et al.* [182,183] and Qin and Jia [184] do describe non-radiative tunneling of carriers to a  $\text{SiO}_2$  coating surrounding the crystallite. In a recent work Schuppler *et al.* [57] have claimed that PL occurs in nanocrystallites of sizes  $\simeq 15\text{\AA}$ . Our barrier width  $S$  has a range  $5\text{-}20\text{\AA}$ . It is tempting then to think of the carriers in Fig. 5.1 to be hopping from the core to the surface of these luminescing nanocrystallites. At this stage we can only speculate on the nature of the barrier. Our results in Sec. 5.3.1 and Sec. 5.3.2 hold if we assume an Arrhenius and a competitive Berthelot term irrespective of the microscopic origin of the latter. We refrain from ascribing a definite microscopic material character to the barrier at this stage.

We have obtained the tunneling probability  $\langle\Gamma\rangle$  in terms of the barrier parameters. We had noted that a more rigorous derivation by Hurd [149] yielded

$$\langle\Gamma\rangle = \Gamma_0 \exp(-2\alpha S) \exp\left[\frac{\hbar\alpha^2}{M\Omega \tanh(\frac{\hbar\Omega}{2kT})}\right]$$

Even for a barrier frequencies as large as  $\Omega \simeq 10^{12} \text{ sec}^{-1}$ , as suggested by Hurd, the approximation  $\tanh(\hbar\Omega/2kT) \sim \hbar\Omega/2kT$  is excellent, upto temperatures as low as 10K. Hence, this approximation is valid in our case.

The barrier width  $S$  has been assumed to be temperature independent. The linear thermal expansion coefficient  $\beta$  for silicon has been reported to be  $1 - 5 \times 10^{-6} \text{ K}^{-1}$ . Thus the thermal expansion  $S\beta\Delta T$  of the barrier is less than 0.1% when a temperature variation of 100K is assumed. Hence the thermal expansion of the barrier can be safely ignored.

The radiative recombination has been assumed to follow an activated process  $R_r = \nu_r \exp(-T_r/T)$ . This is in agreement with the studies of Suemoto and coworkers [141] who experimentally obtain a fit to  $R_r$ ,

$$R_r = A \exp\left[\frac{-E_a}{kT}\right] + B$$

where  $A = 5000\text{s}^{-1}$  and  $B = 180\text{s}^{-1}$ . Since  $B \ll A$ , we have left out this temperature independent term, for the sake of mathematical simplicity. If  $B$  is included in the model, the low temperature limit of the luminescence decay time (Eq. (5.20)) will become

$$\tau|_{T \rightarrow 0} \frac{1}{\nu_B + B}$$

PL studies in amorphous silicon (a-Si) have been conducted for the past two decades [185–188]. Peak PL emission energies have been reported between 1.0 - 1.5 eV. The mechanisms contributing to PL have been debated ranging from donor-acceptor recombination to self-trapped excitonic models. Disorder plays an important role in these models. We have not undertaken a detailed survey of a-Si results yet. However, we point out two features of these studies. Street [187] has reported a maximum in the PL efficiency at 50K. He has attributed the fall in the PL efficiency below 50K to Auger recombination of geminate electron-hole pairs. There has been a recent suggestion by Delerue and coworkers [189] that the non-radiative process in silicon nanocrystallites is dominated by fast Auger recombination. Our work however does not explicitly invoke an Auger mechanism. Another feature of a-Si studies [185,186] is to ascribe the competitive non-radiative process to tunneling to defects. This is in consonance with our model.

Since porous silicon is a highly disordered system some studies have invoked Mott's variable range hopping model [4,190]. It has been customary to analyze the temperature dependence of the lifetime in terms of an activated or hopping process,

$$\frac{1}{\tau} \propto \exp \left[ - \left( \frac{T_0}{T} \right)^\alpha \right]$$

Here  $\alpha = 1$  is a pure Arrhenius dependence while a fractional value of  $\alpha$  indicates a Mott type variable range hopping process. Kanemitsu [4] has suggested a value of  $\alpha = 1/3$  corresponding to two-dimensional exciton hopping in the interface region of the silicon nanocrystallites. Our model attributes the temperature dependence of the lifetime to a mathematically well-defined competition between radiative and escape mechanisms where the latter is determined by tunneling across thermally vibrating barriers. An attempt by Mares [137] to fit the conductivity data to a Mott type process was unsuccessful in as much as it resulted in hopping distance of a thousand meters.

Based on our model we can suggest a range of experiments. The pressure dependence of the lifetime can be examined. Eq. (5.3) and Eqs. (5.10-5.12) yield

$$\frac{1}{\tau} = \Gamma_0 \exp[-2\alpha S] \exp[T/T_B] + R_r$$

From Eq. (5.23)  $S \rightarrow S(1-KP)$  with pressure  $P$ . This suggests that the lifetime falls

almost linearly with increasing pressure.

$$\log(\tau) \sim -(2\alpha KS)P$$

The conductivity of the sample has been observed to follow a Berthelot type law as noted above. The pressure dependence of the conductivity term can also be examined,

$$\sigma = \exp[-2\alpha S(1 - KP)]\sigma_1$$

where temperature and related dependencies are present in  $\sigma_1$ . Thus the conductivity should increase with pressure. The role of the pressure transmitting medium in governing the extent to which the lifetime and conductivity maybe significant as noted in the pressure studies in Sec. 5.4.3.

In summary, we have presented a transparent analytical framework to explain a diverse range of experimental studies on the PL behavior in porous silicon. This, we hope will provide a unified perspective to workers in the field. Systematic studies to verify, sharpen, and critique our model are possible. We hope to extend this framework to other aspects of porous silicon such as electroluminescence and to related nanocrystalline and disordered semiconductors.

## Key Reference

The major reference for the material contained in this chapter is:

- George C. John and Vijay A. Singh. Phys. Rev. **B 54**, 4416-4419 (1996).

almost linearly with increasing pressure.

$$\log(\tau) \sim -(2\alpha KS)P$$

The conductivity of the sample has been observed to follow a Berthelot type law as noted above. The pressure dependence of the conductivity term can also be examined.

$$\sigma = \exp[-2\alpha S(1 - KP)]\sigma_1$$

where temperature and related dependencies are present in  $\sigma_1$ . Thus the conductivity should increase with pressure. The role of the pressure transmitting medium in governing the extent to which the lifetime and conductivity may be significant as noted in the pressure studies in Sec. 5.4.3.

In summary, we have presented a transparent analytical framework to explain a diverse range of experimental studies on the PL behavior in porous silicon. This, we hope will provide a unified perspective to workers in the field. Systematic studies to verify, sharpen, and critique our model are possible. We hope to extend this framework to other aspects of porous silicon such as electroluminescence and to related nanocrystalline and disordered semiconductors.

## Key Reference

The major reference for the material contained in this chapter is:

- George C. John and Vijay A. Singh. Phys. Rev. B **54**, 4416-4419 (1996).

a proper characterization of the porous silicon surface. In this section, we discuss various efforts employing infrared vibrational spectroscopy to validate these models.

The formation process of porous silicon involves Si, HF and an organic medium such as  $C_2H_5OH$ . Consequently, the surface composition is largely unpredictable. Even the hydrogen passivated porous silicon surface is unstable and susceptible to contamination by other elements. Visible PL from porous silicon has been found to be extremely sensitive to surface treatments. This has prompted the school of thought which attributes the luminescence from porous silicon to the presence of luminescing chemical complexes on the large surface. Several molecules have been proposed as possible sources of PL.

The contention that certain siloxene derivatives constitute the source of the visible room temperature luminescence in porous silicon [193] was made largely on the basis of a comparison between the infrared transmission spectra of porous silicon and siloxene, which appeared to be remarkably similar. Further, as mentioned earlier in chapter 5, the temperature dependence of PL intensity in both the materials is well described by the relation

$$\frac{I_0}{I(T)} = 1 + \exp\left(\frac{T}{T_0}\right)$$

The large width of the PL spectra of porous silicon (see discussion in chapter 4) also supported the siloxene case, as all reported spectra fell well within the siloxene luminescence energy range.

Tischler and Collins showed that the infrared transmission spectra of freshly prepared porous silicon samples do not show any oxygen related modes [22]. At the same time, these samples also exhibit efficient visible luminescence. The pronounced lack of oxygen indicates the absence of siloxene or other oxygen containing complexes on the surface. On oxidation, porous silicon spectra was seen to develop oxygen related modes and become similar to the siloxene infrared spectrum. They concluded that the presence of siloxene is not necessary for obtaining efficient PL. Thus the refutation of the siloxene model was also premised on careful infrared studies.

In a later study [194], they observed that during UV illumination of the PS sample, hydrogen desorption occurs (as illustrated by a drop in intensity of the Si-H vibration band) along with photoluminescence degradation. It was also observed that thermal annealing causes degradation of PL due to hydrogen desorption. This led to the belief



that surface Si-H<sub>n</sub> molecules (silanes) were the luminescing agents in porous silicon. However, in another infrared study [195] carried out with various etching times of silicon in HF, it was seen that the intensity of the PL spectra bore no correlation with the Si-H vibration mode. The observed degradation of PL on hydrogen desorption could be attributed to an increase in the number of dangling bonds which can act as centers for non-radiative recombination.

To account for the sensitivity of PL to post-anodization surface treatments within a quantum confinement model, a hybrid model invoking the recombination of carriers confined in the nanocrystallites via the surface states has been suggested. It has been proposed that various chemical ligands such as H, OH, O and other radicals can saturate the Si cluster. This results in a wide spectrum of disorder induced trap states which act as mediators in the light emitting process. A convenient way to characterize these surface states is provided by infrared vibrational spectroscopy. This can yield information on the electron states as well as on the vibrational modes of the surface spectra.

The above discussion underscores the importance of impurity related studies in discriminating between the surface related models for PL in porous silicon. It would be useful to develop a phenomenological scheme for the assignment of the vibrational frequencies of impurities in porous silicon. In this chapter, we propose a simple model for the stretching mode vibrational frequencies of hydrogen and chlorine in varying environments found on the silicon crystallite surface. The model is calibrated by appealing to well established vibrational spectra assignments in crystalline silicon.

It has been known for sometime that the stretching mode vibrational frequencies of Si-H ( $\nu_{\text{Si-H}}$ ) in substituted silane molecules SiHR<sub>1</sub>R<sub>2</sub>R<sub>3</sub> [196], amorphous solids such as a-Si and a-SiO<sub>2</sub> [197], and in crystalline silicon (c-Si) [198] correlate with the electronegativities of {R<sub>1</sub>R<sub>2</sub>R<sub>3</sub>}. The R<sub>i</sub> here may denote an element or a radical. The following explanation is usually proffered for this correlation. As the electronegativity of the substituting species {R<sub>1</sub>R<sub>2</sub>R<sub>3</sub>} increases, the s-character of the Si-H bond increases. A calculation of the s-component of the bond-order matrix substantiates this [199]. Because of the enhanced s-character, the Si-H distance  $d_{\text{Si-H}}$  decreases and the effective force-constant increases. Thus  $\nu_{\text{Si-H}}$  increases. In this chapter, we develop a phenomenological approach to predicting the vibrational frequencies of the Si-H bonds depending on the immediate molecular environment. Section 6.2 outlines

this model. In section 6.3, we predict the frequencies of possible surface environments in porous silicon and critique the existing assignments in literature.

## 6.2 The Renormalized Electronegativity (REEL) Model

### 6.2.1 Electronegativity and Orbital Radius

To motivate the application of the orbital-radii scales to the systematization and prediction of the vibrational frequencies of H and other impurities in semiconductors, we shall first relate the electronegativity to the orbital radius of the element  $R_j$ . The three orbital radii listed by Zunger [200] are  $r_s$ ,  $r_p$ , and  $r_d$  which are respectively the crossing points of the first principles pseudopotentials for  $l = 0, 1$ , and  $2$ . The role of the  $s$  character of a  $\nu_{\text{Si-H}}$  bond in determining the Si-H vibrational frequencies has been pointed out by other workers [198,199]. Further,  $\nu_{\text{Si-H}}$  has been related to Sanderson electronegativity  $SR$  of element  $R_j$  [197]. This motivated us to seek a relation between the electronegativity and the Zunger orbital radii  $r_s(R_j)$  since the  $s$ -character of the Si-H bond appears to play a key role [199].

Pauling defined electronegativity as "the power of an atom in a molecule to attract electrons to itself" [201]. Several numerical scales have been devised for a quantitative representation of the electronegativity scale. Allred and Rochow chose to represent electronegativity by the electrostatic force exerted on the valence electron by the nucleus of the atom [202]. The Allred - Rochow electronegativity  $\chi_{AR}$  is expressible on the Pauling scale (i.e., with values close to the Pauling electronegativity  $\chi_P$  values in magnitude) as

$$\chi_{AR} = \frac{0.3592Z^2}{R_c^2} + 0.744 \quad (6.1)$$

where  $Z$  is the effective nuclear charge, and  $R_c$  is the single bond covalent radius.

Another similar approach is due to R.T.Sanderson who defines a stability ratio ( $SR$ ) [203,204]. This is the ratio of the average electron density ( $\bar{\rho}_e$ ) of the atom to that of an inert atom having the same number of electrons.

$$\bar{\rho}_e = \frac{3Z}{4\pi R_c^3}$$

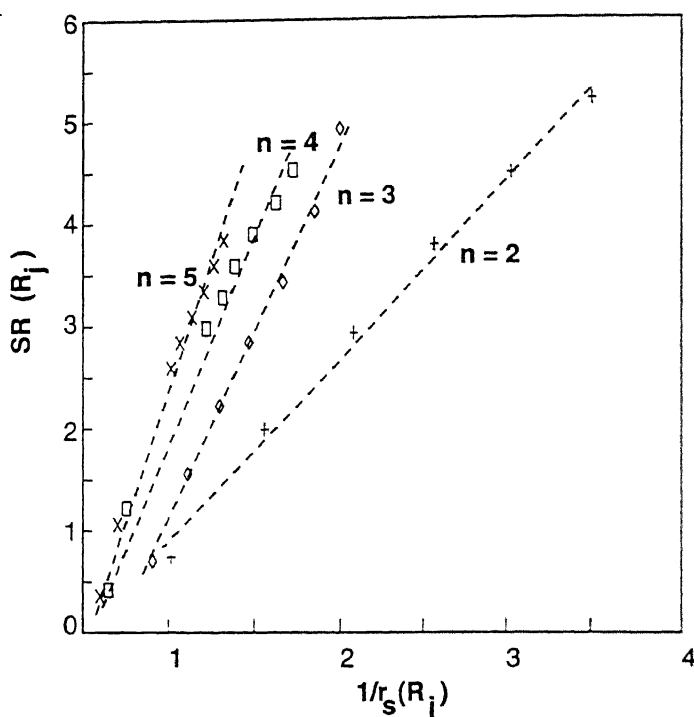


Figure 6.1: Row-wise plots of the Sanderson electronegativity  $SR(R_j)$  and  $1/r_s(R_j)$ , where  $r_s(R_j)$  is the  $l = 0$  orbital radius of the element. The principal quantum number of the valence shell is denoted by  $n$ .

whereas the electron density of the corresponding inert atom is calculated by interpolating the noble gas electron densities.  $SR$  is reported to scale linearly with  $\sqrt{\chi_P}$  [197],

$$\sqrt{\chi_P} = 0.21SR + 0.77 \quad (6.2)$$

We find a similar linear relationship, but with the slope 0.19 (instead of 0.21) and intercept 0.79 (instead of 0.77).

Eqs. (6.1) and (6.2) suggest a linear relation between  $1/r_s$  and  $SR$  of the form

$$SR(R_j) \propto \frac{1}{r_s(R_j)}$$

can be established for each row of the periodic table [205]. This is depicted in figure 6.1. But to establish a universal linear relationship incorporating several rows of the periodic table, we need to postulate another quantum scale.

According to Zunger [200] the orbital radii are characteristic of the atomic cores whose defining quantum numbers are  $1, 2, \dots, n-1$ . In this spirit we attempt to

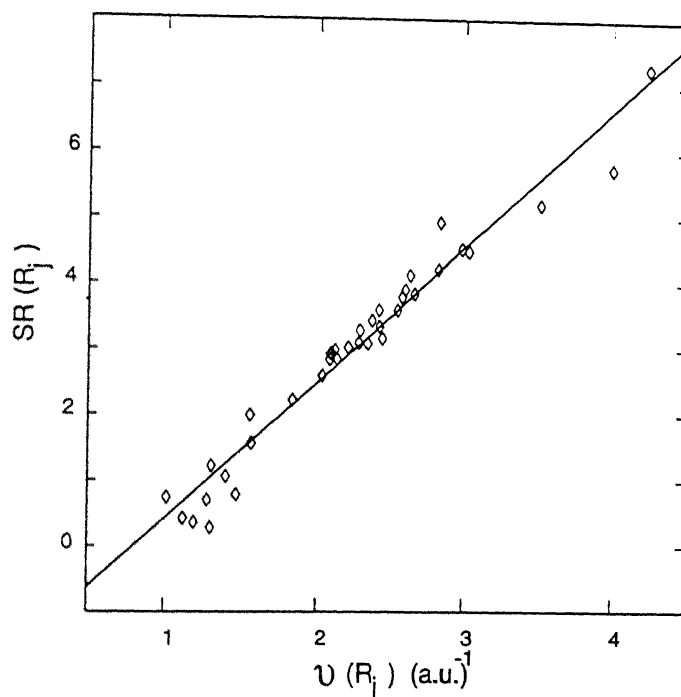


Figure 6.2: Linear relationship between the Sanderson electronegativity  $SR(R_j)$  and the REEL quantum scale  $\mathcal{V}(R_j) = \sqrt{n(R_j) - 1}/r_s(R_j)$  where  $n(R_j)$  and  $r_s(R_j)$  denote the principal quantum number of the valence shell and the  $l = 0$  orbital radius of the element respectively.

correlate the electronegativity  $SR(R_j)$  with the functional form  $f((n(R_j) - 1), r_s)$ . An inspection of figure 6.1 reveals that there is a systematic shift in the slope of the row wise plots. This insight, and some trial and error, led us to the discovery that  $SR$  scales linearly with the quantity [205]

$$\mathcal{V}(R_j) = \frac{\sqrt{n(R_j) - 1}}{r_s(R_j)} \quad (6.3)$$

which we call the valence shell renormalized electronegativity (REEL).

Fig. 6.2 depicts a linear scaling behavior:

$$SR(R_j) = a\mathcal{V}(R_j) + S_0 \quad (6.4)$$

Here the slope  $a$  and the intercept  $S_0$  are  $2.07 (\pm 0.02) \text{ a.u.}$  and  $-1.66 (\pm 0.006)$  respectively. The uncertainty in the calculated electronegativity is  $\pm 0.01$  and is of the same order as the uncertainty in the original electronegativity data [206]. For

Table 6.1: Stretching mode Si-H frequencies ( $\nu_{Si-H}$ ) for well established environments in crystalline (c-Si) and amorphous (a-Si) silicon. Data for c-Si are taken from Shi *et al.* [198] and for a-Si from Kniffler *et al.* [207]. The symbol 'd' represents a dangling bond.

No.	System	$\nu_{Si-H}$ (cm <sup>-1</sup> )	Remarks
1	(SiSiSi)SiH	1980-1990	c-Si
2	(CSiSi)SiH	2028-2030	c-Si
3	(SiSi)SiH <sub>2</sub>	2055-2066	c-Si
4	(CCSi)SiH	2083	c-Si
5	(CSi)SiH <sub>2</sub>	2105-2107	c-Si
6	(OSi)SiH <sub>2</sub>	2160-2162	c-Si
7	(OC)SiH <sub>2</sub>	2210-2218	c-Si
8	(O <sub>2</sub> Si)SiH	2193	a-Si
9	(O <sub>3</sub> )SiH	2247	a-Si
10	(O <sub>2</sub> )SiH <sub>2</sub>	2219	a-Si
11	(OSi <sub>2</sub> )SiH	2100	a-Si
12	(Sidd)SiH	1830-1840	c-Si
13	(CSid)SiH	1925-1931	c-Si
14	(Sid)SiH <sub>2</sub>	1957-1965	c-Si

larger values of  $\mathcal{V}$ , the stability ratio saturates. Our attempts to correlate  $SR(R_j)$  with the orbital radius  $r_p$  or  $(r_s + r_p)$  were not as successful.

### 6.2.2 Vibrational Spectra

We now establish the relationship between the Si-H stretching frequencies  $\nu_{Si-H}$  observed in silicon and the quantum scale defined by us. Table 6.1 lists some of the well known Si-H stretching bands observed in crystalline silicon (c-Si) and amorphous silicon (a-Si). The frequencies listed in the first seven rows are observed for c-Si and the next four for a-Si. The last three entries involve dangling bonds and are observed in c-Si. The values are taken from the data culled by Shi *et al.* [198] and Kniffler *et al.* [207]. As demonstrated by Fig. 6.3, one obtains a linear relationship between  $\nu_{Si-H}$  and our quantum scale.

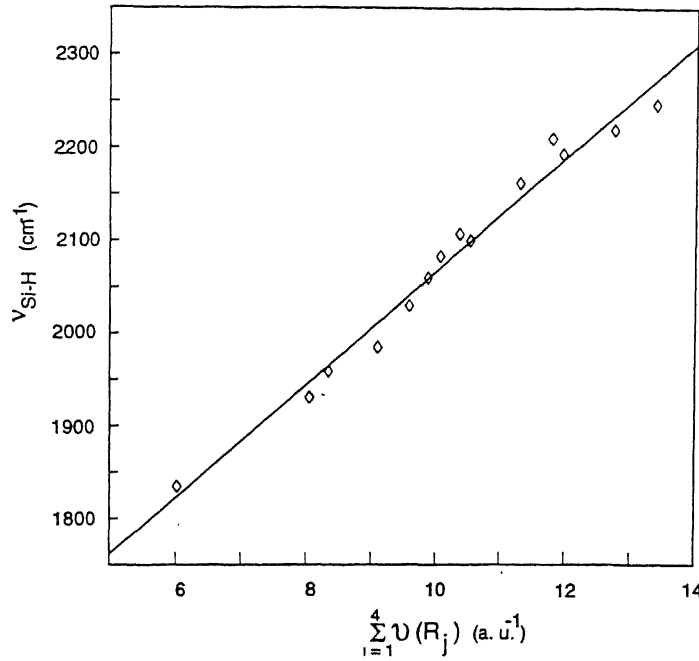


Figure 6.3: Linear relationship between the Si-H band stretching frequency  $\nu_{Si-H}$  and the quantum scale  $\sum_{j=1}^4 \mathcal{V}(R_j)$  where the summation runs over the four bonds of the central silicon atom.

$$\nu_{Si-H} = m \sum_{j=1}^4 \mathcal{V}(R_j) + \nu_0 \quad (6.5)$$

Here the summation is over all four nearest neighbors of the central Si atom and includes H. For H we have taken the relevant REEL value  $\mathcal{V}$  to be  $2.86 \text{ (a.u.)}^{-1}$ . For the dangling bond neither a  $n(R_j)$  nor a  $r_s(R_j)$  can be defined. To include it into our scheme we take  $\mathcal{V}$  to be  $0.54 \text{ (a.u.)}^{-1}$ . These values have been obtained from empirical fit to data. In Eq. (6.5), the slope  $m = 61.03 \text{ cm}^{-1}\text{-(a.u.)}$  and the intercept  $\nu_0 = 1456.45 \text{ cm}^{-1}$ . The uncertainties in the slope and the intercept are  $\Delta m = \pm 0.07 \text{ cm}^{-1}\text{-(a.u.)}$  and  $\Delta \nu_0 = \pm 7.3 \text{ cm}^{-1}$  respectively. The relationship given by Eq. (6.5) has predictive value with the attendant uncertainty  $\Delta \nu = \pm(11 - 16) \text{ cm}^{-1}$ . We shall employ it to obtain Si-H stretching frequencies in environments likely to occur in porous silicon.

## 6.3 Discussion

In Sec. 6.2, we have developed a phenomenological model to compute Si-H stretching mode vibrational frequencies for various environments that may occur within porous silicon. In this section, we discuss the existing assignments in literature for the infrared spectrum of porous silicon as reported by different groups. We focus on the Si-H stretching mode vibrations and suggest revisions of the existing assignments.

The Si-H<sub>n</sub> vibrational modes in a purely silicon environment reported in literature fall in three frequency ranges (i) 600 - 835 cm<sup>-1</sup> (bending modes), (ii) 870 - 916 cm<sup>-1</sup> (scissors mode) and (iii) 2050 - 2150 cm<sup>-1</sup> (stretching modes). As seen from Sec. 6.2, the frequencies depend largely on the immediate environment. In consonance with this, the Si-H stretching modes in a Si-O environment is shifted away from 2050 - 2150 cm<sup>-1</sup> and is seen to lie in the range 2150 - 2300 cm<sup>-1</sup>. A summary of the assignments reported for various vibrational modes is depicted in Fig. 6.4. Besides Si-H vibrational frequencies, Si-O modes are also seen in the figure.

There exists a consensus in literature regarding the assignments of the Si-H scissors and bending modes. The Si-H<sub>2</sub> scissors mode is reported by almost all workers to be in the range 870 - 916 cm<sup>-1</sup> (see Fig. 6.4). Ogata and coworkers also report the presence of an Si-H<sub>3</sub> bending mode in this range. All other workers report Si-H<sub>n</sub> (n = 1,2,3) bending modes in the range 600 - 835 cm<sup>-1</sup> as depicted in Fig. 6.4.

While there is a general agreement in the scientific community regarding the scissors and bending modes, there exists some disputes in literature over the detailed nature of the stretching mode vibrations. In particular, three peaks are observed in the range 2050 - 2150 cm<sup>-1</sup>, which were initially assigned to Si-H (2087 cm<sup>-1</sup>), Si-H<sub>2</sub> (2110 cm<sup>-1</sup>) and Si-H<sub>3</sub> (2140 cm<sup>-1</sup>) [210,211], but this has been contested by several works on amorphous silicon [212-214] as well as on porous silicon [191]. In this context, the values we have cited in Table 6.1 have been chosen from the data that has been obtained from crystalline silicon [198]. A linear relation of the form given by Eq. (6.5) is seen to hold extremely well for the given set of data.

The theoretical approaches to the evaluation of vibrational modes in silicon have relied on phenomenological schemes as well as *ab initio* electronic structure calculations. The first attempt to systematize and predict the vibrational modes in silicon clusters was based on a semi-empirical electronic structure calculation due to Singh

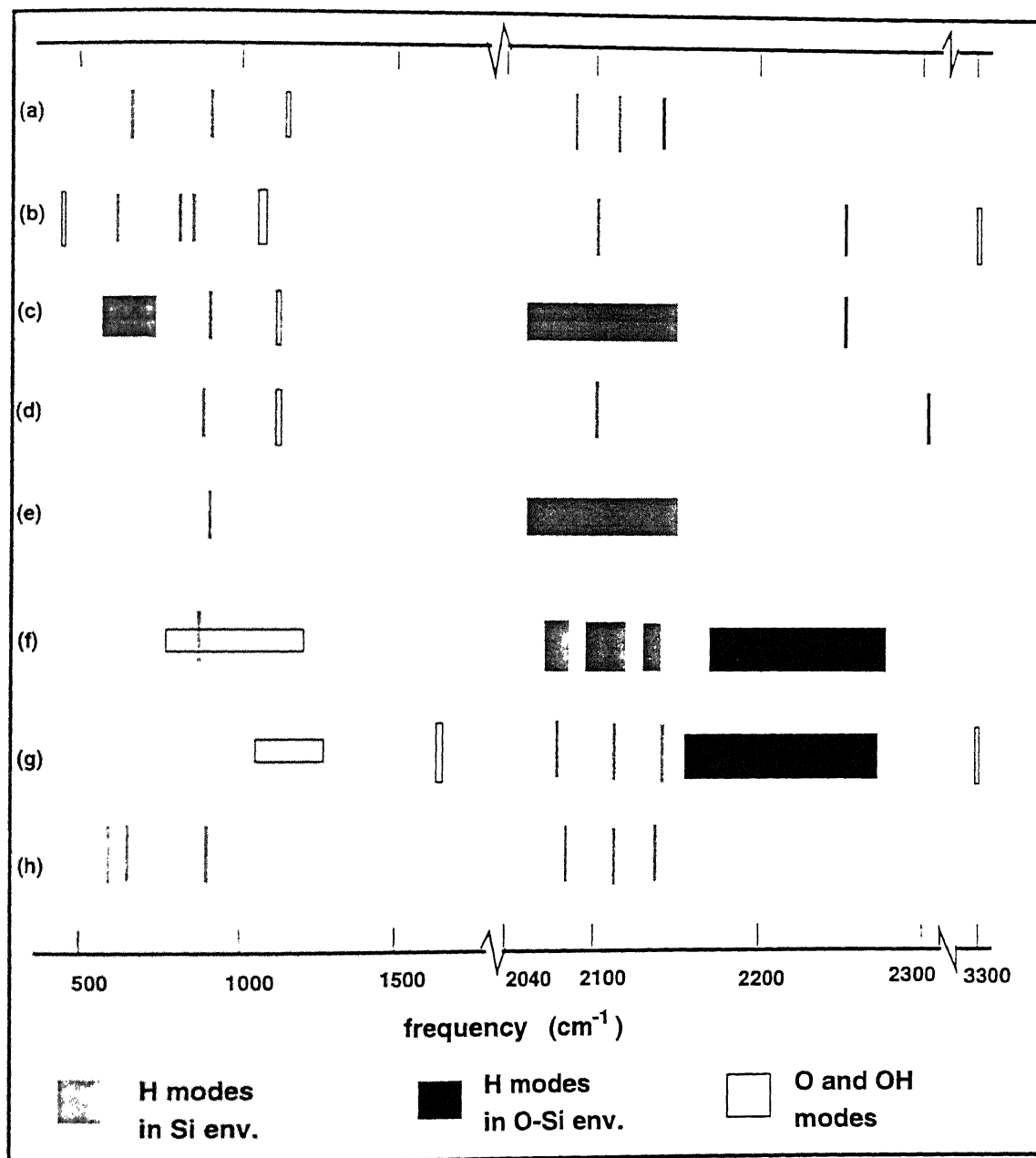


Figure 6.4: The vibrational spectra of Si-H and Si-O bonds in porous silicon reported by various groups: (a) Gupta *et al.* [191] (b) Brandt *et al.* [193] (c) Tischler *et al.* [22] (d) Tischler *et al.* [194] (e) Robinson *et al.* [195] (f) Schuppler *et al.* [57] (g) Dubin *et al.* [208] (h) Ogata *et al.* [209]. The figure divides the assignments made by the respective groups into three broad categories as shown. The detailed assignments are discussed in Sec. 6.3.



and coworkers [215]. Later, first principles calculations were carried out, along with experimental studies on the Si(100) surface by Chabal and Raghavachari to study the stretching modes of monohydride and dihydride silicon [216,217]. The monohydride symmetric mode was assigned to  $2099\text{ cm}^{-1}$  and the dihydride symmetric mode to  $2091\text{ cm}^{-1}$ . The calculations were limited to very small clusters, the largest cluster being  $\text{Si}_9\text{H}_{14}$ . The calculated frequencies were also found to be dependent on the level of the theoretical approximation. In another study, Deak *et al.* [53] have considered siloxene structures which are planar  $[\text{Si}_2\text{H}(\text{OH})]_{3n}$ , linear  $[\text{Si}_2\text{H}_2\text{O}]_{3n}$ , and ring-like  $[\text{Si}_6\text{H}_6\text{O}_3]_n$  as well as substituted ring-like siloxenes  $[\text{Si}_6\text{H}_{6-r}(\text{OH})_r\text{O}]_n$ . A judicious mix of quantum chemical techniques were employed to evaluate bond strengths, force constants and make infrared frequency predictions. A stretching frequency of  $2105\text{ cm}^{-1}$  was predicted for Si-H in the planar structure. This is in consonance with the dominant Si-H stretching band in porous silicon. A peak in this range is also observed in in-situ siloxene. In a recent work, Ogata and coworkers [209] perform detailed calculations similar to those of Chabal and Raghavachari [216] to predict the stretching as well as various deformation mode frequencies for the  $\text{Si-H}_n$  species in porous silicon. They find that the vibrational frequencies increase with increasing hydrogen content and assign the  $2087\text{ cm}^{-1}$  line to the Si-H stretching mode,  $2108\text{ cm}^{-1}$  line to  $\text{Si-H}_2$  and the  $2142\text{ cm}^{-1}$  line to  $\text{Si-H}_3$ .

The earlier phenomenological approaches to the prediction of infrared modes in silicon are due to Lucovsky [197] and Sahu and coworkers [199]. These are similar in spirit to the present work. Lucovsky employs three independent linear relations akin to Eq. (6.5)

$$\nu_{\text{Si-H}_n} = m_n \sum_{j=R_1, \dots, R_n} \text{SR}(R_j) + \nu_{0n} \quad n = 1, 2, 3 \quad (6.6)$$

where  $R_j$  are the various chemical ligands attached to silicon (other than hydrogen),  $\text{SR}(R_j)$  the respective Sanderson electronegativity and  $m_n$  and  $\nu_{0n}$  the characteristic constants of the linear relation. In a later work, Sahu and coworkers [199] replace Eqs. (6.6) by a single linear relation:

$$\nu_{\text{Si-H}} = 39.7 \sum_{j=1}^4 \text{SR}(R_j) - 1512.7$$

Note that the sum is over all nearest neighbors including hydrogen. Further, the Sanderson electronegativity of hydrogen is reassigned to 4.25 from 3.55. However, this

fit does not work well at high frequencies as there is a pronounced saturation effect in high electronegativity environments. In comparison, the linear relation established between REEL and the Si-H vibrational modes (Eq. 6.5) is seen to hold good for a wide range of frequencies (see Fig. 6.3).

The present study shows that the vibrational frequency increases with increasing hydrogen content (Eq. (6.5)). This is also supported by most of the theoretical calculations described earlier. A notable deviation from this trend is the assignment due to Gupta, Colvin and George [191] who notice that during thermal annealing, the peaks at  $2087\text{ cm}^{-1}$  and  $910\text{ cm}^{-1}$  exhibit an identical temperature dependence, where their magnitudes start decreasing from 550 K. Both peaks disappear completely by 720 K. In isothermal annealing, the time evolution of the integrated absorbance of these two peaks is nearly identical. Therefore, they assign the  $2087\text{ cm}^{-1}$  line to the Si-H<sub>2</sub> stretch mode, as it is well known that the  $910\text{ cm}^{-1}$  peak corresponds to the Si-H<sub>2</sub> scissors mode. It was also found that the  $2110\text{ cm}^{-1}$  peak initially increased in magnitude and eventually shifted down to  $2102\text{ cm}^{-1}$ . The variations in the peak intensities were shown to be consistent with a hypothesized conversion of Si-H<sub>2</sub> to Si-H and H<sub>2</sub>. Hence, the  $2110\text{ cm}^{-1}$  peak was assigned to Si-H. The  $2140\text{ cm}^{-1}$  peak was assigned to the Si-H stretching in an O-Si environment. This assignment compares favorably with the predictions of Chabal and Raghavachari [216,217], if we assume that only the symmetric modes of Si-H and Si-H<sub>2</sub> stretching are observed in the infrared spectrum of porous silicon.

The Si-H stretching mode frequencies for possible environments in porous silicon as predicted by Eq. (6.5) is reported in table 6.2. Based on these values, we attempt to reconcile the various systematics reported in different studies. Gupta and coworkers establish a strong correlation between the Si-H<sub>2</sub> scissors mode and the  $2087\text{ cm}^{-1}$  line. However, the predicted increase of the stretching frequency with increasing hydrogen content also needs to be accounted for. We note from table 6.1 that the Si-H stretching frequency in crystalline silicon is reported [198] to be  $\sim 2000\text{ cm}^{-1}$ . The frequency for Si-H<sub>3</sub> stretching mode calculated from Eq. (6.5) is  $\sim 2100\text{ cm}^{-1}$  (see Table 6.2). This suggests the assignment of  $2087\text{ cm}^{-1}$  to Si-H<sub>2</sub> and  $2110\text{ cm}^{-1}$  to Si-H<sub>3</sub> stretching modes, which is seen to be consistent with the experimental results of Gupta, Colvin and George and the theoretical trend predicted by the present work as well as Ogata and coworkers [209]. The  $2140\text{ cm}^{-1}$  line can be assigned to an

Table 6.2: Stretching mode Si-H frequencies ( $\nu_{\text{Si-H}}$ ) for possible environments in porous silicon. The  $\nu_{\text{Si-H}}$  have been calculated on the basis of Eq. (6.5). The symbol 'd' represents a dangling bond.

No.	System	$\nu_{\text{Si-H}}$ ( $\text{cm}^{-1}$ )
1	(Si)SiH <sub>3</sub>	2106
2	(OSi)SiH <sub>2</sub>	2146
3	(OC)SiH <sub>2</sub>	2175
4	(SiO <sub>2</sub> )SiH	2186
5	(F)SiH <sub>3</sub>	2223
6	(O <sub>3</sub> )SiH	2273
7	(F <sub>2</sub> )SiH <sub>2</sub>	2293
8	(Od)SiH <sub>2</sub>	2052
9	(Fd)SiH <sub>2</sub>	2082
10	(O <sub>2</sub> d)SiH	2092
11	(F <sub>2</sub> d)SiH	2152

oxygen complex (OSi)Si-H<sub>2</sub> as calculated from Eq. (6.5) (see Table 6.2). Recall from our earlier discussion that a similar suggestion has also been made by Gupta and coworkers [191].

While the location of the hydrogen related peaks in the vibrational spectra of porous silicon samples agree with that of H passivated Si(100) surfaces, the peaks are substantially broader with typical FWHM of  $\sim 20 \text{ cm}^{-1}$  as opposed to  $1 \text{ cm}^{-1}$  in crystalline Si. This may be due to the high degree of disorder present on the surface, as a result of surface contamination as well as geometrical relaxation of the surface Si atoms. Oxygen, fluorine and organic radicals can get introduced into the silicon system during the anodization of silicon in HF. Substituted oxygen and fluorine may give rise to  $\nu_{\text{Si-H}}$  in the range  $2050\text{-}2150 \text{ cm}^{-1}$ . Table 6.2 enumerates some of the possible environments with frequencies calculated using Eq. (6.5). The first four entries of  $\nu_{\text{Si-H}}$  fall in the range  $2050\text{-}2150 \text{ cm}^{-1}$  or are close to it. It has been reported that the number of dangling bonds in porous silicon increases upon UV illumination [194]. Hence we have also considered dangling bond environments. The

last four entries in table 6.2 suggest four such environments which may contribute to the observed  $\nu_{\text{Si-H}}$  line ( $2050 - 2150 \text{ cm}^{-1}$ ) in porous silicon. Note that the substitution of an oxygen atom in  $(\text{O}_3)\text{SiH}$  by a dangling bond reduces  $\nu_{\text{Si-H}}$  from  $2273 \text{ cm}^{-1}$  to  $2092 \text{ cm}^{-1}$ . Broad lines are also observed at  $\approx 850 \text{ cm}^{-1}$  and  $1100 \text{ cm}^{-1}$ . These lines have been assigned to Si-H<sub>2</sub> scissors mode and Si-O-Si stretching modes respectively in the past. However, Si-F related frequencies [209,218] also lie in the range  $800 \text{ cm}^{-1}$  to  $1030 \text{ cm}^{-1}$ . In view of the possible presence of fluorine in porous silicon, caution must be exercised in assigning frequencies to the observed infrared lines.

The changes in the surface chemical environment can also lead to geometrical relaxation of the cluster. In the *ab initio* calculations of Chabal and Raghavachari [216,217], it was found that the Si-H distance decreases slightly because of the strain present in the enhanced Si-Si distances (Si-Si in the cluster was found to be  $2.51 \text{ \AA}$  whereas the bulk value is  $2.35 \text{ \AA}$ ). In the first principles calculations of Buda and coworkers [41], the surface Si-Si distances were found to be relaxed by  $0.15 \text{ \AA}$ , and hence  $d(\text{Si-Si}) = 2.5 \text{ \AA}$ . It is therefore reasonable to assume that in porous silicon, the Si-H distances are somewhat lower. Using the phenomenological formula [197]

$$\nu_{\text{Si-H}} d_{\text{Si-H}}^3 = 7074 \text{ \AA cm}^{-1} \quad (6.7)$$

we obtain, the variation in the vibrational frequency  $\Delta\nu$  to be

$$\Delta\nu = \frac{21222}{d_{\text{Si-H}}^4} \Delta d_{\text{Si-H}}$$

For a value of  $\Delta d_{\text{Si-H}} = 0.3 \text{ \AA}$ ,  $\Delta\nu$  works out to be  $1257 \text{ cm}^{-1}$ . Thus a small variation in the Si-H distance can lead to a large variation in the vibrational frequency. This could lead to an upshift in the frequencies as well as a broadening of the peaks if there is a distribution of Si-H distances. Further, based on the observed range of  $\nu_{\text{Si-H}}$  in porous silicon, Eq. (6.7) suggests that  $d_{\text{Si-H}}$  is confined to  $\{1.49 - 1.51\} \text{ \AA}$ . This should be a useful guide in electronic structure calculations where the dangling bonds are passivated by hydrogen. Values such as  $d_{\text{Si-H}} = 1.637 \text{ \AA}$  or  $d_{\text{Si-H}} = 1.17 \text{ \AA}$  employed in these calculations [39,45] are clearly out of range.

## 6.4 Conclusion

The present work postulates a renormalized electronegativity scale REEL based on the principal quantum number  $n$  and the orbital radius  $r_s$ . Consequently, this new scale is purely non-empirical in character. A universal relationship between the Sanderson electronegativity and our quantum scale  $\mathcal{V}$  defined by Eq. (6.4) has been established. This relation is seen to be valid for almost the entire periodic table. A detailed discussion of the renormalized electronegativity scale in the context of extant phenomenological scales is to be found elsewhere [205]. In this chapter, we have highlighted the utility of our scale in assigning vibrational modes to Si-H stretching in porous silicon. This approach can be gainfully extended to study the infrared spectra of ligands other than hydrogen as well as other semiconductors.

One may extend this work to  $\nu_{\text{Si-H}}$  in silane molecules substituted by organic radicals such as  $\text{CH}_3$ ,  $\text{C}_2\text{H}_5$ ,  $\text{C}_6\text{H}_5$  etc. The  $SR$  values for these radicals can be calculated using Lucovsky's prescription [197],

$$SR = \left( \prod_{j=1}^n SR(R_j) \right)^{1/n}$$

where  $SR(R_j)$  represents the Sanderson electronegativity values of the component elements. The linear fit in Fig. 6.2 enables us to define an effective  $\mathcal{V}(R_j)$  using these  $SR$  values. One may then look for a correlation between  $\nu_{\text{Si-H}}$  and these values of  $\mathcal{V}(R_j)$ . We have carried out such an exercise for  $\text{SiH}(R\text{Cl}_n)$  ( $n = 0.1.2$ ) where  $R$  stands for the radicals and found an approximate linear relationship akin to Fig. 6.3.

Chlorine is known to be a good dangling bond passivator in silicon. We have also discovered a linear relationship between the Si-Cl stretching mode frequency and our quantum scale. We use the data for  $\nu_{\text{Si-Cl}}$  in a-Si cited by Wu et al. [219]. Fig. 6.5 depicts this correlation. Except for the highly electronegative environment  $(\text{Cl}_3)\text{SiCl}$ , the data is linear to a good approximation.

Our model has focused mainly on the identification of Si-H modes in porous silicon. Hydrogen plays a key role in silicon. In c-Si, it is known to passivate both deep and shallow impurities [220]. In porous silicon, the presence of hydrogen is linked to surface passivation which facilitates efficient luminescence. We also show that this model can be used to study the vibrational modes of other impurities.

The past assignments of the vibrational spectra of PS to specific transitions exhibit

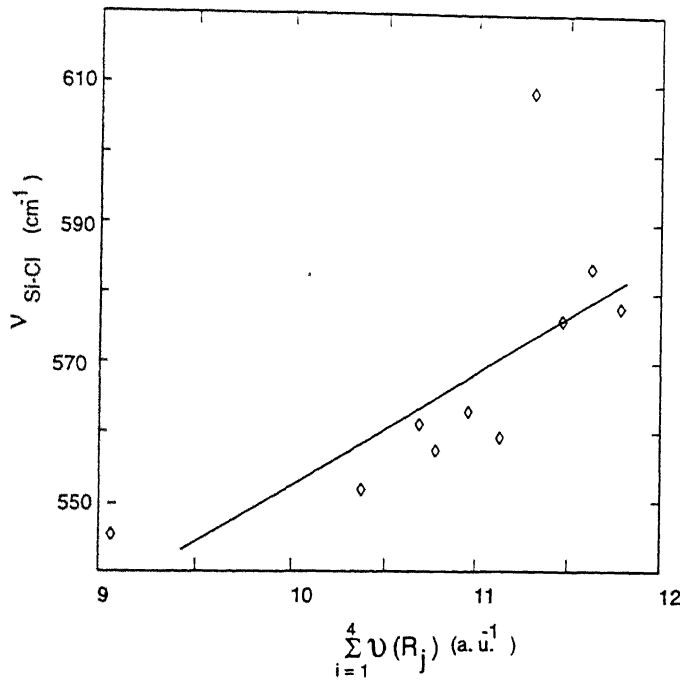


Figure 6.5: Linear relationship between the Si-Cl bond stretching frequency  $\nu_{Si-Cl}$  and the quantum scale  $\sum_{j=1}^4 \nu(R_j)$ .

some inconsistencies. Our model has limited value in making exact identifications, but suggests systematic variations in the vibrational spectrum with the addition (or removal) of other elements to the Si-H environment. For example, Shanks and coworkers [212] state that the shift of the  $2000 \text{ cm}^{-1}$  line on annealing to  $2100 \text{ cm}^{-1}$  is due to the introduction of two dangling bonds. However, our work seems to indicate that the introduction of dangling bonds can only lower the vibrational frequency as mentioned earlier. Thus the trends suggested by the present work can be used to improve upon existing results. Again, our model contradicts some of the assignments due to Gupta, Colvin and George [191] who posit a decrease in the vibrational frequency as the number of neighboring hydrogen atoms are increased. The main utility of this model thus lies in correlating changes in the vibrational spectrum with specific changes in the surface environment, which are known to play a major role in porous silicon photoluminescence. The PL spectra of siloxene, a complex considered responsible for the luminescence in porous silicon, can also be varied by the introduction of halides or organic radicals [193]. In porous silicon, post anodization surface treat-

ment modifies the PL spectra [221]. This is perhaps due to the formation of molecular complexes on the surface of porous silicon. Some insight into this phenomena can be obtained by studying the vibrational spectra. Our approach provides a valuable tool to correlate the PL spectra of various samples with their vibrational spectra. This can serve to characterize the porous silicon surface.

## Key Reference

The major reference for the material contained in this chapter is:

- George C. John and Vijay A. Singh, Phys. Rev. **B 53**, 9831-9837 1996).

# Chapter 7

## Conclusion

Traditionally, the physicists have adopted a reductionist approach to materials physics, focusing on the extrapolation of individual atomic properties to macroscopic collections of atoms [222]. The quantum chemists carry out electronic structure calculations on molecules consisting of  $< 10^2$  atoms. Solid state physicists compute the band structure of infinite solids by applying periodic boundary conditions on a unit cell consisting of  $\leq 10$  atoms. Over the last decade, the increasing technological importance of nanocrystalline materials have called for a detailed, microscopic analysis of atomic clusters of the size  $10^3 - 10^4$  atoms [223]. Such clusters are found to exhibit properties surprisingly distinct from the molecular and bulk limits. This regime, bridging the microscopic ( $< 10^2$ ) atoms and the macroscopic ( $> 10^6$ ) atoms, has been termed *mesoscopic*. (See Fig. 7.1).

Porous silicon, the material that we have examined in some detail in this thesis, belongs to this category of nanocrystalline materials. However, unlike the III-V quantum wells or dots which are normally fabricated under controlled conditions using sophisticated techniques such as molecular beam epitaxy (MBE) or metal organic chemical vapor deposition (MOCVD), porous silicon can be fabricated easily and economically - in fact in most undergraduate laboratories. In this sense, porous silicon could be described as the "poor man's quantum dot."

Porous silicon is easily fabricated. Its PL is present for all to see. But the agony of the situation is not merely confined to the lack of success in presenting a unified model for the optical behavior. The holy grail of porous silicon research, namely a commercially viable electroluminescent device continues to remain elusive. The



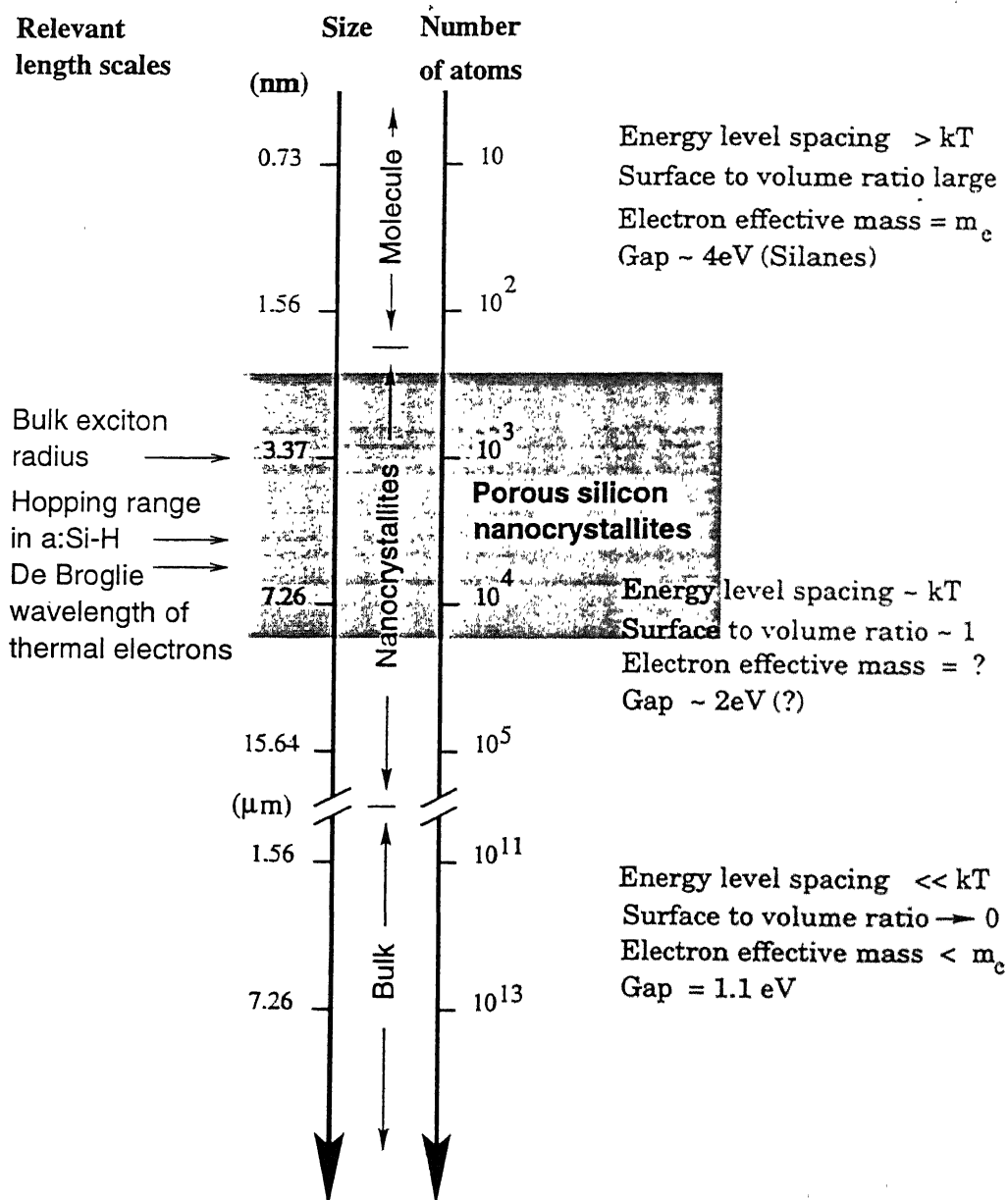


Figure 7.1: Transition from the molecular regime to the bulk solid. Nanocrystallites and quantum dots fall in the intermediate mesoscopic region. The shaded area depicts the size range of luminescing crystallites in porous silicon. Also shown are the schematic variation in properties. The mass of the free electron is represented by  $m_e$ . The diameter  $d$  of a cluster of  $N$  atoms is  $d = (3N/4\pi)^{1/3}a_0$  where  $a_0 = 0.357\text{ nm}$ , the silicon lattice constant. Uncertain values are indicated by question marks.

large luminescence decay times ( $10^{-4}$  s) may render it unsuitable for optoelectronic applications requiring smaller response times. Efforts to obtain efficient electroluminescence have been disappointing and we face a technological bottleneck. At the time of writing this thesis, there has been reports of the successful fabrication of an integrated optoelectronic circuit incorporating porous silicon [224]. Though the speed and efficiency of this circuit needs to improve further, this achievement seems to hold out some promise for the future of porous silicon.

The lack of control over the formation process leads to a high degree of disorder in the system as mentioned earlier in the thesis. To obtain a reasonable theory of porous silicon, one needs to look beyond the properties of individual silicon nanocrystallites. The hierarchical disorder (see Sec. 1.4) has to be accounted for, and one should attempt to study the "collective microstructure" of the system consisting of crystallites of various sizes and shapes.

Phenomenological theories for porous silicon formation employ experimentally familiar parameters such as the anodization potential, electrolyte concentration etc., to qualitatively argue the case for pore formation in silicon. On the other hand, computer simulation models of chapters 2 and 3 employ rules of growth which are not explicitly related to the experimental growth parameters. Thus, these theories are in a sense "indirect." The drift-diffusion model described in chapter 2 successfully reproduces the various morphological transitions observed in porous silicon with the tuning of experimental parameters. The PS formation problem is thus identified as one belonging to the larger class of non-equilibrium growth phenomena, where the competition between two antithetical parameters give rise to various morphological classes. It would be worthwhile to explore this further so that the competing phenomena may be identified and their relevance to the simulation parameters established.

The diffusion induced nucleation model for porous silicon formation discussed in chapter 3 successfully explains (i) a constant rate of growth, (ii) the dependence of the rate of growth on the anodization potential, (iii) high porosity structures similar to samples exhibiting visible photoluminescence and (iv) electropolishing of silicon in the high potential limit. It would be desirable to carry out further studies using this model to establish a proper correspondence between the parameters of the simulation and the experiment. One needs to explain the occurrence of the constant porosity profile as well as the nearly planar film front.

A desirable goal is the formulation of a computational model which can simulate the fabrication process on a computer. Simulation studies of molecular beam epitaxy (MBE) growth of AlGaAs/GaAs semiconductor wells is a good example [225]. The DIN model discussed in chapter 3 can be used to study the effect of substrate roughness on porosity. The effect of placing inert masks on the substrate surface during the dissolution process can also be explored. Thus, the model can be extended to design experiments to fabricate porous silicon layers of varying geometry.

The porous silicon community continues to remain divided as to the exact nature of the radiative process. Of the three categories of models described in Sec. 1.3, namely (i) the quantum confinement model, (ii) the chemical luminescence model, and (iii) the hybrid model, the quantum confinement hypothesis seems to be the simplest and the most appealing. Recently, the quantum confinement model has been reinforced by two experiments. Schuppler and coworkers [57] have obtained visible photoluminescence from Si nanocrystallites of about 1.5 nm diameter. They contend that the luminescence in porous silicon is due to dots/columns of size  $< 1.5$  nm, as opposed to the earlier belief that the sizes are typically 3 nm. In Si/SiO<sub>2</sub> superlattices grown using molecular beam epitaxy, an unambiguous blue shift in the PL peak position with decreasing layer thickness in the range  $d \sim 1.5 - 3$  nm has been observed by Lockwood and coworkers [17]. Further, employing soft X-ray edge absorption spectroscopy and X-ray photo emission spectroscopy, they have measured the conduction band upshift and the valence band downshift respectively. For  $d = 1.5$  nm, the valence band downshift is 0.1 eV and the conduction band upshift is 0.3 eV. Note that these measurements are in conflict with the effective mass based calculations described in Sec. 1.3.1, which predict a larger shift for the valence band [19].

The influence of the surface in the recombination process cannot be ruled out. Consider the QCM where an electron is radiatively excited into the conduction band. The experimental luminescence time constant  $\tau > 1\mu\text{sec}$ . A simple particle in a box picture indicates that within this time the electron can sample the nanocrystallite surface roughly ten million times. Alternatively, we know that the electron mobility  $\mu_n$  in bulk silicon is 500 cm<sup>2</sup>/volt-sec. From the Einstein relation the diffusion constant  $D_n = \mu_n kT/q = 12.5\text{cm}^2/\text{sec}$ . Given the crystallite size of 3 nm, the transit time to the surface is in the femtosecond range and much smaller than the luminescence

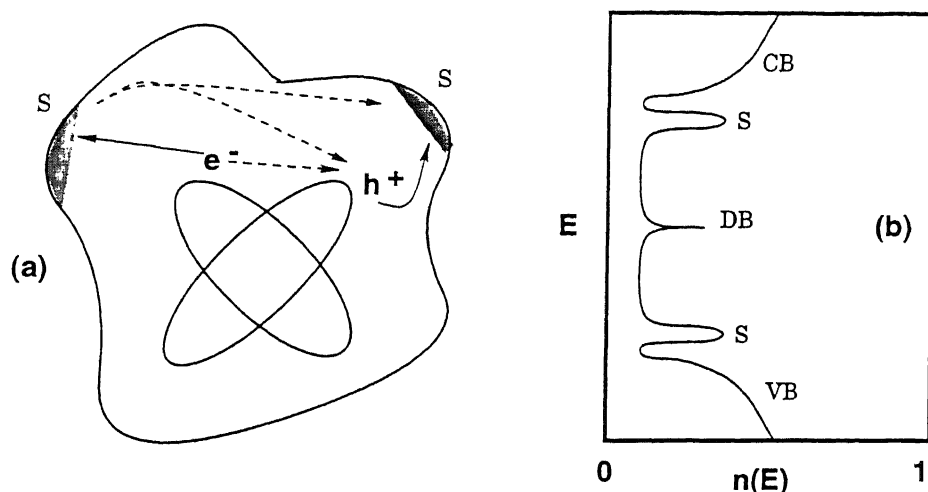


Figure 7.2: Role of surface states in the luminescence process. Fig. (a) depicts the schematic structure of a crystallite. The electron hole pair (ellipses) can get trapped in the surface states depicted by the shaded regions (solid arrow). Possible recombination pathways are indicated by the broken arrow. Fig. (b) shows the density of states  $n(E)$  in a realistic nanocrystallite, with a  $\cup$  shaped distribution of surface states  $S$  near the band edges  $CB$  (conduction band) and  $VB$  (valence band). The peak near the mid-gap region is due to dangling bonds ( $D$ ) (also see Sec. 1.3). According to the Berthelot hopping model discussed in chapter 5, the surface states could act as pathways for carrier hopping.

time.

Surface related chemical mechanisms would be a cause for concern where the applications of PL are involved, and perhaps, the scientific community wants a more “physical theory.” The presence of quantum confinement is clearly established by the shift in the absorption edge from 1.1 eV for bulk silicon to over 1.6 eV for a luminescing porous silicon layer. Hence, the variety of hybrid models which invoke both quantum confinement and the surface chemistry, seems an attractive compromise. These models assign roles to the core, surface, and dangling bond related states, but differ in the identification of radiative transitions responsible for the visible PL (see Fig. 7.2). The possible transitions are many - band to band ( $CB \rightarrow VB$ ), bound state to band ( $S/DB \rightarrow VB$ ,  $CB \rightarrow S/DB$ ) or bound state to bound state ( $S/DB \rightarrow S/DB$ ). Hence these models do not come up with specific predictions, are vague, and flexible enough to accommodate experimental contingencies. In short, these theories

are non-falsifiable and hence not “scientific” in Karl Popper’s sense of the term [226].

From the course of the discussions on photoluminescence, it is clear that the source of luminescence consists of nanocrystalline structures which could be as small as 1 nm. This translates to around  $10^2 - 10^3$  atoms per crystallite (see Fig. 7.1). This is the regime where the molecular calculations of quantum chemistry meet the traditional solid state calculations. The question now arises whether one should view the problem of porous silicon in a reductionist fashion, i.e., as a simple extrapolation of the properties of a constituent nanocrystallite. This approach has enjoyed a degree of success as elucidated in chapter 4. In this chapter, we have shown that the assumption of a Gaussian distribution of crystallite sizes can successfully explain the observed shape of the emission spectrum. This calculation also explains the disparities in the excitonic binding energies which need to be assumed by electronic structure calculations reviewed in Sec. 1.4. Thus, the necessity of incorporating the disorder inherent to the porous silicon system is highlighted.

The spectral linewidth is an important parameter in the fabrication of light emitting devices. Chapter 4 explains the observed line width as a simple sum of the contributions due to individual crystallites. The carrier hopping length scale  $S$  of the model in chapter 5 is of the order of the crystallite size (1 – 5 nm.). Workers have also tried to model carrier transport using a variable range hopping model (see Sec. 5.5). Hence the calculations of chapter 4 can be improved upon by accounting for the collective behavior of the crystallites. Recently, there have been reports of a reduction in the PL line width due to electronic coupling in a stack of indium arsenide quantum dots separated by gallium arsenide layers [227,228]. One needs to look for similar phenomena in porous silicon. These considerations assume importance if one attempts to fabricate semiconductor lasers from porous silicon.

A consequence of the ongoing debate about the photoluminescence mechanism has been the accumulation of a mountainous volume of experimental data on the optical behavior of silicon. The results from various experimental groups, which have often been advanced in support of a particular hypothesis, need to be explained under a common “unified” model. Chapter 5 presents a phenomenological scheme which lays the foundations for such a unification. Our model invokes the competition between (i) an Arrhenius type radiative process and (ii) a Berthelot type carrier hopping process to explain wide ranging phenomena such as,

- The variation of luminescence intensity with temperature, with a maximum in the range 50 – 150 K.
- The exponential drop in intensity with increasing pressure.
- The faster luminescence decay with increasing temperature.

Assuming a quantum confinement model (see Fig. 5.1), one can extend the above phenomenological scheme to explain

- The variation of the luminescence decay time with emission energy.
- The anomalous variation in the PL peak position with temperature, which shows both blue and redshifts.
- The dependence on the PL peak energy on applied pressure as well as the pressure transmitting medium.

Thus our approach is seen to support the quantum confinement hypothesis. This model can also explain, to some extent, the high surface sensitivity of PL as the Berthelot process is most likely to be a surface related mechanism. For instance, the carrier hopping could take place between the surface states in the gap (see Fig. 7.2), whereas the light emission occurs as a consequence of re-excitation into the bands and subsequent band to band recombination.

There does exist several observations that fall outside the ambit of the model proposed in chapter 5. The disparities in the absorption and emission edges cannot be addressed within our scheme. The electroluminescence from PS is found to be extremely weak. This can be attributed to a surface dominated transport process which results in poor carrier injection into the crystallites. The model should be extended to address transport related phenomena such as persistent photoconductivity [229].

The exact nature of the vibrating barrier assumed in chapter 5 is still unclear. However, it is well known that several vibrating species are present on the PS surface, the frequencies of which have been linked to a theoretical electronegativity scale in chapter 6. Using the renormalized electronegativity scale defined in chapter 6, one may attempt to predict the possible environments that can give rise to vibrating barriers in the desired frequency range. However, such an approach needs to be

augmented by appropriate experiments to vary the surface composition of the silicon crystallites in a controlled manner.

The main utility of the phenomenological model outlined in chapter 6 lies in correlating changes in the vibrational spectrum to changes in the surface chemistry. This scheme can be used to predict the surface composition by observing the infrared vibrational spectra after post-anodization treatments. The variations in the luminescence behavior can then be attributed to the presence (absence) of specific chemical species on the surface.

Summarizing, we have, in this thesis

- Proposed a generalized computational scheme to model aggregation and etching phenomena.
- Successfully extended this model to explain porous silicon formation during the anodization of silicon in HF.
- Proposed a theoretical framework to explain the observed spectral shape in porous silicon photoluminescence. This framework provides two parameters, the mean diameter  $d_0$  and variance  $\sigma$  of the nanocrystallite size distribution which can perhaps be used to characterize the porous silicon sample.
- Proposed a novel phenomenological model to explain a large body of data on the optical behavior of porous silicon under a “unified theory.” This model suggests a valuable characterizing parameter,  $T_B$ , the Berthelot temperature, which is also experimentally easily accessible.
- Defined a novel quantum scale which is then successfully employed to predict the vibrational spectra of defects in porous silicon.

The computational models of porous silicon formation can be gainfully extended to aid device design and fabrication. The phenomenological models of chapters 4, 5 and 6 suggest novel characterizing scales and provide a firm mathematical basis for predicting the optical behavior as well as the vibrational spectra of porous silicon. This can constitute a basis for further microscopic calculations which need to take into account the mesoscopic, disordered nature of the system.

# References

- [1] L.T.Canham, Appl. Phys. Lett. **57**, 1046 (1990).
- [2] G. C. John and V. A. Singh, Phys. Reports **263**, 93 (1995).
- [3] L.E.Brus, J. Phys. Chem. **98**, 3575 (1994).
- [4] Y.Kanemitsu, Phys. Reports **263**, 1 (1995).
- [5] B.Hamilton, Semicond. Sci. Technol. **10**, 1187 (1995).
- [6] *Light Emission From Silicon*, MRS Symposia Proceedings No:256. edited by S.S.Iyer, R.T.Collins, and L.T.Canham (Materials Research Society, Pittsburgh, 1992).
- [7] *Microcrystalline Semiconductors: Materials Science and Devices*, MRS Symposia Proceedings No:283, edited by P.M.Fauchet, C.C.Tsai. and L.T.Canham (Materials Research Society, Pittsburgh, 1993).
- [8] *Silicon Based Optoelectronic Materials*, MRS Symposia Proceedings No:298, edited by M.A.Tischler, R.T.Collins, M.L.Thewalt. and G.Abstreiter (Materials Research Society, Pittsburgh, 1993).
- [9] *Microcrystalline and Nanocrystalline Semiconductors*, MRS Symposia Proceedings No:358, edited by R.W.Collins *et al.* (Materials Research Society, Pittsburgh, 1995).
- [10] A.Uhlir, Bell Syst. Tech. J. **35**, 333 (1956).
- [11] R.L.Smith and S.D.Collins, J. Appl. Phys. **71**, R1 (1992).
- [12] M.I.J.Beale *et al.*, J. Cryst. Growth **73**, 622 (1985).



- [13] H.Takagi, M.Mitome, R.Yano, and T.Nakagiri. Solid State Phys. **27**, 875 (1992).
- [14] Y.Kanemitsu *et al.*, Phys. Rev. B **48**, 2827 (1993).
- [15] R.E.Hummel, A.Morrone, M.Ludwig, and S.S.Chang, Appl. Phys. Lett. **63**, 2771 (1993).
- [16] Z.H.Lu, D.J.Lockwood, and J.-M.Baribeau, Nature **378**, 258 (1995).
- [17] D.J.Lockwood, Z. Lu, and J.-M.Baribeau, Phys. Rev. Lett. **76**, 539 (1996).
- [18] K.Werner, IEEE Spectrum **31**, 30 (July 1994).
- [19] M.Voos *et al.*, Appl. Phys. Lett. **61**, 1213 (1992).
- [20] H.D.Fuchs *et al.*, Phys. Rev. B **48**, 8172 (1993).
- [21] M.Stutzmann *et al.*, J. Lumin. **57**, 321 (1993).
- [22] M.A.Tischler and R.T.Collins, Solid State Commun. **84**, 819 (1992).
- [23] T.K.Sham *et al.*, Nature **363**, 331 (1993).
- [24] S.M.Prokes *et al.*, Phys. Rev. B **45**, 13788 (1992).
- [25] Y.Kanemitsu, K.Suzuki, Y.Nakaoshi, and Y.Nasumoto, Phys. Rev. B **46**, 3916 (1992).
- [26] S.M.Prokes and O.J.Glembocki, Phys. Rev. B **49**, 2238 (1994).
- [27] Y.Kanemitsu, Phys. Rev. B **49**, 16845 (1994).
- [28] F.Koch, Mat. Res. Soc. Proc. **283**, 319 (1993).
- [29] F.Koch, V.Petrova-Koch, and T.Muschik, J.Lumin. **57**, 271 (1993).
- [30] P.M.Fauchet *et al.*, Mat. Res. Soc. Symp. Proc. **298**, 271 (1993).
- [31] Y.H.Xie *et al.*, Phys. Rev. B **49**, 5386 (1994).
- [32] K.Barla *et al.*, J. Cryst. Growth **68**, 727 (1984).

- [33] H.Sugiyama and O.Nittono, J. Cryst. Growth **103**, 156 (1990).
- [34] P.Hohenberg and W.Kohn, Phys. Rev. **136**, B864 (1964).
- [35] W.Kohn and L.J.Sham, Phys. Rev. **140**, A1133 (1965).
- [36] R.O.Jones and O.Gunnarsson, Rev. Mod. Phys. **61**, 689 (1989).
- [37] W.E.Pickett, Comments in Sol. State Phys. **12**, 1 (1986).
- [38] W.E.Pickett, Comments in Sol. State Phys. **12**, 57 (1986).
- [39] A.J.Read *et al.*, Phys. Rev. Lett. **69**, 1232 (1992). (E) **70**, 2050 (1993).
- [40] R.J.Needs *et al.*, Phys. Rev. B **50**, 14223 (1994).
- [41] F.Buda, J.Kohanoff, and M.Parinello, Phys. Rev. Lett. **69**, 1272 (1992).
- [42] T.Ohno, K.Shiraishi, and T.Ogawa, Phys. Rev. Lett. **69**, 2400 (1992).
- [43] C.-Y. Yeh, S.B.Zhang, and A.Zunger, Phys. Rev. B **50**, 14405 (1994).
- [44] J.-B.Xia and Y.-C. Chang, Phys. Rev. B **48**, 5179 (1993).
- [45] G.D.Sanders and Y.-C.Chang, Appl. Phys. Lett. **60**, 2525 (1992).
- [46] B.Delley and E.F.Steigmeier, Phys. Rev. B **47**, 1397 (1993).
- [47] J.P.Proot, C.Delerue, and G.Allan, Appl. Phys. Lett. **61**, 1948 (1992).
- [48] C.Delerue, G.Allan, and M.Lannoo, Phys. Rev. B **48**, 11024 (1993).
- [49] X. Wang *et al.*, Phys. Rev. Lett. **71**, 1265 (1993).
- [50] S.Furukawa and T.Miyasato, Phys. Rev. B **38**, 5726 (1988).
- [51] Y.Kayanuma, Solid State Commun. **59**, 405 (1986).
- [52] S.Sawada, N.Hamada, and N.Ookubo, Phys. Rev. B **49**, 5236 (1994).
- [53] P.Deak *et al.*, Phys. Rev. Lett. **69**, 2531 (1992).
- [54] Y.Takeda *et al.*, J. Appl. Phys. **73**, 1924 (1993).

- [55] G.Allan, C.Delerue, and M.Lannoo, J. Lumin. **57**, 239 (1993).
- [56] G.Allan, C.Delerue, and M.Lannoo, Phys. Rev. B **48**, 7951 (1993).
- [57] S.Schuppler *et al.*, Phys. Rev. B **52**, 4910 (1995).
- [58] J.C.Vial *et al.*, Phys. Rev. B **45**, 14171 (1992).
- [59] G. C. John and V. A. Singh, Phys. Rev. B **50**, 5329 (1994).
- [60] X.L.Zheng, W.Wang, and H.C.Chen, Appl. Phys. Lett. **60**, 986 (1992).
- [61] K.L.Narasimhan, S.Banerjee, A.K.Srivastava, and A.Sardesai, Appl. Phys. Lett. **62**, 331 (1993).
- [62] A.K.Sood, K.Jayaram, and D.V.S.Muthu, J. Appl. Phys. **72**, 4963 (1992).
- [63] H.M.Cheong *et al.*, Phys. Rev. B **52**, R11577 (1995).
- [64] C. Van de Walle and J.E.Northrup, Phys. Rev. Lett. **70**, 1116 (1993).
- [65] K.Murayama, H.Komatsu, S.Miyazaki, and M.Hirose, Jpn. J. Appl. Phys. **34**, 176 (1995).
- [66] K.Murayama, S.Miyazaki, and M.Hirose, Jpn. J. Appl. Phys. **31**, L1358 (1992).
- [67] Y.Kang and J.Jorne, J. Electrochem. Soc. **140**, 2258 (1993).
- [68] A.Valance, Phys. Rev. B **52**, 8323 (1995).
- [69] W.W.Mullins and R.F.Sekerka, J. Appl. Phys. **34**, 323 (1963).
- [70] W.W.Mullins and R.F.Sekerka, J. Appl. Phys. **35**, 444 (1964).
- [71] *On Growth and Form*, NATO ASI Series E No 100, edited by H.E.Stanley and N.Ostrowsky (Martinus Nijhoff, Cargese, France, 1985).
- [72] G. C. John and V. A. Singh, Phys. Rev. E **53**, 3920 (1996).
- [73] H.J.Herrmann, Phys. Reports **136**, 153 (1986).
- [74] D.Dhar and R.Ramaswamy, Phys. Rev. Lett. **54**, 1346 (1985).

- [75] Y.Sawada, A.Dougherty, and J.P.Gollub, Phys. Rev. Lett. **56**, 1260 (1986).
- [76] D.Grier, E.Ben-Jacob, R. Clarke, and L.M.Sander, Phys. Rev. Lett. **56**, 126 (1986).
- [77] E. Ben-Jacob and P.Garik, Nature **343**, 523 (1990).
- [78] D. G. Grier, D. A. Kessler, and L.M.Sander, Phys. Rev. Lett. **59**, 2315 (1987).
- [79] P.Garik *et al.*, Phys. Rev. Lett. **62**, 2703 (1989).
- [80] M.Eden, Proc. 4th Berkeley Symp. Math. Stat. Prob. **4**, 223 (1961).
- [81] T.A.Witten and L.M.Sander, Phys. Rev. Lett. **47**, 1400 (1981).
- [82] J.Feder, *Fractals* (Plenum, New York, 1988).
- [83] T. Vicsek, Phys. Rev. Lett. **53**, 2281 (1984).
- [84] R.F.Voss, J. Stat. Phys. **36**, 861 (1984).
- [85] J.Erlebacher, P.C.Searson, and K.Sieradzki, Phys. Rev. Lett. **71**, 3311 (1993).
- [86] O.Shochet *et al.*, Physica A **181**, 136 (1992).
- [87] O.Shochet *et al.*, Physica A **187**, 87 (1992).
- [88] P.Meakin, in *Phase Transitions and Critical Phenomena Vol.12*, edited by C.Domb and T.L.Lebowitz (Academic, New York, 1988).
- [89] R.C.Ball and R.M.Brady, J.Phys.A **18**, L809 (1985).
- [90] R.L.Smith, S.-F.Chuang, and S.D.Collins, J. Electron. Mater. **17**, 533 (1988).
- [91] J.Erlebacher, K.Sieradzki, and P.C.Searson, J. Appl. Phys. **76**, 182 (1994).
- [92] E.Ben-Jacob *et al.*, Phys. Rev. Lett. **57**, 1903 (1986).
- [93] G.C.John and V.A.Singh, Phys. Rev. B **52**, 11125 (1995).
- [94] M.Matsushita, Y.Hayakawa, and Y.Sawada, Phys. Rev. A **32**, 3814 (1985).
- [95] P. Meakin, Phys. Rev. A **27**, 2616 (1983).

- [96] P. Meakin, Phys. Rev. B **30**, 4207 (1984).
- [97] P.Meakin and J.M.Deutch, J. Chem. Phys. **85**, 2320 (1986).
- [98] M.Nauenberg, Physics Reports **103**, 173 (1984).
- [99] V.Lehmann and H.Foll, J. Electrochem. Soc. **137**, 653 (1990).
- [100] P.C.Searson, Appl. Phys. Lett. **59**, 832 (1991).
- [101] N.Ookubo, J. Appl. Phys. **74**, 6375 (1993).
- [102] X.G.Zhang, S.D.Collins, and R.L.Smith, J. Electrochem. Soc. **136**, 1561 (1989).
- [103] V.Lehmann and U.Gosele, Appl. Phys. Lett. **58**, 856 (1991).
- [104] V.P.Parkhutik, L.K.Glinenko, and V.A.Labunov, Surf. Technol. **20**, 265 (1983).
- [105] V.P.Parkhutik, J.M.Martinez-Duart, and J.M.Albella, in *Proc. NATO A.R. Workshop on Optical properties of low dimensional silicon structures* (Meylan, 1993).
- [106] V.Lehmann, Adv. Mater. **4**, 114 (1992).
- [107] V.Lehmann, H.Cerva, and U.Gosele, Mat. Res. Soc. Symp. Proc **256**, 3 (1992).
- [108] V.Lehmann *et al.*, Jpn. J. Appl. Phys. **32**, 2095 (1993).
- [109] R.W.Bower and S.D.Collins, Phys. Rev. A **43**, 3165 (1991).
- [110] R.F.Voss and M.Tomkiewicz, J. Electrochem. Soc. **132**, 371 (1985).
- [111] N.Noguchi and I.Suemuene, Appl. Phys. Lett. **62**, 1429 (1993).
- [112] S.Schuppler *et al.*, Phys. Rev. Lett. **72**, 2648 (1994).
- [113] M.Thonissen *et al.*, J. Appl. Phys. **80**, 2990 (1996).
- [114] D.Andsager, J.Hilliard, and M.H.Nayfeh, Appl. Phys. Lett. **64**, 1141 (1994).
- [115] R.L.Smith and S.D.Collins, Phys. Rev. A **39**, 5409 (1989).
- [116] H.Yan and X.Hu, J. Appl. Phys. **73**, 4324 (1993).

- [117] Y.M.Weng, J.Y.Qiu, Y.H.Zou, and X.F.Zong, J. Vac. Sci. Technol. B **14**, 2505 (1996).
- [118] E.O.Kane, Phys. Rev. **131**, 79 (1963).
- [119] I.M.Lifshitz, Adv. Phys. **13**, 483 (1964).
- [120] V.Sa-yakanit and H.R.Glyde, Comments on Solid State Physics **13**, 35 (1987).
- [121] A.Hallimaoui *et al.*, Appl. Phys. Lett. **59**, 304 (1991).
- [122] S.Gardelis *et al.*, Appl. Phys. Lett. **59**, 2118 (1991).
- [123] Y.H.Xie *et al.*, J. Appl. Phys. **71**, 2403 (1992).
- [124] A.G.Cullis and L.T.Canham, Nature **353**, 335 (1991).
- [125] S.Zhang, Appl. Phys. Lett. **62**, 642 (1993).
- [126] S.Banerjee *et al.*, Solid State Commun. **84**, 691 (1992).
- [127] R.E.Hummel and S.S.Chang, Appl. Phys. Lett. **61**, 1965 (1992).
- [128] C.Tsai *et al.*, Appl. Phys. Lett. **60**, 1700 (1992).
- [129] K.H.Jung *et al.*, Appl. Phys. Lett. **59**, 3264 (1991).
- [130] G.Fishman, I.Mihalcescu, and R.Romestain, Phys. Rev. B **48**, 1464 (1993).
- [131] J.B.Khurgin, E.W.Forsythe, G.S.Tompa, and B.A.Khan, Appl. Phys. Lett. **69**, 1241 (1996).
- [132] M.S.Hybertsen, Mat. Res. Soc. Symp. Proc. **256**, 179 (1992).
- [133] R.Behrensmeier *et al.*, Appl. Phys. Lett. **62**, 2408 (1993).
- [134] B.Sapoval, J.Russ, and J-N. Chazalviel, J. Phys. Condens. Matter **8**, 6235 (1996).
- [135] C.Lanczos, *Applied Analysis* (Prentice Hall, Englewood Cliffs, NJ, 1961).
- [136] V.Lehmann, J. Electrochem. Soc. **140**, 2836 (1993).

- [137] J.J.Mares, J.Kristofik. and V.Smid, *Semicond. Sci. Technol.* **7**, 119 (1992).
- [138] Z.Chen, T.-Y.Lee, and G.Bosman, *J. Appl. Phys.* **76**, 2499 (1994).
- [139] S.Sinha *et al.* (unpublished).
- [140] L.Pavesi and M.Ceschini, *Phys. Rev. B* **48**, 17625 (1993).
- [141] T.Suemoto, K.Tanaka, and A.Nakajima, *Phys. Rev. B* **49**, 11005 (1994).
- [142] Y.Kanemitsu, *Phys. Rev. B* **53**, 13515 (1996).
- [143] J.J.Mares, J.Kristofik, J.Pangrac, and A.Hospodkova, *Appl. Phys. Lett.* **63**, 180 (1993).
- [144] D.Deresmes, V.Marissael, D.Stievenard, and C.Ortega, *Thin Sol. Films* **255**, 258 (1995).
- [145] H.Berthelot, *Ann. Chim. Phys.* **66**, 110 (1862).
- [146] L.Pavesi, M.Ceschini, and H.E.Roman, *Thin Sol. Films* **255**, 67 (1995).
- [147] V.A.Joshkin *et al.*, *Phys. Rev. B* **52**, 12102 (1995).
- [148] N.Ookubo, N.Hamada, and S.Sawada, *Solid State Commn.* **92**, 369 (1994).
- [149] C.M.Hurd, *J. Phys. C*, **18**, 6487 (1985).
- [150] G. C. John and V. A. Singh, *Phys. Rev. B* **54**, 4416 (1996).
- [151] N.Ookubo *et al.*, *Appl. Phys. Lett.* **61**, 940 (1992).
- [152] R.H.Tredgold, *Proc. Phys. Soc.* **80**, 807 (1962).
- [153] G.Amato, *Solid State Commun.* **89**, 213 (1994).
- [154] S.Banerjee, *Bull. Mater. Sci.* **17**, 533 (1994).
- [155] Z.Y.Xu, M.Gal, and M.Gross, *Appl. Phys. Lett.* **60**, 1375 (1992).
- [156] G.Mauckner *et al.*, *J. Appl. Phys.* **75**, 4167 (1994).
- [157] S.Finkbeibner and J.Weber, *Thin Sol. Films* **255**, 254 (1995).

- [158] V.P.Kesan *et al.*, J. Vac. Sci. Tech. A **11**, 1736 (1993).
- [159] L.Tsybekov, S.D.Duttgupta, and P.M.Fauchet, Solid State Commun. **95**, 429 (1995).
- [160] G.Amato, G. Francia, and P.Menna, Thin Sol. Films **255**, 204 (1995).
- [161] A.Shimuzu *et al.*, Jpn. J. Appl. Phys. **35**, L276 (1996).
- [162] E.V.Astrova *et al.*, Thin Sol. Films **255**, 196 (1995).
- [163] R.A.Street, Adv. Phys. **25**, 397 (1976).
- [164] I.Hirabayashi, K.Morigaki, and S.Yamanaka, J. Phys. Soc. Jap. **52**, 671 (1983), J. Non-Cryst. Solids **59-60**, 645 (1983).
- [165] M.Stutzmann *et al.*, Adv. Sol. St. Phys. **32**, (1992).
- [166] P.D.J.Calcott *et al.*, J. Phys. Condens. Matter **5**, L91 (1993).
- [167] G.W.'t Hooft, Y.A.R.R.Kessener, G.L.J.A.Rikken, and A.H.J.Venhuizen, Appl. Phys. Lett. **61**, 2344 (1992).
- [168] T.Tsuboi, R.Laiho, and A.Pavlov, Thin Sol. Films **255**, 216 (1995).
- [169] R.Laiho, A.Pavlov, O.Hovi, and T.Tsuboi, Appl. Phys. Lett. **63**, 275 (1993).
- [170] W.Zhou *et al.*, Appl. Phys. Lett. **61**, 1435 (1992).
- [171] N.Ookubo, Y.Matsuda, and N.Kuroda, Appl. Phys. Lett. **63**, 346 (1993).
- [172] J.M.Ryan, P.R.Wamsley, and K.L.Bray, Appl. Phys. Lett. **63**, 2260 (1993).
- [173] J.M.Zeman *et al.*, Thin Sol. Films **255**, 35 (1995).
- [174] J.Zeman, M.Zigone, G.L.J.A.Rikken, and G.Martinez, J.Phys.Chem.Solids **56**, 655 (1995), solid State Commn.**96**, 503 (1995).
- [175] L.Pavesi, Solid state phenomena **44-46**, 261 (1995).



- [176] X.-S.Zhao, P.D.Persans, J.Schroeder, and Y.-J.Wu. in *Microcrystalline Semiconductors: Materials Science and Devices*, MRS Symposia Proceedings No: 283, edited by P.M.Fauchet *et al.* (Materials Research Society, Pittsburgh, 1993), p. 127.
- [177] W.Paul and G.L.Pearson, *Phys. Rev.* **98**, 1755 (1995).
- [178] B.Welber, C.K.Kim, M.Cardona, and S.Rodrigues, *Solid State Commn.* **17**, 1021 (1975).
- [179] B.A.Weinstein, *Phys. Rev. B* **23**, 787 (1981).
- [180] C.-Y. Yeh, S.B.Zhang, and A.Zunger, *Appl. Phys. Lett.* **64**, 3545 (1994).
- [181] J.Camassel *et al.*, in *Proceedings of the 21st International Conference on the Physics of Semiconductors*, edited by P.Jiang and H-Z.Zhang (World Scientific, Singapore, 1992), p. 1463.
- [182] M.Sacilotti *et al.*, *Electronics Letters* **29**, 790 (1993).
- [183] M.Sacillotti *et al.*, *J. Lumin.* **57**, 33 (1993).
- [184] G.G.Qin and Y.Q.Jia, *Solid State Commun.* **86**, 559 (1993).
- [185] I.G.Austin *et al.*, *J. Non-Crystalline Solids* **32**, 373 (1979).
- [186] R.W.Collins, M.A.Paesler, and W.Paul, *Solid State Commun.* **34**, 833 (1980).
- [187] R.A.Street, *Phys. Rev. B* **23**, 861 (1981).
- [188] R.Stachowitz, M.Schubert, and W.Fuhs, *Phys. Rev. B* **52**, 10906 (1995).
- [189] C.Delerue *et al.*, *Phys. Rev. Lett.* **75**, 2228 (1995).
- [190] N.F.Mott and E.A.Davis, *Electronic Processes in Non-Crystalline Materials* (Clarendon Press, Oxford, 1979).
- [191] P.Gupta, V.Colvin, and S.M.George, *Phys. Rev. B* **37**, 8234 (1988).
- [192] I.M.Young, M.I.J.Beale, and J.E.Benjamin, *Appl. Phys. Lett.* **46**, 1133 (1985).
- [193] M.S.Brandt *et al.*, *Solid State Commun.* **81**, 307 (1992).

- [194] M.A.Tischler, R.T.Collins, J.H.Stathis, and J.C.Tsang, Appl. Phys. Lett. **60**, 639 (1992).
- [195] M.B.Robinson, A.C.Dillon, and S.M.George, Appl. Phys. Lett. **62**, 1493 (1993).
- [196] A.L.Smith and N.C.Angellotti, Spectrochemica Acta **15**, 412 (1959).
- [197] G.Lucovsky, Solid State Commun. **29**, 571 (1979).
- [198] T.S.Shi *et al.*, Phys. Stat. Sol.(a) **74**, 329 (1982).
- [199] S.N.Sahu *et al.*, J. Chem. Phys. **77**, 4330 (1982).
- [200] A.Zunger, Phys. Rev. B **22**, 5839 (1980).
- [201] L. Pauling, *The Nature of the Chemical Bond* (Cornell University press, Ithaca, N.Y. 1960).
- [202] A.L.Allred and E.G.Rochow, J. Inorg. Nucl. Chem **5**, 264.269 (1958).
- [203] R.T.Sanderson, *Chemical Bonds and Bond Energies* (Academic Press, New York, 1976).
- [204] T.Moller, *Inorganic Chemistry: A Modern Introduction* (John Wiley, New York, 1982).
- [205] H.C.Verma, G. C. John, and V. A. Singh, Phys. Rev. B **53**, 9831 (1996).
- [206] R.T.Sanderson, *Chemical Periodicity* (Reinhold Publishing Corp., New York, 1960), pg. 16-56.
- [207] N.Kniffler, B.Schroeder, and J.Geiger, J. Non-Cryst. Sol. **58**, 153 (1983).
- [208] V.M.Dubin, F.Ozanam, and J.-N.Chazalviel, Phys. Rev. B **50**, 14867 (1994).
- [209] Y.Ogata, H.Niki, T.Sakka, and M.Iwasaki, J. Electrochem. Soc. **142**, 195 (1995).
- [210] T.Unagami, J. Electrochem. Soc. **127**, 476 (1980).
- [211] T.Unagami, Jpn. J. Appl. Phys. **19**, 231 (1980).

- [212] H.Shanks *et al.*, Phys. Stat. Sol. (b) **100**, 43 (1980).
- [213] W.Paul, Solid State Commun. **34**, 283 (1980).
- [214] S.Oguz, R.W.Collins, M.A.Paesler, and W.Paul, J. Non-Cryst. Sol. **35-36**, 231 (1980).
- [215] V. A. Singh, C.Weigel, J.W.Corbett, and L.M.Roth, Phys. Stat. Sol. b **81**, 637 (1977).
- [216] Y.J.Chabal and K.Raghavachari, Phys. Rev. Lett. **53**, 282 (1984).
- [217] Y.J.Chabal and K.Raghavachari, Phys. Rev. Lett. **54**, 1055 (1985).
- [218] K.Yamamoto, T.Nakanishi, H.Kasahara, and K.Abe, J. Non-Cryst. Sol. **59-60**, 213 (1983).
- [219] Wu Shi-Qiang *et al.*, J. Non-Cryst. Sol. **59-60**, 217 (1982).
- [220] *Oxygen, Carbon, Hydrogen and Nitrogen in Crystalline Silicon*. Vol. 59 of *Mat. Res. Soc. Symp. Proceedings*, edited by J.C.Mikkelsen Jr., S.J.Pearton, J.W.Corbett, and S.J.Pennycok (Materials Research Society, Pittsburgh, 1986).
- [221] X.Y.Hou *et al.*, Appl. Phys. Lett. **62**, 1097 (1993).
- [222] S.Pantelides, Physics today **45**, 67 (September 1992).
- [223] L.E.Brus, in *Nanophase Materials*, edited by G.C.Hadjipanayis and R.W.Siegel (Kluwier Academic Publishers, Netherlands, 1994), pp. 433-448.
- [224] K.D.Hirschman, L.Tsybeskov, S.P.Duttagupta, and P.M.Fauchet, Nature **384**, 338 (1996).
- [225] A.-L.Barabasi and H.E.Stanley, *Fractal concepts in surface growth* (Cambridge University Press, Cambridge, 1995).
- [226] K. R. Popper, *The Logic of Scientific Discovery* (Hutchinson & Co., London, 1959), pp. 32-42.

- 
- [227] G.S.Solomon. J.A.Trezza. A.F.Marshall. and J.S.Harris, Jr. Phys. Rev. Lett. **76**, 952 (1996).
- [228] B.G.Levi, Physics Today **49**, 22 (May 1996).
- [229] T.Frello, E.Veje, and D.Leishiko. J. Appl. Phys. **79**, 1027 (1996).